

**NUMERICAL SIMULATIONS OF THE EFFECT OF
TURBULENCE INTENSITY AND INTEGRAL LENGTH
SCALE ON STAGNATION REGION HEAT TRANSFER**

CENTRE FOR NEWFOUNDLAND STUDIES

**TOTAL OF 10 PAGES ONLY
MAY BE XEROXED**

(Without Author's Permission)

NUR IKHWAN



**National Library
of Canada**

**Acquisitions and
Bibliographic Services**

**395 Wellington Street
Ottawa ON K1A 0N4
Canada**

**Bibliothèque nationale
du Canada**

**Acquisitions et
services bibliographiques**

**395, rue Wellington
Ottawa ON K1A 0N4
Canada**

Your file Votre référence

Our file Notre référence

The author has granted a non-exclusive licence allowing the National Library of Canada to reproduce, loan, distribute or sell copies of this thesis in microform, paper or electronic formats.

The author retains ownership of the copyright in this thesis. Neither the thesis nor substantial extracts from it may be printed or otherwise reproduced without the author's permission.

L'auteur a accordé une licence non exclusive permettant à la Bibliothèque nationale du Canada de reproduire, prêter, distribuer ou vendre des copies de cette thèse sous la forme de microfiche/film, de reproduction sur papier ou sur format électronique.

L'auteur conserve la propriété du droit d'auteur qui protège cette thèse. Ni la thèse ni des extraits substantiels de celle-ci ne doivent être imprimés ou autrement reproduits sans son autorisation.

0-612-62389-0

Canada

**Numerical Simulations of
the Effect of Turbulence Intensity and
Integral Length Scale on Stagnation Region
Heat Transfer**

By
©Nur Ikhwan

**A thesis submitted to the School of Graduate
Studies in partial fulfillment of the
requirements for the degree of
Master of Engineering**

**Faculty of Engineering and Applied Science
Memorial University of Newfoundland
December, 2000**

St. John's Newfoundland Canada

Abstract

Numerical simulations of stagnation region heat transfer for laminar and turbulent freestreams have been performed using a commercial CFD code CFX-TASCflow. Prior to the stagnation region simulations, some classical flow problems were solved to validate the CFD code and evaluate the different turbulence models. Simulations were performed for flow in a square driven cavity, laminar and turbulent boundary layers on a flat plate and flow over a backward facing step. The simulation results are in good agreement with previous simulation results, experiment and theory. The simulations of stagnation region heat transfer with a laminar freestream are performed at Reynolds numbers ranging from 6.5×10^3 to 6.5×10^5 . The laminar freestream simulations were performed to obtain an appropriate grid structure and simulation parameters. The laminar simulation results are in good agreement with results of Rigby and VanFossen. The simulations for a turbulent freestream are performed at Reynolds numbers of 1.3×10^4 , 5×10^4 and 1×10^5 , turbulence intensities of 1%, 3% and 5% and the ratio of integral length scales to leading edge diameter (λ/D) of 0.4282, 0.5709 and 0.7136. The $k-\epsilon$ turbulence model proposed by Kato-Launder is used for the simulation. The heat transfer results from the simulations are compared with the empirical solution of VanFossen, et al. The heat transfer increases with Reynolds number and turbulence intensity, and decreases with integral length scale.

Acknowledgement

I would like to thank the Indonesian Government for providing financial support for my period of study at Memorial University of Newfoundland from May 1998 until August 2000.

My gratitude also goes to my supervisors, Dr. Chan Ching and Dr. Neil Hookey. The frequent discussions with Dr. Ching have helped me understand the phenomena of turbulence and in finishing my thesis. I also wish to thank Dr. Ching for providing the CFD code TASCflow during my research. Special thanks to Dr. Hookey for his suggestions and consultations that have helped me in understanding CFD and in finishing my simulations.

My thanks to N. Aung for discussions and providing the experimental results. I would also like to thank David Press and Philip van Ulden for their help in installing and providing access to the CFD code.

Finally, my heartfelt gratitude to my wife Letina, and my sons Azhar and Burhan who will always shine my heart.

Table of Contents

ABSTRACT	I
ACKNOWLEDGEMENT	II
TABLE OF CONTENTS	III
LIST OF FIGURES	VI
LIST OF TABLES	XI
LIST OF SYMBOLS	XII
GENERAL	XII
GREEK SYMBOLS	XIV
1. INTRODUCTION	1
1.1. BACKGROUND	1
1.2. PURPOSE OF STUDY	5
1.3. OUTLINE OF THESIS	6
2. THEORY	8
2.1. GOVERNING EQUATIONS	8
2.1.1 Instantaneous Equations	8

2.1.2. Reynolds Averaging.....	10
2.1.3. Reynolds-Averaged Equations.....	11
2.2. TURBULENCE MODELING.....	11
2.2.1. Classification of Turbulence Models	12
2.2.1.1. Algebraic Model	13
2.2.1.2. Turbulence Energy equation model	14
2.3. TURBULENCE MODEL FOR FLOW NEAR A SOLID WALL.....	20
2.3.1. Standard Wall Function	21
2.3.2. Two-Layer Turbulence Model	23
2.4 NUMERICAL METHODS	25
2.4.1. Discretization Schemes.....	25
2.4.2. Co-located Method.....	29
2.4.3. The linear solver	30
2.4.4. CFX-TASCflow software system	33
3. SOFTWARE VALIDATION.....	40
3.1. FLOW IN A SQUARE DRIVEN CAVITY	40
3.1.1. Problem Definition.....	40
3.1.2. Flow simulation	41
3.1.3. Discussion of results	42
3.2. BOUNDARY LAYER ON A FLAT PLATE	43
3.2.1. Problem Definition.....	46

3.2.2. Flow simulation	48
3.2.3. Discussion of result.....	49
3.3. BACKWARD-FACING STEP	52
3.3.1. Problem Definition.....	53
3.3.2. Discussion of result.....	54
4. STAGNATION REGION HEAT TRANSFER.....	72
4.1. LAMINAR FREESTREAM.....	72
4.1.1. Problem definition	74
4.1.2. Flow simulation	76
4.2. TURBULENT FREESTREAM.....	79
4.2.1. Problem definition	85
4.2.2. Flow simulation	87
5. CONCLUDING REMARKS AND RECOMMENDATIONS.....	113
5.1 CONCLUDING REMARKS	113
5.2. RECOMMENDATIONS.....	116
REFERENCES.....	118

List of Figures

Figure 2.1: Velocity profile in the near wall region (reproduced from CFX-TASCflow, 1999a).	34
Figure 2.2: Distribution of f_ϵ over vertical distance, y^+	34
Figure 2.3: Distribution of f_μ over vertical distance, y^+	35
Figure 2.4: The definition of a two-dimensional control volume and integration surfaces.	35
Figure 2.5: Algorithm for the equal-order method used for solving u , v , w and p	36
Figure 2.6: Solution algorithm for turbulent flow.	37
Figure 2.7 : Residual error distribution along a grid line (reproduced from CFX-TASCflow, 1999a).	38
Figure 2.8: One-dimensional grid hierarchy and error components line (reproduced from CFX-TASCflow, 1999a).	38
Figure 2.9: V and W cycle of multigrid line (CFX-TASCflow, 1999a).	39
Figure 2.10: Structure of CFX-TASCflow line (CFX-TASCflow, 1999a)	39
Figure 3.1: Flow domain in a square driven cavity.	56
Figure 3.2: Grid structure for flow in square driven cavity.	56
Figure 3.3: U-velocity distribution along $x=0.5$ for different discretization schemes: a). $Re=100$ and b). $Re=400$	57

Figure 3.4: U-velocity distribution along $x=0.5$ for different discretization schemes at grid size $41 \times 41 \times 3$ and $Re=400$.	58
Figure 3.5: Velocity contour (a), and velocity vector (b) for $Re=100$.	58
Figure 3.6: Velocity contour (a), and velocity vector (b) for $Re=400$.	59
Figure 3.7: Schematic of boundary layer over a flat plate.	59
Figure 3.8: Blasius velocity profile for laminar boundary layer (reproduced from Panton, 1984).	60
Figure 3.9: The sensitivity of skin friction calculation to the number of nodes within boundary layer for some turbulence models (rep. from Bardina et al. 1997).	60
Figure 3.10: Layout for grid structure and boundary conditions for flow over a flat plate.	61
Figure 3.11: Grid structure for flow over a flat plate. Top: grid distribution, left bottom: grid distribution along vertical direction, right bottom: grid refinement around leading edge.	62
Figure 3.12: Pressure contours for (a) laminar flow, (b) turbulent flow; and temperature contour for (c) laminar and (d) turbulent flow.	63
Figure 3.13: Velocity contours for (a) laminar, (b) turbulent flow; and velocity vector for (c) laminar and (d) turbulent flow.	64
Figure 3.14: Velocity profile at several streamwise locations (laminar boundary layer).	65
Figure 3.15: Distribution of Nusselt numbers (laminar boundary layer).	65
Figure 3.16: Distribution of skin Friction (laminar boundary layer).	66
Figure 3.17: Nusselt number for coarse grid structure (turbulent boundary layer).	66

Figure 3.18: Skin friction for coarse grid structure (turbulent boundary layer.....	67
Figure 3.19: Nusselt number distribution using different distances to the first node.	67
Figure 3.20: Skin friction distribution using different distances to the first node..	68
Figure 3.21: Distribution of wall unit value for different distance to the first node.....	68
Figure 3.22: Flow domain for backward facing step.	69
Figure 3.23: Grid structure for backward facing step.	69
Figure 3.24: Mean streamwise velocity profile at several streamwise locations in the recirculation region..	70
Figure 3.25: Turbulent kinetic energy profile at several streamwise locations in the recirculation region..	71
Figure 4.1: The influence of separation and reattachment flow on the local heat transfer rate (reproduced from Zdravkovich, 1997).....	95
Figure 4.2: The location of separation point for flow over cylinder (rep. from Zdravkovich, 1997).....	95
Figure 4.3: Boundary conditions for flow over the stagnation region.....	96
Figure 4.4: Grid structures for laminar flow over the stagnation region.	97
Figure 4.5: The performance of discretization scheme in estimating Frossling number using the first grid structure.	98
Figure 4.6: Local grid refinement near the wall on the stagnation point.	98
Figure 4. 7 Velocity contours for different discretization schemes (a) Upwind, (b) MWS, (c) MLPS and (d) LPS.	99

Figure 4.8: Estimation of Frossling number using different grid structure.	100
Figure 4.9: (a) Speed contour and (b) pressure contour for the first grid.	100
Figure 4.10: (a) Speed contour and (b) pressure contour for the second grid.	101
Figure 4.11: (a) Speed contour and (b) pressure contour for the third grid.	101
Figure 4.12: Frossling number distribution at different Reynolds numbers.	102
Figure 4. 13 The small separation and reattachment at $Re=1.3 \times 10^5$ located in $80^0 < \theta < 90^0$.	102
Figure 4. 14 Correlation of stagnation region heat transfer with turbulence freestream proposed by Lowery and Vachon (1997).	103
Figure 4. 15 Correlation of stagnation region heat transfer with turbulence freestream proposed by Van Fossen et al. (1995).	103
Figure 4.16: The estimation of heat transfer on the suction side of a turbine blade surface (Reproduced from Larsson, 1997).	104
Figure 4.17: The estimation of heat transfer on the pressure side of a turbine blade surface (Reproduced from Larsson, 1997).	104
Figure 4.18: Turbulent kinetic energy distribution around the stagnation region.	105
Figure 4.19: Distribution of Frossling numbers for different turbulence models at $Re=1 \times 10^5$, $Tu=0.75\%$ and $\lambda/D=0.98$.	106
Figure 4.20: Distribution of Frossling numbers for Kato and RNG turbulence models at $Re=5 \times 10^4$, $Tu=5\%$ and $\lambda/D=0.69$.	106

Figure 4. 21 Turbulence kinetic energy contour at $Re=5 \times 10^4$, $Tu=5\%$ and $\lambda_{eff}/D= 0.69$ (a) Kato, (b) RNG..... 107

Figure 4. 22 Velocity contours at the final simulation. (a) $Re=10^5$, (b) $Re=1.3 \times 10^4$ 108

Figure 4.23: Distribution of Frossling numbers for Kato turbulence models at $Re=1. \times 10^5$: (a) $\lambda=0.4282$, (b) $\lambda_{eff}/D=0.5709$ and (c) $\lambda_{eff}/D=0.7136$ 109

Figure 4.24: Distribution of Frossling numbers for Kato turbulence models at $Re=5. \times 10^4$: (a) $\lambda=0.4282$, (b) $\lambda_{eff}/D=0.5709$ and (c) $\lambda_{eff}/D=0.7136$ 110

Figure 4.25: Distribution of Frossling numbers for Kato turbulence models at $Re=1.3 \times 10^4$: (a) $\lambda=0.4282$, (b) $\lambda_{eff}/D=0.5709$ and (c) $\lambda_{eff}/D=0.7136$.) 111

Figure 4.26: Stagnation Frossling number vs. $Tu Re_d^{0.8} (\lambda/D)^{-0.574}$ 112

List of Tables

Table 2. 1: Closure coefficients for some proposed k-ϵ turbulence models.....	17
Table 3.1: Parameters for laminar and turbulent boundary layer over a flat plate	47
Table 3.2 Comparison of the estimated reattachment length.....	54
Table 4.1: Control parameters for laminar freestream simulations	75
Table 4.2: Control parameter for turbulent freestream simulations.....	86
Table 4.3: Reynolds number, turbulence intensity and integral length scale (λ_z/D) for simulations with freestream turbulence	87
Table 4.4: Stagnation Frossling numbers.....	92

List of Symbols

General

C	additive constant in the law of the wall
$C_\mu, C_l, f_\varepsilon, \sigma_k, \sigma_\varepsilon$	closure coefficients of turbulence model
C_f	skin friction
c_p	Specific heat at constant pressure
c_v	Specific heat at constant volume
D	leading edge diameter
e_0	total energy
E_0	Mean total energy
$f_\mu, f_l, f_\varepsilon, \varepsilon_0$ and E	damping functions of turbulence model
Fr	Frossling number = $\frac{Nu_x}{\sqrt{Re}}$
h	convection coefficient, inlet height in flow over a backward-facing step
H	outlet height in flow over a backward-facing step
k	thermal conductivity, turbulent kinetic energy
ℓ_{mix}	mixing length of turbulence
ℓ_t	turbulence length scale
L	characteristic length
n^*	distance of the first node from the wall (in wall unit)

n^+	dimensionless wall unit = $\frac{u_\tau y}{\nu}$
Nu	Nusselt number
p	pressure
Pr	Prandtl number
q	heat flux
Re	Reynolds number
Re_D	Reynolds number based on diameter D
Re_τ	turbulent Reynolds number = $\frac{k^2}{\varepsilon \nu}$
Re_y	near-wall turbulence Reynolds number = $\frac{k^{1/2} y}{\nu}$
S_ϕ	source term in governing equation
T	Temperature
T_∞	freestream temperature
T_f	fluid temperature
Tu	turbulence intensity = u'/U
T_w	wall temperature
U	Mean velocity
u_τ	friction velocity
u'	fluctuating velocity
u^+	ratio of tangential velocity and friction velocity = u_t / u_τ
u_t	tangential velocity

$\overline{u_i u_i}$	time averaged fluctuating velocity
V	freestream velocity
W	height of backward-facing step
x , y, z	rectangular Cartesian coordinates
y	distance perpendicular to the wall
y^+	dimensionless wall unit = $\frac{u_\tau y}{\nu}$

Greek Symbols

μ	molecular viscosity
θ	angular location of stagnation region
δ	boundary layer thickness
Γ	coefficient of diffusion
ρ	density
ϕ	scalar dependent variable in governing equation
η	dimensionless distance unit in laminar boundary layer
χ	integral length scale
κ	Karman constant
ϵ	specific dissipation
ω	specific dissipation rate
δ_{ij}	Kronecker delta
τ_{ij}	Reynolds-stress tensor

Δn	distance of the first node from the wall
μ_T	eddy viscosity
τ_w	wall shear stress
∇	control volume
ν	kinematics molecular viscosity

1. Introduction

A study of leading edge heat transfer by convection is important because of its many critical applications. For example, the highest heat flux in heat exchanger tubes in cross flow occurs in the stagnation region. Another critical application would be heat transfer to the leading edge of gas turbine blades, especially the stagnation region, because of the very high temperature of the combustion gases. Heat transfer is usually highest in this region, and this restricts efforts to increase turbine efficiency by raising inlet temperature. A clear understanding and accurate prediction of stagnation region heat transfer is necessary for the design of effective blade cooling systems to allow higher turbine inlet temperature. It is difficult, however, to predict stagnation region heat transfer accurately because of the complex flow field in a gas turbine.

1.1. Background

The physical mechanism of heat transfer in the stagnation region is not well understood. Freestream turbulence significantly augments the stagnation region heat transfer. It is believed that three dimensional vortex stretching near the stagnation region is primarily responsible for the increase in heat transfer (Sutera, et al. 1963). While heat transfer in the stagnation region can be estimated if the freestream is laminar (Frossling, 1940), there is no analytical solution when the freestream is turbulent. It has been established, however, that the heat transfer depends on Reynolds number, turbulence intensity, integral length scale and vorticity (Kestin, 1966; Lowery and Vachon, 1975; Van Fossen et al., 1995). For example, an increase in Reynolds number results in thinner

boundary layers with increased temperature gradients, and consequently an increase in heat transfer.

Freestream turbulence also promotes earlier boundary layer transition that can result in higher heat transfer on a turbine blade. Zhang and Han (1995) showed that an increase in turbulence intensity by 10 percent could result in an increase in heat transfer by 25-30 percent. Van Fossen et al. (1994) performed experiments using grids to generate different integral length scale, with ratio 0.05 to 0.3 to leading edge diameter, to show that a decrease of length scale of turbulence increases the heat transfer. Rigby and Van Fossen (1991 and 1992) determined that a spanwise variation of freestream velocity, representing a spanwise vortex, caused an increase in heat transfer on cylindrical and elliptical leading edges. Van Fossen et al. (1994) also showed that an increase in turbulence intensity causes significant heat transfer augmentation on both elliptical and cylindrical leading edges.

Numerical calculations for leading edge heat transfer in the presence of freestream turbulence can still be in error by a significant amount (Larsson, 1996; Larsson et al., 1995; and Rigby and VanFossen, 1992). The main sources of error are due to the turbulence model, the discretization scheme and grid construction. When using the Reynolds Averaged Navier Stokes (RANS) equations, models are required for the Reynolds-stresses. Many turbulence models use the Boussinesq (1877) analogy between the Reynolds-stress and viscous shear stress tensor. This introduces an eddy viscosity,

which must be modelled. In algebraic turbulence models, eddy viscosity is usually correlated with a mixing length. By finding a proper mixing length, the RANS equations can be solved numerically. Turbulence models, which express the eddy viscosity in terms of specific turbulent kinetic energy (k), are also commonly used. The equation for turbulent kinetic energy contains the dissipation (ϵ) that requires an additional equation or correlation for closure. One-equation models introduce a closure coefficient to model the correlation for dissipation. In two-equation models, an additional equation is introduced for the correlation. The usual parameter for the additional equation is ω , ω^2 or ϵ . The turbulence models are usually named on the basis of the two equations used for the correlation, namely k - ω , k - ω^2 and k - ϵ model. Among the two-equation models, the k - ϵ model is preferable, because it has good performance in a wide range of applications (Wilcox, 1993).

The simulations of Larsson, et al. (1995) on turbine blade heat transfer showed errors as high as 33 percent in the vicinity of the leading edge. High freestream turbulence intensity induces earlier transition of the boundary layer from laminar into turbulent in the leading edge region. Most turbulence models predict transition earlier than experiment, which can overestimate heat transfer rates. Larsson (1996) modified the production term in the turbulence kinetic energy equation to reduce the error, and found it gave better results for the k - ω model, but not for the k - ϵ model. The primary error of the k - ϵ model is due to inaccuracies of the model in the near wall region. The ϵ equation has a tendency to generate turbulence length scales much larger than that shown through

experimental data. Methods to increase accuracy in this region include adjusting kinetic energy and length scale magnitude (Goldberg, et al. 1998), using a wall-function (CFX-TASCflow, 1999; Versteeg and Malalasekera, 1995; Wilcox, 1993) and using an algebraic turbulence model (CFX-TASCflow, 1999).

Discretization schemes also play an important role in obtaining accurate computational results. The Central Differencing Scheme (CDS) has good accuracy, but it cannot predict flow direction well and can produce unrealistic oscillations. The oscillation is caused by negative coefficients in the convection-diffusion equation. The Upwind Differencing Scheme (UDS) remedies the deficiency by adjusting the values of each term in the convection-diffusion equation according to local flow direction so that negative coefficients are avoided. Unfortunately, the UDS scheme only has first order of accuracy, and consequently causes large truncation errors. Some schemes such as Upwind Weighted Differencing Scheme (UWDS), Exponential Differencing Scheme (EDS) and Hybrid Scheme contain UDS or CDS in a specific fraction of blending in order to eliminate the oscillations or increase its accuracy. Other alternative discretization schemes are Second Order Upwind (SOU) and QUICK (blending of UDS, CDS and SOU).

Formation of large angles between flow direction and grid orientation cause false diffusion that can result in significant error. This can be minimised by either creating a finer grid or by applying a Physical Advection Correction (PAC) scheme that evaluates

flow in crosswise and streamwise directions. High aspect ratio elements promote short wavelength errors caused by the remaining residual error in the elements. This kind of error can be damped out by applying multi-level and multigrid algorithms.

1.2. Purpose of Study

The objectives of the study are to verify the ability of the commercial CFD code, CFX-TASCflow, to simulate heat transfer in the stagnation region in the presence of freestream turbulence, and to determine the effect of turbulence intensity and integral length scale on heat transfer. The simulations were performed for both laminar and turbulent freestreams at Reynolds numbers based on leading edge diameter ranging from 13,000 to 100,000. The results of the numerical simulations are compared to existing experimental results. The ability of k - ϵ turbulence models provided by CFX-TASCflow (Standard, Kato and RNG) in estimating stagnation region heat transfer are evaluated in the simulations.

Prior to performing the stagnation region heat transfer simulations, the software was validated using some classical flow problems. The first validation was done by evaluating the velocity distribution in a square driven cavity. Calculations were also performed for the skin friction and heat transfer coefficient under constant wall temperature for laminar and turbulent boundary layers on a flat plate. Finally, estimation of reattachment length, velocity, turbulent kinetic energy and turbulent dissipation

distribution of flow over a backward-facing step was performed and compared to previous simulations.

1.3. Outline of Thesis

A description of theory is given in chapter 2. The chapter begins with a description of the governing equations for continuity, momentum and heat transfer for turbulent flow using the two-equation k - ε turbulence model. Discretization of the governing equations by the Finite Volume Method used in the software is discussed. The difficulties and proposed procedure to handle the problems in CFD that arise in diffusion-convection problems and pressure-velocity coupling are also presented. The solution enhancement by the multigrid method and the software structure of CFX-TASCflow are discussed in the last section of this chapter.

The software validation is presented in chapter 3. The three validation problems consist of flow in a square driven cavity, laminar and turbulent boundary layers over a flat plate and flow over a backward facing step. Chapter 4 contains a brief literature review for stagnation region heat transfer and the simulations of stagnation region for laminar and turbulent freestream. Reynolds numbers ranging from 6.5×10^3 to 1.3×10^4 are used for the laminar simulation. The influence of selected discretization schemes and grid structure on the accuracy of the results are also discussed. The simulations for a turbulent freestream were performed to evaluate the performance of three proposed two-equation turbulence models: Standard, Chien and RNG. The final simulations use the “best”

turbulence model, and combinations of Re (1.3×10^4 , 5×10^4 and 10^5), turbulence intensity (1%, 3% and 5%) and the ratio of integral length scales to the leading edge diameter (0.4282, 0.5709 and 0.7136). The flow near a solid wall is resolved using the two-layer turbulence model rather than the wall function, since the turbulence of the flow over the stagnation region is not in an equilibrium in the stagnation region. Finally, concluding remarks and suggestions are presented in chapter 5.

2. Theory

This Chapter is divided into four sections: the governing equations, turbulence model classification, turbulence models in the near wall region, and numerical methods. The first section explains the derivation of the governing equations for turbulent flow. The governing equations consist of the mass conservation, momentum and energy equations. Algebraic, one and two equation turbulence models are discussed in section 2. Since the CFD code, CFX-TASCflow, uses the two-equation k - ϵ model, some proposed k - ϵ models are discussed in detail. The methods for obtaining solutions in the near wall region consist of using wall functions and two-layer turbulence models. The fourth section contains a discussion of the numerical methods used to discretize the governing equations. The discretization methods for the convection-diffusion equation, the pressure-velocity coupling, multigrid methods and the software structure of CFX-TASCflow are discussed in this section.

2.1. Governing Equations

2.1.1 Instantaneous Equations

The instantaneous equations for mass conservation, momentum and energy conservation for incompressible flow are:

$$\frac{\partial}{\partial x_j}(\rho u_j) = 0 \quad (2.1)$$

$$\rho \frac{\partial u_i}{\partial t} + \rho u_j \frac{\partial u_i}{\partial x_j} = -\frac{\partial p}{\partial x_i} + \frac{\partial \tau_{ji}}{\partial x_j} \quad (2.2)$$

$$\rho \frac{\partial e_o}{\partial t} + \frac{\partial}{\partial x_j} [\rho u_j e_o + u_j p + q_j - u_i \tau_{ij}] = 0 \quad (2.3)$$

The vectors x_i , u_i , q_j are cartesian coordinate, velocity and heat flux, respectively. The scalars p , e_o and ρ are pressure, total energy and density. The tensor τ_{ij} is the viscous stress, and for Newtonian fluids, it can be expressed as:

$$\tau_{ij} = \mu \left(\frac{\partial u_i}{\partial x_j} + \frac{\partial u_j}{\partial x_i} \right) \quad (2.4)$$

From Fourier's law, heat flux is defined as:

$$q_j = -k \frac{\partial T}{\partial x_j} = -\frac{\mu c_p}{Pr} \frac{\partial T}{\partial x_j} \quad (2.5)$$

The total energy, e_o , is defined as:

$$e_o = e + \frac{1}{2} u_i u_i = c_v T + \frac{1}{2} u_i u_i \quad (2.6)$$

Equations (2.1) to (2.3) constitute the set of differential equations that govern the fluid flow. When the flow is turbulent, the flow variables can be decomposed into a mean and fluctuating component, and then averaged to obtain the governing equations for the mean flow.

2.1.2. Reynolds Averaging

There are two important concepts of averaging in turbulent flow: time averaging and spatial averaging. Time averaging is appropriate for inhomogeneous and stationary turbulent flow:

$$\phi(x) = \lim_{T \rightarrow \infty} \frac{1}{T} \int_0^{T+t} \phi(x,t) dt \quad (2.7)$$

For homogeneous and time-varying turbulent flow, spatial averaging is more appropriate:

$$\phi(t) = \lim_{V \rightarrow \infty} \frac{1}{V} \int_V \phi(x,t) dV \quad (2.8)$$

Since most turbulent flows are inhomogeneous, time averaging is more suitable. The flow variable is first decomposed into a mean and fluctuating component.

$$\phi(x,t) = \Phi(x,t) + \phi'(x,t) \quad (2.9)$$

Some important aspects of time averaging are detailed below (see Wilcox, 1993). The time average of the fluctuating component is zero and time averaging is commutative with spatial and time derivatives. When averaging a product of two variables, the mean of the product of fluctuating component, $\overline{\phi'\psi'}$, is not necessarily zero and depends on the correlation between the two variables. The variables are correlated if $\overline{\phi'\psi'} \neq 0$, and uncorrelated if $\overline{\phi'\psi'} = 0$. For example,

$$\overline{\frac{\partial \phi}{\partial x_i}} = \frac{\partial \overline{\Phi}}{\partial x_i} + \frac{\partial \overline{\phi'}}{\partial x_i} = \frac{\partial \overline{\Phi}}{\partial x_i} = \frac{\partial \overline{\Phi}}{\partial x_i} \quad (2.10)$$

$$\overline{\phi \psi} = \overline{(\Phi + \phi)(\Psi + \psi)} = \overline{\Phi \Psi} + \overline{\phi' \psi'} \quad (2.11)$$

2.1.3. Reynolds-Averaged Equations

The resulting equations after time averaging equations (2.1) to (2.3) are:

$$\frac{\partial U_i}{\partial x_i} = 0 \quad (2.12)$$

$$\frac{\partial U_i}{\partial t} + \frac{\partial}{\partial x_j} (U_i U_j) = \frac{1}{\rho} \left(-\frac{\partial P}{\partial x_i} + \frac{\partial}{\partial x_j} \left(\mu \frac{\partial U_i}{\partial x_j} + \rho \overline{u'_i u'_j} \right) \right) \quad (2.13)$$

$$\frac{\partial E_o}{\partial t} + \frac{\partial}{\partial x_j} (U_j E_o) = \frac{1}{\rho} \frac{\partial}{\partial x_j} \left(-U_j P - \overline{u'_j p} - \overline{u'_j e'_o} - Q + U_i \mu \frac{\partial U_i}{\partial x_j} + \rho \overline{u'_i u'_j} \right) \quad (2.14)$$

2.2. Turbulence Modeling

Equations (2.13) and (2.14) contain the unknown term, $\rho \overline{u'_i u'_j}$, which is known as the Reynolds-stress tensor. The Reynolds-averaged equations cannot be solved without additional information, because the number of unknowns exceed the number of

equations. The number of equations are five (continuity equation, three components of the momentum equation, and the energy equation), while the number of unknowns are eleven (average pressure, three average velocity components, average temperature, and six Reynolds-stress components). To solve the set of equations, additional equations or relations between the Reynolds-stress tensor and the other flow variables are required. The process of obtaining these relations is known as turbulence modelling.

Boussinesq (1877) was the first to propose a model for the Reynolds-stress by assuming an analogy between the viscous and Reynolds-stress tensor. He introduced the concept of eddy viscosity and proposed an algebraic turbulence model. Prandtl (1945) assumed that the eddy viscosity depended on the turbulence kinetic energy (k). Since the equation for turbulence kinetic energy contains specific dissipation, an additional equation or closure for specific dissipation is also required. The introduction of closure coefficients for specific dissipation (ϵ) in the turbulence kinetic energy equation produces a one-equation turbulence model. Kolmogorov (1942) proposed the equation for turbulent “frequency”, ω , and obtained the two-equation k - ω turbulence model. The k - ϵ turbulence model uses the equation for specific dissipation as the second governing equation.

2.2.1. Classification of Turbulence Models

Turbulence models are classified into algebraic models, turbulence energy equation models, and second order closure models. The second classification is according

to the number of additional equations required for the model. Algebraic and two-equation models are based on the Boussinesq approximation of eddy viscosity for estimating the Reynolds-stress tensor. The second order closure models use non-linear constitutive relations that relate Reynolds-stress tensor with k , mean strain rate and mean rotation tensor. The second order closure models have complicated algorithms and need very high computer capacity, these models are not used in CFX-TASCflow, and will not be discussed here.

2.2.1.1. Algebraic Model

The algebraic model is based on the Boussinesq analogy between the viscous shear stress and Reynolds-stress tensor.

$$-\overline{\rho u_i u_j} = \mu_T \frac{\partial U_i}{\partial x_j} \quad (2.15)$$

Prandtl expressed the turbulent viscosity in terms of a mixing length, ℓ_{mix} .

$$\mu_T = \rho \ell_{mix}^2 \left| \frac{dU}{dy} \right| \quad (2.16)$$

If the mixing length can be estimated, Reynolds-stress tensor can be calculated and the equations can be solved numerically. A drawback of this method is that ℓ_{mix} cannot be estimated reliably, since it depends on the flow configuration.

2.2.1.2. Turbulence Energy equation model

This model is based on the assumption that the Reynolds-stress tensor is proportional to the turbulent kinetic energy (k), where k is defined as:

$$k = \frac{1}{2} \overline{u'_i u'_i} = \frac{1}{2} (\overline{u'^2_1} + \overline{u'^2_2} + \overline{u'^2_3}) \quad (2.17)$$

The Reynolds-stress tensor is expressed as:

$$-\overline{\rho u'_i u'_j} = 2\mu_T S_{ij} - \frac{2}{3} \rho k \delta_{ij} \quad (2.18)$$

and the eddy viscosity is expressed as

$$\mu_T = \text{constant} \times \rho k^{1/2} \ell \quad (2.19)$$

The turbulent kinetic energy equation is obtained from the momentum equation:

$$\rho \frac{\partial k}{\partial t} + \rho U_j \frac{\partial k}{\partial x_j} = \tau_{ij} \frac{\partial U_i}{\partial x_j} - \rho \epsilon + \frac{\partial}{\partial x_j} \left[\mu \frac{\partial k}{\partial x_j} + \frac{1}{2} \overline{\rho u'_i u'_i u'_j} - \overline{p' u'_j} \right] \quad (2.20)$$

According to Direct Numerical Simulation (DNS) calculations (Mansoor et al., 1988), the

last two terms on the right hand side of equation (2.20) can be estimated as:

$$\frac{1}{2} \overline{\rho u'_i u'_i u'_j} - \overline{p' u'_j} = \frac{\mu_T}{\sigma_k} \frac{\partial k}{\partial x_j} \quad (2.21)$$

where σ_k is a closure coefficient. Substituting (2.21) into (2.20) provides the final form of the turbulent kinetic energy equation.

$$\rho \frac{\partial k}{\partial t} + \rho U_j \frac{\partial k}{\partial x_j} = \tau_{ij} \frac{\partial U_i}{\partial x_j} - \rho \epsilon + \frac{\partial}{\partial x_j} \left[(\mu + \mu_T / \sigma_k) \frac{\partial k}{\partial x_j} \right] \quad (2.22)$$

From equation (2.22), μ_T is obtained from equation (2.19) by specifying the constant as unity and σ_k is a closure coefficient where its value depends on the turbulence model. The only unknowns are turbulence length scale (ℓ) and specific dissipation (ϵ).

One-equation Model

For closing equation (2.22), Prandtl modelled the dissipation and used a constant of unity in equation (2.19).

$$\begin{aligned} \epsilon &= C_D \frac{k^{3/2}}{\ell} \\ \mu_T &= \rho k^{1/2} \ell \end{aligned} \quad (2.23)$$

Since the model contains only one additional equation, it is known as a one-equation model. The model assumes that the turbulence length scale (ℓ) is proportional to the mixing length (ℓ_{mix}).

Two-Equation Models

The two-equation turbulence models use the turbulent kinetic energy equation, and an additional equation for turbulence length scale or equivalent. The first model uses a frequency (ω) as the second parameter. Kolmogorov (1942) modelled ω as dissipation divided by turbulent kinetic energy, and the governing equation is obtained from dimensional analysis and physical interpretation (2.24). Wilcox, on the other hand, correlated turbulence length scale with ω (2.25).

$$\omega = ck^{1/2} / \ell \quad (2.24)$$
$$\rho \frac{\partial \omega}{\partial t} + \rho U_i \frac{\partial \omega}{\partial x_i} = \beta \rho \omega^2 + \frac{\partial}{\partial x_i} \left(\sigma \mu_\tau \frac{\partial \omega}{\partial x_i} \right)$$

$$\ell = k^{1/2} / \omega$$
$$\rho \frac{\partial \omega}{\partial t} + \rho U_i \frac{\partial \omega}{\partial x_i} = -\beta \rho \omega^2 + \alpha \frac{\omega}{k} \tau_{ij} \frac{\partial U_i}{\partial x_j} + \frac{\partial}{\partial x_i} \left[(\mu + \sigma \mu_\tau) \frac{\partial \omega}{\partial x_i} \right] \quad (2.25)$$
$$\mu_\tau = \rho k / \omega$$

In the k - ε turbulence model, the specific dissipation is obtained by taking the moment of the momentum equations.

$$\rho \frac{\partial \varepsilon}{\partial t} + \rho U_j \frac{\partial \varepsilon}{\partial x_j} = -2\mu \left[\overline{u'_{i,k} u'_{k,j}} + \overline{u'_{k,i} u'_{k,j}} \right] \frac{\partial U_i}{\partial x_j} - 2\mu \overline{u'_k u'_{i,j}} \frac{\partial^2 U_i}{\partial x_k \partial x_j} - 2\mu \overline{u'_{i,k} u'_{i,m} u'_{k,m}} - 2\mu \nu \overline{u'_{i,km} u'_{i,km}} + \frac{\partial}{\partial x_j} \left[\mu \frac{\partial \varepsilon}{\partial x_j} - \mu \overline{u'_j u'_{i,m} u'_{i,m}} - 2\nu \overline{p'_{,m} u'_{j,m}} \right] \quad (2.26)$$

The terms in the right hand side of equation (2.26) are denoted as production of specific dissipation, dissipation of specific dissipation, and the sum of molecular diffusion and turbulent transport of specific dissipation. It is not possible to obtain the new double and triple correlation of fluctuating velocity, pressure and velocity. DNS studies (Mansour et al. 1988) provide some insight for obtaining closure coefficients for the new correlation. The final form of the specific dissipation equation is (Wilcox, 1993):

$$\rho \frac{\partial \varepsilon}{\partial t} + \rho U_j \frac{\partial \varepsilon}{\partial x_j} = -C_{\varepsilon 1} \frac{\varepsilon}{k} \tau_{ij} \frac{\partial U_i}{\partial x_j} + C_{\varepsilon 2} \rho \frac{\varepsilon^2}{k} + \frac{\partial}{\partial x_j} \left[(\mu + \sigma \mu_T) \frac{\partial \varepsilon}{\partial x_j} \right] \quad (2.27)$$

The relationships between k - ε turbulence model with frequency and integral length scale are:

$$\omega = \varepsilon / (C_\mu k) \quad \text{and}$$

$$\ell = C_\mu k^{3/2} / \varepsilon \quad (2.28)$$

Originally, k - ε turbulence models were developed to solve flow with high Reynolds number. The presence of viscous effects near a solid wall is significant and most two-

equation turbulence models give large errors in the viscous sub-layer. To account for these viscous effects, some damping functions are required. Damping functions are additional functions that depend on the flow property in the near-wall region such as Re_τ , R_y and y^+ . The damping functions and closure coefficients of turbulence kinetic energy and dissipation equations for some proposed models are given in Table 2.1:

Model	f_μ	f_1	f_ϵ	ϵ_0	E	$C_{\epsilon 1}$	$C_{\epsilon 2}$	C_μ	σ_k	σ_ϵ
Jones- Launder	$e^{-2.5/(1+Re_\tau/50)}$	1	$1 - 0.3e^{-Re_\tau^2}$	$2\nu \left(\frac{\partial \sqrt{k}}{\partial y} \right)^2$	$2\nu \nu_\tau \left(\frac{\partial^2 U}{\partial y^2} \right)^2$	1.45	2.00	0.09	1.0	1.3
Launder- Sharma	$e^{-3.4/(1+Re_\tau/50)^2}$	1	$1 - 0.3e^{-Re_\tau^2}$	$2\nu \left(\frac{\partial \sqrt{k}}{\partial y} \right)^2$	$2\nu \nu_\tau \left(\frac{\partial^2 U}{\partial y^2} \right)^2$	1.44	1.92	0.09	1.0	1.3
Lam- Bremhorst	$\left(1 - e^{-0.0165 Re_\tau} \right)^2 \left(1 + 20.5 / Re_\tau \right)$	$1 + (0.05 / f_\mu)^3$	$1 - e^{-Re_\tau^2}$	0	0	1.44	1.92	0.09	1.0	1.3
Chien	$1 - e^{-0.0115 y^+}$	1	$1 - 0.22e^{-(Re_\tau/6)^2}$	$2\nu \frac{k}{y^2}$	$2\nu \frac{\bar{\epsilon}}{y^2} e^{-y^+/12}$	1.35	1.8	0.09	1.	1.3

Table 2.1. Closure coefficients for some proposed k - ϵ turbulence models.

where:

$C_{\epsilon 1}, C_{\epsilon 2}, C_{\mu}, \sigma_k$ and σ_{ϵ} = closure coefficients

$f_{\mu}, f_1, f_{\epsilon}, \epsilon_0$ and E = damping functions

Re_T = turbulent Reynolds number = $\frac{k^2}{\epsilon \nu}$

Re_y = near-wall turbulent Reynolds number = $\frac{k^{1/2} y}{\nu}$

y^+ = dimensionless wall unit = $\frac{u_{\tau} y}{\nu}$

In addition to closure coefficients, Table 2.1 also presents the damping functions that are required for solving flow near a solid wall or flow at low-Reynolds number. CFX-TASCflow (1999a) employs damping functions for solving flow near a solid wall by using a one-equation turbulence model (see section 2.3.2). The models given in Table 2.1 also propose k - ϵ model for low-Reynolds number by adding damping functions in the governing equations (Wilcox, 1993; and Larsson, 1997). Since the functions depend on the flow properties near the wall, the viscous effects near the wall can be estimated accurately.

2.3. Turbulence Model for Flow Near a Solid Wall

A solid wall is a common boundary condition, and is encountered in the study of boundary layers. It involves large gradients in velocity and temperature close to the wall. There are two important flow regions near solid walls: viscous sub-layer and log-law

layer. The viscous sub-layer region is used for two-layer turbulence models, while the standard wall function uses the log-law layer.

2.3.1. Standard Wall Function

Because the log-law region is larger than the viscous sublayer ($30 < y^+ < 500$), the application of the wall function requires fewer grid points in the near-wall region. Within the log-law region, streamwise velocity has a logarithmic function, which can be written as:

$$u^+ = \frac{1}{\kappa} \ln(y^+) + C \quad (2.29)$$

where:

$$y^+ = \rho u_\tau \Delta n / \mu = \text{wall unit distance}$$

$$u^+ = \frac{u_r}{u_\tau}$$

$$u_\tau = c_\mu^{1/4} \sqrt{k} = \text{friction velocity}$$

By assuming production equals dissipation of turbulent kinetic energy and the shear stress in the near wall region is constant (CFX-TASCflow, 1999a), the shear stress can be estimated by:

$$\tau_w = \tau_{\text{visc}} \frac{n^+}{u^+} \quad (2.30)$$

where:

$$\tau_{visc} = \mu u_r / \Delta n$$

Δn = distance of the first node from the wall

n^* = distance of the first node from the wall in wall unit

The recommended distance of the first node from the wall should have a value of n^* in the range of 30 to 500. For the thermal boundary layer, Kader (1981) proposed a relationship between wall temperature, wall heat flux and near wall fluid temperature as:

$$q_w = \frac{\rho c_p u^*}{T^*} (T_w - T_f) \quad (2.31)$$

where:

$$T^* = Pr n^* \exp(-\Gamma) + [2.12 \ln(n^*) + \beta] \exp\left(\frac{-1}{\Gamma}\right)$$

$$\beta = (3.85 Pr^{1/3} - 1.3)^2 + 2.12 \ln(Pr)$$

$$\Gamma = \frac{0.01(Pr n^*)^4}{1 + 5 Pr^3 n^*}$$

$$Pr = \frac{\mu c_p}{k}$$

Equation (2.31) is useful in calculating heat flux at the wall when the wall temperature is specified as the wall boundary condition. For a specified wall heat flux (q_w) boundary condition, equation (2.31) can be recomposed to estimate wall temperature (T_w).

2.3.2. Two-Layer Turbulence Model

The application of the wall function requires fewer grid points; however, this approach relies on the validity of turbulence equilibrium in the near wall region. In the two-layer turbulence model, the region is divided into the near wall region (viscous sub-layer) and a region away from the wall. A one-equation turbulence model is applied in the near wall region, while standard k - ε turbulence models can be applied for the outer region. The model has the advantage that it does not depend on equilibrium in the near wall region. It requires, however, more grid points in the near-wall region since it uses the viscous sub-layer as reference.

In the near-wall region, one-equation is applied by solving equation (2.22). Turbulence production is calculated from equation (2.18), while dissipation and turbulence viscosity is obtained by modifying equation (2.23):

$$\begin{aligned}\varepsilon &= \frac{k^{2/3}}{\ell_t f_\varepsilon} \\ \mu_t &= \rho c_\mu \sqrt{k} \ell f_\mu \\ \ell_t &= \frac{\kappa \eta}{c_\mu^{3/4}}\end{aligned}\tag{2.32}$$

where f_μ , f_ε , C_μ and ℓ_t are near wall viscosity damping function, damping function, closure coefficient and turbulent length scale, respectively. Yap (1987) proposed the relationships:

$$f_\epsilon = \left[1 - \exp\left(\frac{-y^+}{C_\mu^{1/4} A_\epsilon}\right) \right] \quad (2.33)$$

$$f_\mu = \left[1 - \exp\left(\frac{-y^+}{C_\mu^{1/4} A_\mu}\right) \right]$$

where $A_\epsilon = 3.8$, $A_\mu = 63$ and turbulent Reynolds number is defined as $Re = \rho \cdot \sqrt{k} \cdot n / \mu = y^+ / c_\mu^{1/4}$. By substituting the equation of turbulent length scale into turbulent viscosity in equation 2.32, the viscosity ratio (ratio between turbulent and molecular viscosity) is stated as:

$$\frac{\mu_t}{\mu} = \frac{\rho c_\mu \sqrt{k} \ell_t f_\mu}{\mu} \quad (2.34)$$

The one-equation turbulence model is applicable in the region where f_μ and f_ϵ have values smaller than one (≈ 0.98) which corresponds to values of y^+ equal to 10 and 100 respectively (Figure 2.2 and Figure 2.3). Substituting the value of f_μ into equation 2.34, one obtains a viscosity ratio (μ_t/μ) smaller than 36 (Rodi, 1991), and local turbulent Reynolds number (Rn) smaller than 250 (Chen and Patel, 1988). The criterion for applying one-equation turbulence model then uses either viscosity ratio or local turbulent Reynolds number.

To increase accuracy, Amano (1984) proposed a three-layer model that consists of the viscous sub-layer, buffer layer and overlap layer. The buffer layer is the region between the viscous sub-layer and the overlap layer. The model was tested in separation and reattachment flow, and gave better results compared to the two-layer model.

However, due to the complicated implementation and more computational time, the two-layer model is still preferable for solving flow near solid walls.

2.4 Numerical Methods

This section describes the capabilities of the software package CFX-TASCflow that is used for the simulations in this thesis. The fluid solver, CFX-TASCflow3D, is a co-located Finite Volume Method based on a Finite Element technique (FVMFE). It can simulate the primitive variable formulation of three-dimensional, steady or unsteady, compressible or incompressible, laminar or turbulent fluid flow problems. The software permits the use of four discretization schemes: (1) Upwind Differencing Scheme (UDS); (2) Mass Weighted Scheme (MWS); (3) Modified Linear Profile Skew (MLPS); and (4) pure Linear Profile Skew (LPS). Three k - ϵ turbulence models proposed by Launder-Sharma, Kato-Launder and RNG are supplied to model turbulent flow. The following subsections discuss some details of discretization schemes, co-location of dependent variable storage, solution algorithms and solution requirements in CFX-TASCflow3D.

2.4.1. Discretization Schemes

The equations governing the steady, turbulent, incompressible flows considered in this thesis are:

Continuity:

$$\frac{\partial}{\partial x_j}(U_j) = 0$$

Momentum:

$$\frac{\partial}{\partial x_j}(U_i U_j) = \frac{1}{\rho} \left(-\frac{\partial P}{\partial x_i} + \frac{\partial}{\partial x_j} \left(\mu \frac{\partial U_i}{\partial x_j} + \rho \overline{u'_i u'_j} \right) \right)$$

Energy:

$$\frac{\partial}{\partial x_j}(U_j E_o) - \frac{1}{\rho} \frac{\partial}{\partial x_j} \left(U_i \mu \frac{\partial U_i}{\partial x_j} \right) = \frac{1}{\rho} \frac{\partial}{\partial x_j} \left(-U_j P - \overline{u'_j p} - \overline{u'_j e_o} - Q + \overline{u'_i \tau'_{ij}} \right)$$

Turbulent kinetic energy:

$$\rho U_j \frac{\partial k}{\partial x_j} - \frac{\partial}{\partial x_j} \left(\mu \frac{\partial k}{\partial x_j} + \frac{1}{2} \rho \overline{u'_i u'_i u'_j} - \overline{p' u'_i} \right) = \tau_{ij} \frac{\partial U_i}{\partial x_j} - \rho \epsilon$$

Dissipation of turbulent kinetic energy:

$$\rho U_j \frac{\partial \epsilon}{\partial x_j} - \frac{\partial}{\partial x_j} \left((\mu + \mu_\tau / \sigma_\epsilon) \frac{\partial \epsilon}{\partial x_j} \right) = C_{\epsilon 1} \frac{\epsilon}{k} \tau_{ij} \frac{\partial U_i}{\partial x_j} - C_{\epsilon 2} \rho \frac{\epsilon^2}{k} \quad (2.35)$$

The variables in equation (2.35) are described in Section 2.1. The equations can be cast in the following general form:

$$\frac{\partial}{\partial x_j} (\rho \phi u_j) - \frac{\partial}{\partial x_j} (\Gamma \text{ grad } \phi) = S_\phi \quad (2.36)$$

where:

ϕ = scalar dependent variable

Γ = diffusion coefficient

S_ϕ = Source term

Equation (2.36) consists of convection, diffusion and source terms.

The governing equation is discretized using a Finite Volume Method based on Finite Element technique (FVMFE) in CFX-TASCflow. In finite volume based methods the governing equations are discretized by integrating the governing equation over a fixed control volume constructed around each node in a mesh (Figure 2.4),

$$\int_{cv} \frac{\partial}{\partial x_j} (\rho \phi u_j) dV - \int_{cv} \frac{\partial}{\partial x_j} (\Gamma \text{ grad } \phi) dV = \int_{cv} S_\phi dV \quad (2.37)$$

where \forall is the volume integration.

Using Gauss' divergence theorem, equation (2.37) can be written as:

$$\int_s \left(\int_x \frac{\partial}{\partial x_j} (\rho \phi u_j) dx_j \right) dn_j - \int_s \left(\int_x \frac{\partial}{\partial x_j} (\Gamma \text{ grad } \phi) dx_j \right) dn_j = \int_{cv} S_\phi dV$$

$$\int_s (\rho \phi u_j) dn_j - \int_s (\Gamma \text{ grad } \phi) dn_j = \int_{cv} (S_\phi) dV \quad (2.38)$$

where:

n_j = surface vector in j direction

This results in volume integration of the source term and surface integration of fluxes across control volume surfaces. The FVMFE has the advantage of the geometric flexibility of finite element methods, and conservation properties of finite volume methods.

To perform the volume and surface integrals that arise from the application of the appropriate conservation principle to the control volume in a mesh, appropriate discretization or interpolation schemes must be used for the dependent variables. CFX-TASCflow provides four discretization schemes for the convection-diffusion variables. These schemes are used to provide for the upwind nature of convection processes and to reduce false diffusion produced by locally one-dimensional interpolation. The upwind Differencing Scheme (UDS) is applicable for one-dimensional convection-diffusion problems, but may induce false diffusion when the flow is skew to the mesh lines. For complex geometry, the Skewed Upwind Differencing Scheme (SUDS) is more appropriate, since SUDS was originally developed for skewed three-dimensional flow. The SUDS consists of the Linear Profile Skew (LPS) and the Mass Weighted Scheme (MWS). Linear Profile Skew uses trilinear interpolation of the nodal values on the element surface, while Mass Weighted Scheme interpolates nodal values based on the proportion of mass flow across the element surface. Modified Linear Profile Skew (MLPS) modifies LPS at downstream nodal values to avoid negative coefficients that may cause oscillations in the solution field. By default, CFX-TASCflow blends UDS with MWS, LPS or MLPS with the fraction of UDS = 5 %. The blending system is intended to increase the robustness of the schemes. The fraction of UDS can be adjusted by changing the value of a solution control parameter.

In this thesis, the performance of the discretization schemes is evaluated in Chapter 3. The simulation of laminar flow in a square driven cavity is used to compare all

schemes, laminar and turbulent boundary layer over a flat plate is used to test LPS and MWS, and turbulent flow over backward-facing step simulations test MLPS.

2.4.2. Co-located Method

The pressure term in the momentum equations is treated as a source term when the equations are written in the form of equation (2.36). Depending on how the pressure gradient is evaluated in the source term, an oscillatory velocity field that is caused by the presence of a physically unrealistic pressure field may arise. One commonly used method to avoid this problem is grid staggering, where velocity is stored on the element surfaces and pressure is stored at the nodes. Staggered grids are inconvenient for complex geometry, since this technique is only applicable for meshing that is aligned with a coordinate system.

An unequal-order method is more appropriate for complex geometry, because it is not affected by element orientation with respect to the coordinate axes. Unequal-order methods store pressure on a coarser grid than velocity. Since pressure and velocity are located at control volume faces, the oscillatory solution can be eliminated. A disadvantage of an unequal-order method is the inaccuracy of the pressure calculation, since pressure is stored on a coarser grid. Furthermore, different control volumes would be used to satisfy conservation of mass and conservation of momentum, with no guarantee that mass conservation is satisfied over momentum control volumes.

To increase the accuracy of the pressure calculation, equal-order methods store pressure and velocity at the same location. The oscillatory solution is eliminated by providing some form of pressure-velocity coupling. CFX-TASCflow uses shape functions to obtain pressure gradients as proposed by Schneider and Raw (1987). The discretized momentum equations are used to express velocity components at a node in terms of a pressure gradient obtained from a shape function and the neighbouring nodal velocity components. The equations are then substituted into the mass conservation equation to obtain a coupled pressure-velocity equation. Figure 2.5 describes the algorithm to solve for u , v , w and p implemented in CFX-TASCflow.

2.4.3. The linear solver

The discretization process converts the governing equations into a set of non-linear, coupled and simultaneous algebraic equations that can be written in the matrix form:

$$[A]\{\phi\} = \{b\}$$

The coefficient matrix $[A]$ is evaluated using the best available estimate of all required variables. The linear solver simultaneously solves the algebraic equations to obtain the solution. Figure 2.6 shows the solution algorithm for turbulent flow, with wall functions employed for the treatment of near wall turbulence. CFX-TASCflow uses a relaxation scheme to solve the discretized equations, and a multigrid algorithm to accelerate the solution.

The relaxation scheme of CFX-TASCflow is an Incomplete Lower Upper (ILU) factorisation solver. The coefficient matrix $[A]$ is transformed into lower $[L]$ and upper $[U]$ triangular matrixes.

$$[A]\{\phi\} = [L][U]\{\phi\}$$

If the actual solution is approximated by:

$$\phi = \phi^n + \phi'$$

where:

ϕ^n = approximate solution

ϕ' = correction

The residual on the recent solution $\{R\}$ can then be expressed as:

$$[A]\{\phi\} = \{R\}$$

Initially, ϕ^n is specified and residual $\{R\}$ on the first iteration is calculated as follows:

$$\{R\} = \{b\} - [L][U]\{\phi^n\}$$

The relaxation process is performed until obtaining a residual target.

$$\{y\} = [L]^{-1}\{R\}$$

$$\{\phi'\} = [U]^{-1}\{y\}$$

The solution is updated by:

$$\{\phi^{n+1}\} = \{\phi^n\} + \{\phi'\}$$

The process can be repeated until $\{R\}$ is sufficiently small.

$$\{R\} = [L][U]\{\phi'\}$$

The relaxation scheme employed in CFX-TASCflow is an effective method for solving the types of equations that arise in fluid flow simulations. Since the coefficient

matrix is not exact, as it is evaluated using estimates or currently available values for properties, velocities etc., a direct solution of the set of coupled discretized equations is not practical. Iterative solution schemes are the preferred alternative. A limitation of any relaxation scheme, however, is that the solver will smooth the error, but only on the fine scale, i.e. over localised nodes. Since the error is composed of both short and long wavelength components (see Figure 2.7), the relaxation scheme will require a large number of iterations to reduce the long wavelength components on a fine mesh. The presence of long wavelength components is also more significant, when the mesh contains a large number of nodes. A means of accelerating the flow solution is multigrid.

Multigrid is based on the fact that the coarse grid only contains long wavelength error, and the fine grid contains short wavelength error (Figure 2.8). Multigrid combines the advantages of both grids to eliminate the long wavelength error and accelerate the solution process (Phillips and Schmidt, 1984). CFX-TASCflow uses Additive Correction Multigrid algorithm as proposed by Hutchinson and Raithby, 1986. The algorithm starts with grid coarsening, bounding several elements into a new larger element, for several levels. When the iteration on the original (fine) grid structure has slow convergence, multigrid will stop the current iteration and start a new iteration on the higher level of grid structure, which is coarser than the original grid. When convergence slows on this level, iteration is commenced on the next higher level. This is continued until the highest, i.e. coarsest grid, level is reached. The next process is to return to successively lower level (finer meshes) until reaching the original grid structure. One cycle of the process

will form a V-cycle. In addition to V-cycle, CFX-TASCflow also provides a W-cycle for multigrid (Figure 2.9).

2.4.4. CFX-TASCflow software system

Like any commercial CFD package, CFX-TASCflow provides software for pre-processing, post-processing and a fluid flow solver. Pre-processing includes building the grid structure with TASCgrid, checking the grid structure and specifying initial conditions in TASCtool, and defining boundary conditions and governing equations in TASCbob3D. A file with default name PRM specifies all solution control parameters required for running the solver. The solution results consist of files with the default names: RSO for storing flow variables, OUT for storing convergence history, and IR1 and IR2 for storing data of the restarting process. Post-processing, extracting data of simulation results (RSO), can be performed by TASCtool. The interaction between software is shown in Figure 2.10. In addition to the mentioned software, CFX-TASCflow also provides a Graphical User Interface (GUI) that is interactively able to handle pre- and post-processing.

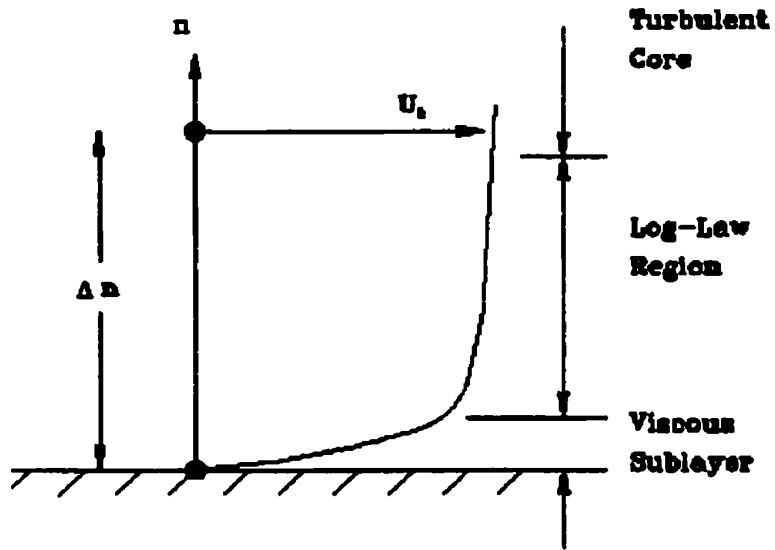


Figure 2.1: Velocity profile in the near wall region (reproduced from CFX-TASCflow, 1999a).

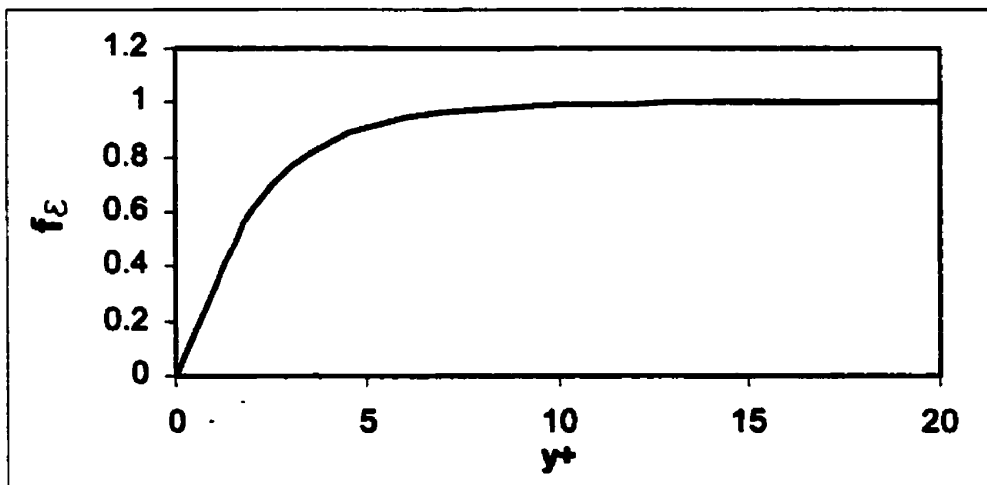


Figure 2.2: Distribution of f_ϵ over vertical distance, y^+ .

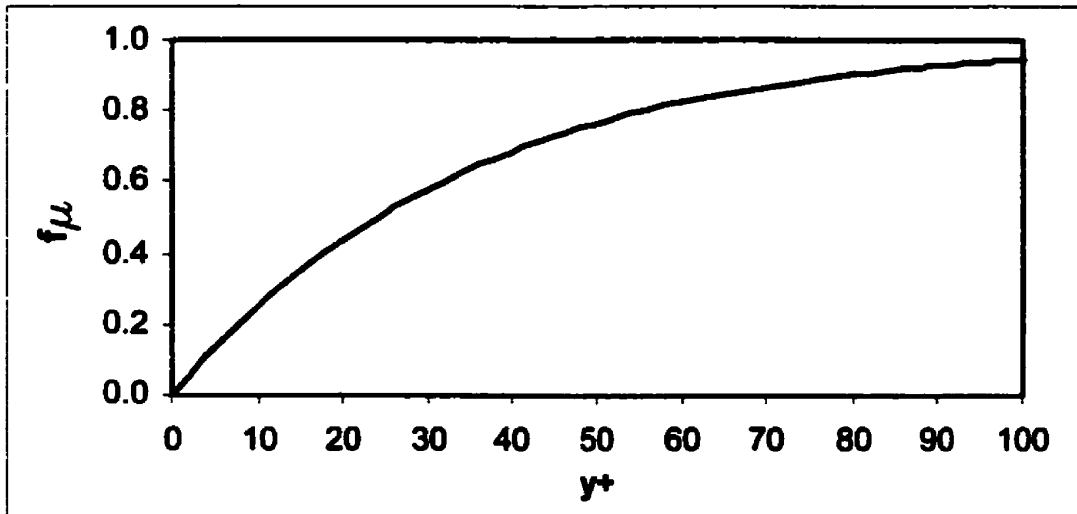


Figure 2.3: Distribution of f_{μ} over vertical distance, y^+ .

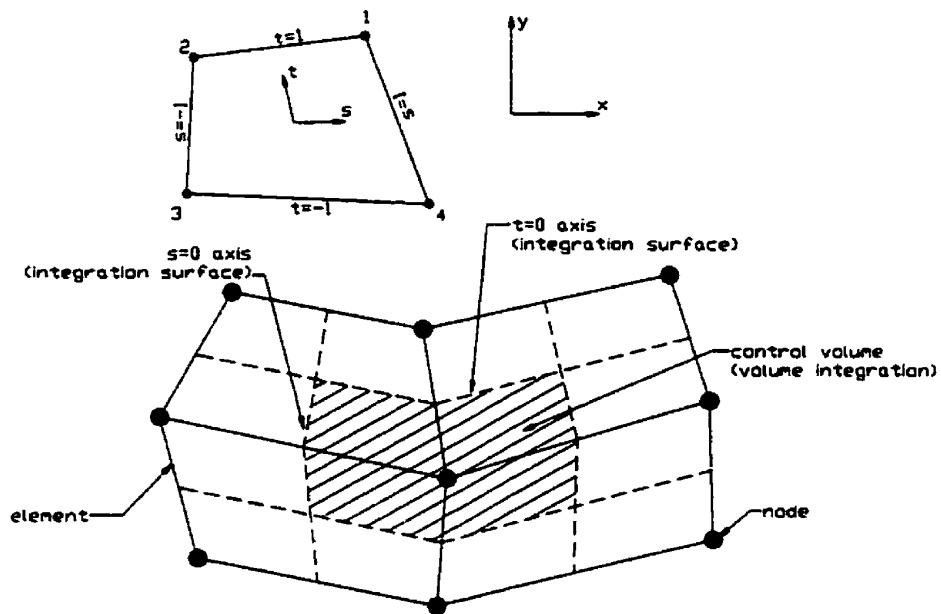


Figure 2.4: The definition of a two-dimensional control volume and integration surfaces.

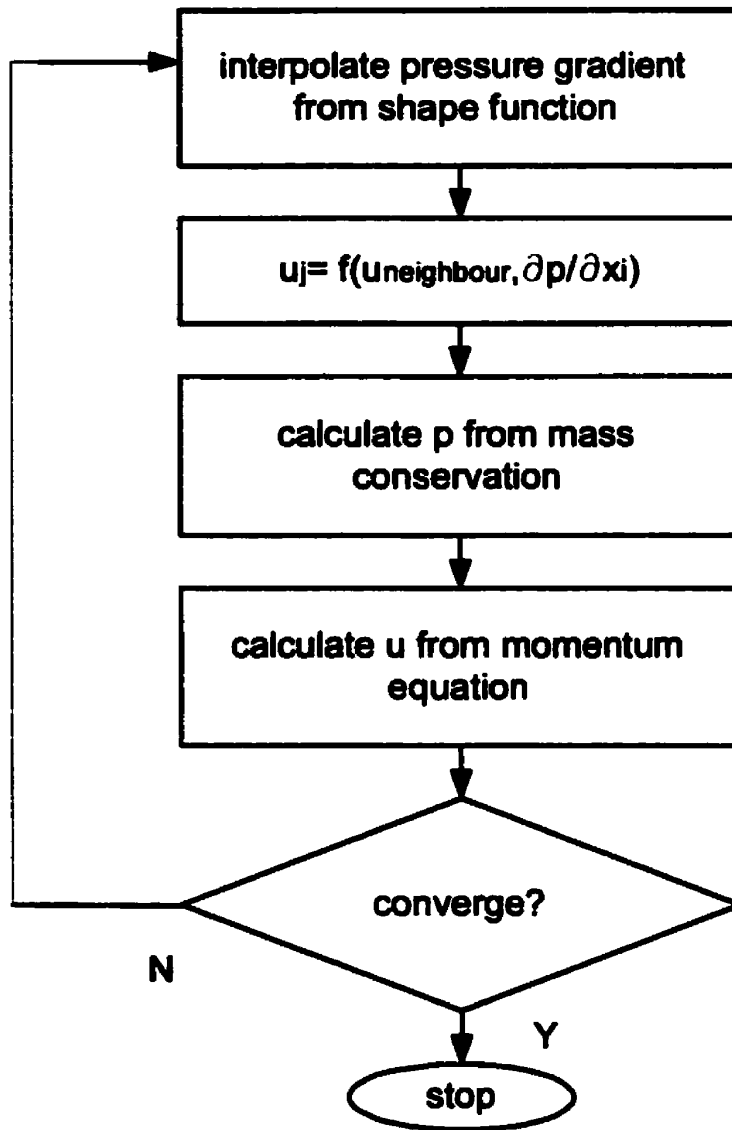


Figure 2.5: Algorithm for the equal-order method used for solving u , v , w and p .

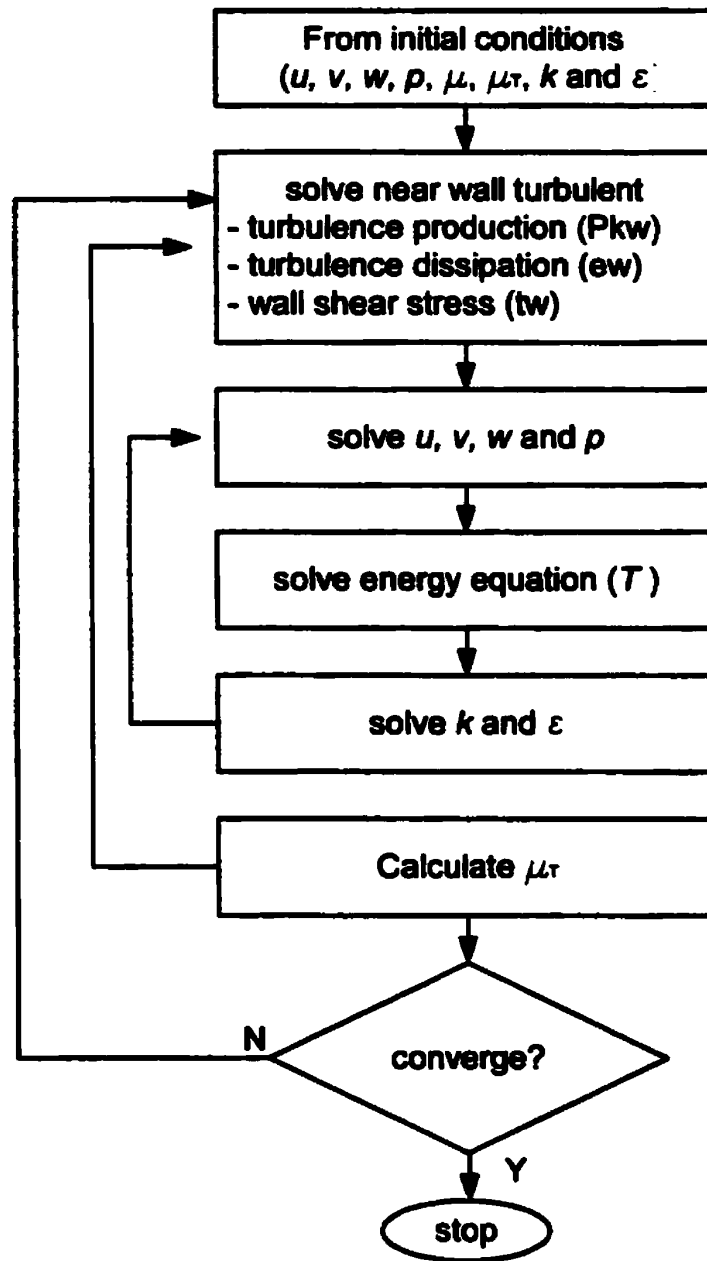


Figure 2.6: Solution algorithm for turbulent flow.



Figure 2.7 : Residual error distribution along a grid line (reproduced from CFX-TASCflow, 1999a).

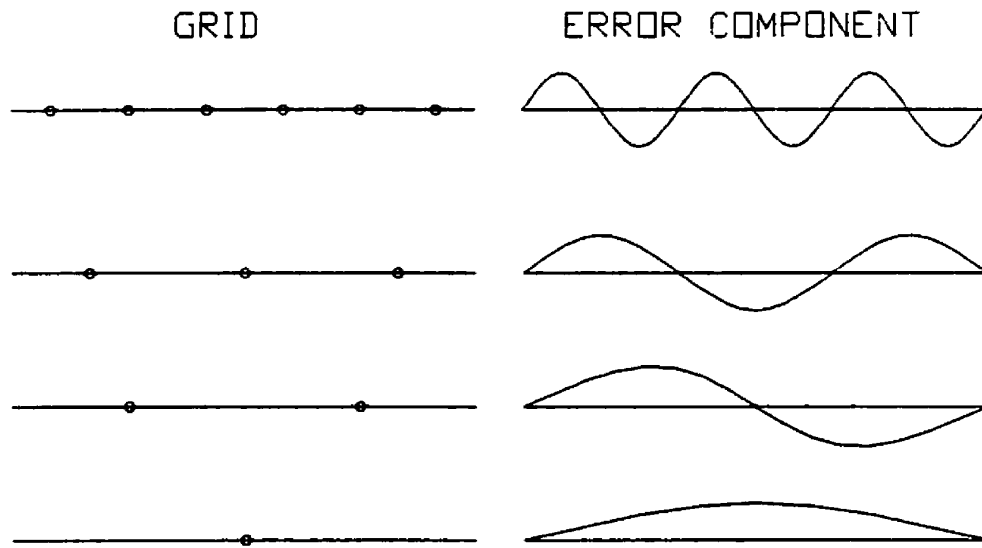


Figure 2.8: One-dimensional grid hierarchy and error components line (reproduced from CFX-TASCflow, 1999a).

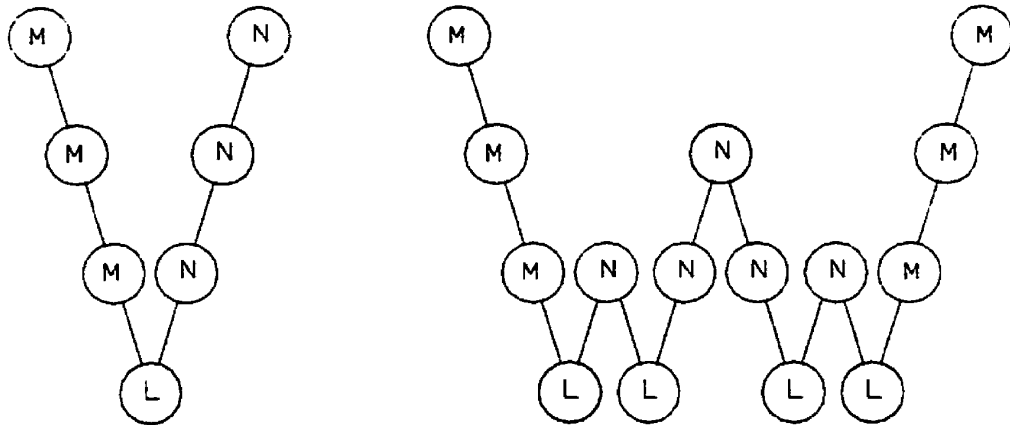


Figure 2.9: V and W cycle of multigrid line (CFX-TASCflow, 1999a).

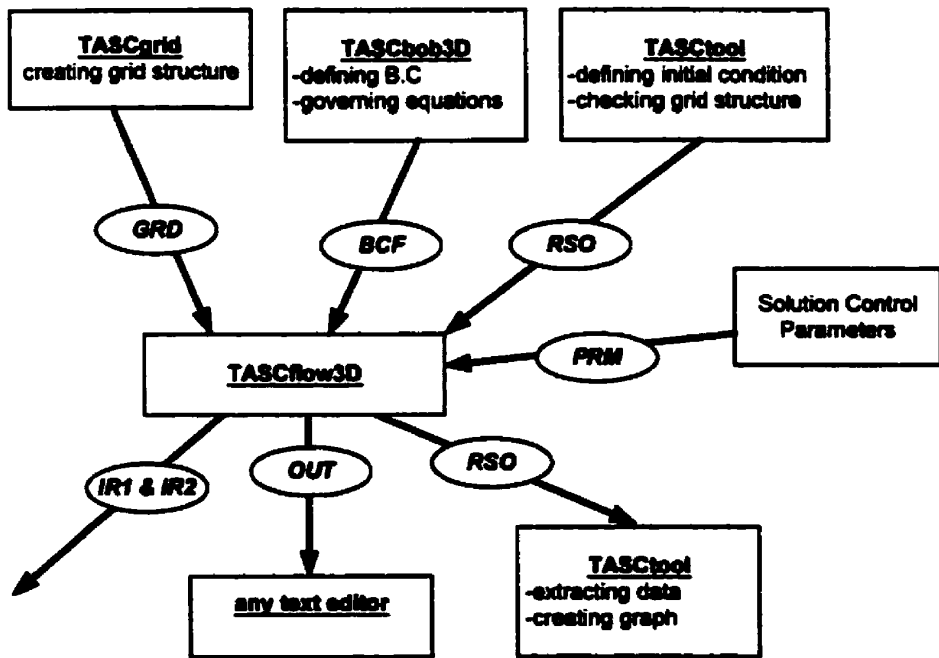


Figure 2.10: Structure of CFX-TASCflow line (CFX-TASCflow, 1999a)

3. Software Validation

Several test flow problems were solved to validate the CFD software. The first simulation is for flow in a square driven cavity at Reynolds numbers of 100 and 400. This problem evaluates the ability of the software to handle recirculating flows. Laminar and turbulent boundary layers over a flat plate are next compared to standard solutions. The performance of the software for solving flow near a wall, using wall function and a two-layer turbulence model, are evaluated in this instance. The last problem is for flow over a backward facing step. This problem is intended to evaluate the performance of the proposed turbulence model in a flow with adverse pressure gradients.

3.1. Flow in a square driven cavity

Flow in a square driven cavity is commonly used to validate numerical methods in computational fluid dynamics. Baliga et al. (1983) used the problem to evaluate an unequal-order method. Schneider and Raw (1987b) used this problem to compare the performance of equal- and unequal-order methods. Hookey (1986) modified the interpolation function for an equal-order method to allow the flexibility of a source term in that function, and compared the simulation results with Baliga et al. (1983).

3.1.1. Problem Definition

In a square driven cavity, the movement of a sliding lid drives a laminar recirculation flow. The flow is steady, two-dimensional and laminar. The calculation

domain is bounded by three fixed walls and a lid that moves along the positive x-direction with constant velocity, u (see Figure 3.1).

The flow domain consists of $21 \times 21 \times 3$ nodes in x, y and z directions, respectively (Figure 3.2). A finer grid of $41 \times 41 \times 3$ nodes is used to evaluate the improvement in accuracy with reduction in grid size. All elements are of uniform size. The use of three elements in the z direction is the consequence of the discretization scheme used by CFX-TASCflow which assumes a three-dimensional problem. The results at Reynolds numbers of 100 and 400 are compared to the simulation of Baliga and Patankar (1983). The main comparison is for the velocity profile along the vertical centreline.

3.1.2. Flow simulation

The simulation uses custom fluid properties specified as:

$$\rho = 1 \text{ kg/m}^3$$

$$\mu = 0.01 \text{ kg/(m.sec)}$$

Reynolds number of 100 and 400 are obtained by specifying the length (L) equal to 1 meter and velocity equal to 1 and 4 m/sec, respectively. The solution control parameters are:

$$\text{Maximum residual error} = 1 \times 10^{-6}$$

$$\text{Time step} = 0.1 \text{ second}$$

$$\text{Number of time steps} = 100$$

Other default parameters are the use of the multigrid algorithm and physical advection correction. Use of the multigrid algorithm accelerates residual error reduction in the grid structure and physical advection correction takes into account the influence of advection and diffusion. The Upwind Difference Scheme (UDS), Mass Weighted Scheme (MWS), Modified Linear Profile Skew (MLPS) and Linear Profile Skew (LPS) discretization schemes are used in solving the flow problem.

Initial conditions for the problem are zero velocity and uniform pressure in the cavity. The movement of the sliding lid causes the fluid motion. After performing several time step iterations, the solution will converge and reach the target residual error.

3.1.3. Discussion of results

The simulations using the four-discretization schemes reach the convergence criteria at time step iteration 65. The center line velocity distribution for $Re=100$ is in close agreement with the results of Baliga for all discretization schemes (Figure 3.3a). Since the results are in good agreement, the computations using the grid size $41 \times 41 \times 3$ were not performed at this Reynolds number. Due to a higher local Peclet number, the velocity distribution for $Re = 400$ has a small difference with Baliga's solution, especially for grid size $21 \times 21 \times 3$ (Figure 3.3b) with the errors less than 6%. Hookey (1986) also reported small differences when using a similar grid size and triangular elements.

For $Re=400$, the use of Linear Profile Skew (LPS) gives the best results when compared to those generated by the Upwind Difference Scheme (UDS), Mass Weighted Scheme (MWS) and Modified LPS (MLPS) (Figure 3.3 b). This agrees with the literature review that LPS is superior in accommodating the influence of diffusion and advection. The accuracy of the solution is increased on the $41 \times 41 \times 3$ mesh. Figure 3.4 shows that all discretization schemes give good agreement with the solution of Baliga with the $41 \times 41 \times 3$ grid.

The velocity contours of Figure 3.5 (a) show that the vortex center at $Re=100$ is displaced to the right side. The velocity vectors in Figure 3.5 (b) show a secondary flow in the bottom right region of the cavity, and is consistent with the results of Hookey (1986). For the Reynolds number of 400, the vortex center is closer to the center of the cavity, because the inertial force is more dominant (Figure 3.6 a). The secondary flow indicated by the velocity vectors appears in both bottom corners (Figure 3.6 b).

3.2. Boundary layer on a Flat plate

The simulation of a boundary layer on a flat plate is useful to determine the effectiveness of the software to resolve the near-wall region, and estimate wall shear stress and wall heat transfer. A boundary layer on a flat plate can be simulated by a uniform flow over a flat wall (Figure 3.7). The boundary layer develops from the leading edge and grows with downstream distance. A discontinuity is always present at the

leading edge due to the abrupt change in velocity from the freestream value to zero. In numerical calculations, the discontinuity affects the accuracy of flow properties near the leading edge. Although most practical flows are turbulent, a laminar boundary layer can be used for preliminary study and validation. The laminar solution is available in either analytical or empirical form (Blasius, 1908) as shown in Figure 3.8, and is useful to benchmark the CFD software.

The Blasius solution for the laminar boundary layer is used to validate the numerical results from the present simulation. In addition to the velocity profile, the boundary layer thickness, skin friction coefficient and Nusselt number distribution are used for the validation. The Blasius solutions for these parameters are:

$$\begin{aligned}\frac{\delta_{99}}{x} &= 5.0 \text{Re}_x^{-1/2} \\ C_{f,x} &= \frac{0.664}{\text{Re}_x^{1/2}} \\ Nu_x &= 0.332 \text{Re}_x^{1/2} \text{Pr}^{1/3}\end{aligned}\tag{3.1}$$

where:

$$\begin{aligned}\text{Re}_x &= \frac{u_o x}{\nu} \\ 0.6 &< \text{Pr} < 50\end{aligned}$$

Unlike for a laminar boundary layer, there are no analytical solutions for a turbulent boundary layer. Most parameters are obtained experimentally, and some correlations are given below (Incropera and Dewitt; 1990):

$$\frac{\delta_{99}}{x} = 0.37 \text{Re}_x^{-1/5}$$

$$C_{f,x} = \frac{0.0592}{\text{Re}_x^{1/5}} \quad (3.2)$$

$$Nu_x = 0.0296 \text{Re}_x^{4/5} \text{Pr}^{1/3}$$

The correlations are valid for:

$$5 \times 10^5 < \text{Re} < 10^7$$

$$0.6 < \text{Pr} < 60$$

To obtain a good simulation of the boundary layer over a flat plate, certain requirements must be met. The height of the flow domain should be at least greater than ten times the maximum boundary layer thickness in order to accommodate boundary layer growth along the flat plate and minimize any adverse pressure gradient effects. The first node from the wall should be in the viscous sublayer to obtain a linear relationship for calculating temperature and velocity gradients at the wall. The distance from the wall to the first node is strongly dependent on the flow condition, whether the flow is turbulent or laminar, and the Reynolds number. For incompressible laminar flow, the first node should be smaller than $\eta=1.73$ (Schlichting, 1979), where:

$$\eta = y \sqrt{\frac{U_{\tau}}{\nu x}} \quad (3.3)$$

For turbulent boundary layers, the distance is smaller since the viscous sublayer is much smaller in this instance. The region usually exists up to five wall units (CFX-TASCflow, 1999a), where the wall unit is defined as:

$$y^+ = \frac{y}{\sqrt{\frac{\tau_{wall}}{\rho}}} \quad (3.4)$$

Bardina et al. (1997) suggested a value of 0.1 wall unit for the first node and sixty nodes within the boundary layer when the flow is incompressible. The accuracy of the skin friction calculation with the number of nodes within the boundary layer is presented in Figure 3.9 for some turbulence models.

When the turbulent boundary layer is in equilibrium, the wall function relationship can be used to reduce the number of nodes. The wall function uses the log-law region to interpolate for the velocity and temperature gradient at the wall. Since the log-law region is applicable in the range $30 < y^+ < 300$, the wall function requires fewer nodes.

3.2.1. Problem Definition

Flow simulation consists of laminar and turbulent boundary layers with Reynolds numbers of 10^5 and 10^7 , respectively. The length of the flow domain is 1.3 m with the

wall occupying the last 1.0 m of the domain (Figure 3.10). The height of the flow domain is approximately ten times the boundary layer thickness at the end of the plate. The grid structure is broken into a boundary layer and free stream region, with heights of two times and eight times boundary layer thickness, respectively. The nodes are not uniform, with a denser resolution close to the wall, and coarser in the freestream with a smooth transition between the two. Grid refinement around the leading edge is required to smooth the transition from the free stream to the boundary layer (see detail of grid refinement in Figure 3.10). The final form of the grid distribution is shown in Figure 3.11. The parameters for the boundary layer simulations are given in Table 3.1.

Table 3.1: Parameters for laminar and turbulent boundary layer over a flat plate

Parameter	Laminar	Turbulent
ρ (kg/m ³)	1	10
μ (N.s/m ²)	10 ⁻⁵	10 ⁻⁶
c_p (J/kg.K)	1000	1000
k (W/m.K)	10 ⁻³	10 ⁻³
u_∞ (m/s)	1	1
Re	10 ⁵	10 ⁷
Pr	1	1
δ (m)	0.016	0.015
Distance of the first node from the wall (Z)	$Z < 1.73 \eta$	$Z < 4y^+$, log-law
Wall Temperature (K)	400	500

3.2.2. Flow simulation

Inflow boundary condition on the left side of the flow domain is specified as uniform velocity, and the outflow boundary condition on the right side is specified as constant pressure at atmospheric condition. A symmetric boundary condition is specified for the first 0.3 m of the bottom of the flow domain, and the rest is a wall boundary condition. The element aspect ratio, defined as the ratio between the longest and shortest side of the element, has a maximum value of 22, and the smallest value of 2 occurs at the top of the flow domain. High aspect ratio elements along the streamwise direction only affects the region around the leading edge, since the change of flow direction in the location beyond the leading edge is small (Figure 3.11). To accommodate the large gradients in the vicinity of the leading edge, the element aspect ratio is reduced to one through grid refinement around the leading edge. The discretization scheme is not critical in the simulation, since flow direction is nearly aligned with the grid orientation. The simulations use Mass Weighted Scheme and Linear Profile Scheme. The simulation results for laminar and turbulent boundary layers are presented as pressure and temperature contours (Figure 3.12), and velocity vectors and contours (Figure 3.13). The intensive change of pressure at the leading edge is caused by the abrupt change of velocity direction. The temperature in a turbulent boundary layer changes more rapidly than in a laminar boundary layer at the wall causing a higher heat transfer for a turbulent boundary layer.

The temperature gradient used to calculate the heat flux in equation (3.5) can be obtained from the linear temperature profile in the viscous sub-layer region. The heat transfer calculation for the laminar boundary layer can be calculated accurately, since the boundary layer is dominated by the viscous sub-layer region (Figure 3.13c). For the turbulent boundary layer, however, the viscous sub-layer region is in the location $0 < y^+ < 5$ (Figure 3.13d). This requires an increase in the number of nodes close to the wall to estimate temperature gradient. Similar conditions are also applicable to obtain the velocity gradient in calculating skin friction from equation (2.6).

3.2.3. Discussion of result

The simulation results for the velocity profile, Nusselt number and skin friction distributions are presented in this section. The velocity profile for the turbulent boundary layer is not presented, since it only contains eight nodes in the boundary layer. Laminar boundary layer velocity profiles at several streamwise locations are compared with the Blasius velocity profile. Nusselt number and skin friction distributions are compared with equation (3.1) for the laminar case and equation (3.2) for the turbulent boundary layer. Heat flux (q'') is obtained from the heat conduction at the wall by assuming a linear temperature profile:

$$q'' = -k \left. \frac{\partial T}{\partial z} \right|_{z=0} \tag{3.5}$$

$$\left. \frac{\partial T}{\partial z} \right|_{z=0} = \frac{T_1 - T_2}{z_1 - z_2}$$

The Nusselt number is obtained from:

$$Nu = \frac{hx}{k} = \frac{q''}{(T_w - T_\infty)} \frac{x}{k}$$

The skin friction is obtained from:

$$C_f = \frac{\mu \left. \frac{\partial u}{\partial z} \right|_{z=0}}{0.5 \rho U_\infty^2} \quad (3.6)$$

where:

$$\left. \frac{\partial u}{\partial z} \right|_{z=0} = \frac{u_1 - u_2}{z_1 - z_2}$$

The simulations for the laminar velocity profiles are, in general, in good agreement with the Blasius profile (Figure 3.8). The velocity profile at $x=0.5077$ meters from the leading edge has the largest difference with the Blasius profile, while the velocity profile at the end of the plate has the smallest difference. The number of nodes within the boundary layer region determines the accuracy of the interpolation of the velocity profile. Since the boundary layer at the end of the plate contains more nodes, its interpolation is better, resulting in a more accurate simulation.

The Nusselt number (Figure 3.15) and skin friction (Figure 3.16) distributions for the laminar boundary layer also are in good agreement with the theoretical solution. The simulation has a tendency to underestimate the value at the leading edge and overestimate at the rear of the plate. The calculated Nusselt number differs from the theoretical value by less than two percent, while the difference in skin friction prediction is in error by seven percent. Rounding error during computational iterations may cause errors in estimating temperature and velocity, since the software is only able to store single precision variables (the calculation is also performed on the second grid, and the results are the same).

For the turbulent boundary layer, the first node beyond the wall should be smaller than four times the wall unit. For $Re=10^7$, the wall unit (y^+) is 2.94×10^{-6} , and the distance is 1.18×10^{-5} m. Since the maximum aspect ratio of the element is 100, the number of nodes along the streamwise direction should be more than $1.3/(100 \times 2.36 \times 10^{-5}) = 1102$ nodes to satisfy this condition. Due to limitations of computer memory and computational time, it is impossible to perform the simulations with the required number of nodes.

By assuming an equilibrium condition, the wall function is used to reduce the number of nodes. For preliminary analysis, a coarse grid structure is used to compare the performance of the turbulence model in estimating Nusselt number and skin friction. Three models, Standard, Kato and RNG, are used for the simulations. Standard and Kato

models have the same accuracy in estimating skin friction, while the RNG model has a larger error (Figures 3.17 and 3.18). From the preliminary simulations, the standard turbulence model is used for simulations with a finer grid structure.

As stated earlier, the wall function is valid for the boundary layer region $30 < y^+ < 500$. For evaluating the influence of the distance of the first node on the accuracy of the results, simulations were performed with node distances ranging from 25 to 500 wall units. Figures 3.19 and 3.20 show that Nusselt number and skin friction for the second node distance ($y = 1.8 \times 10^{-4}$ m) produces the most accurate estimation. The first node distance ($y = 6.0 \times 10^{-5}$ m) underestimates and the remaining overestimate.

Figure 3.21 shows the distances of the first node in wall units from leading edge to the end of plate. By neglecting the leading edge region, the first node distances (in term of wall units) are nearly constant. The first and second nodes are located at 25 and 75 wall units, while the remaining are located in the range of 150 to 450 wall units. It can be concluded that accurate calculation for wall function with $Re=10^7$ can be obtained in the range 50 to 150 wall units.

3.3. Backward-Facing step

Two-equation turbulence models are preferred over algebraic and one-equation turbulence models since they are applicable for any flow configuration without changing any closure coefficients or parameters. Two-equation models also require less

computational resources compared to Large Eddy Simulations. However, most two-equation turbulence models suffer inaccuracy in flows with low Reynolds numbers and adverse pressure gradient. A common problem for validation in adverse pressure gradient is flow over a backward facing step (Wilcox, 1993). Peng, et al. (1997), also used a backward facing step to validate their Low-Reynolds-Number $k-\omega$ model.

In a backward facing step, flow separates at the step and reattaches at a specific distance downstream of the step (Figure 3.22). The reattachment length, skin friction along the separated flow and the distribution of turbulence kinetic energy (k) and velocity along the crossflow direction are used for validating the turbulence model. Generally, $k-\omega$ models predict reattachment length more accurately (3 % after measured point) than $k-\epsilon$ models (20% before measured point) (Wilcox, 1993). The $k-\epsilon$ models undershoot the velocity distribution along the crossflow direction in the near-wall area and both $k-\epsilon$ and $k-\omega$ models overshoot at locations away from the wall. Both models also overestimate turbulent kinetic energy along the separation region (Peng, et al. 1997).

3.3.1. Problem Definition

The flow domain is the same as the simulations of Peng et al. (1997), for a backward facing step. The expansion ratio between inlet and outlet dimension (H/h) is six. The Reynolds number, based on inlet height, is 5050. The length of the domain is one hundred times the inlet height. Figure 3.22 illustrates the flow configuration and the

location of flow reattachment. Figure 3.23 shows the grid structure for the simulations. The simulations use Modified Linear Profile Skew (MLPS) as discretization scheme, three turbulence models, Sharma-Lauder, Kato and RNG model and the wall function for the near-wall region. The simulations are compared with experimental data of Restivo, (1979) and the simulation result of Peng et al. (1997).

Table 3.2 Comparison of the estimated reattachment length

No	Result of	Reattachment Length
1	Experiment (Restivo, 1979)	6.12 W
2	Peng, et al. (1997)	6.4 W
3	Standard model	6.2 W
4	Kato model	6.6 W
5	RNG model	5 W

3.3.2. Discussion of result

Table 3.2 shows the comparison of the estimated reattachment length that is based on the height of backward-facing step (W). The simulation results are compared with the experimental result of Restivo (1979). Standard model has the best performance by overestimating reattachment length by less than two percent, followed by Peng's simulation and Kato model by overestimation five and eight percent, respectively. Unlike the other simulation results, RNG model underestimates reattachment length by eighteen percent.

The mean streamwise velocity profiles are in reasonable agreement with the experimental data (Figure 3.24). At location $x/H=30$, the calculated velocity profile has a significant difference with the experimental profile. The Standard and Kato turbulence models have the same accuracy as Peng's result, while the RNG model behaves poorly. Near the step (at $x/H=5$), Standard and Kato models have a better accuracy in estimating the peak velocity.

Unlike mean streamwise velocity, all models over-estimate the turbulent kinetic energy (Figure 3.25). At $x/H=5,10,15$ and 20 , Standard and Kato models are more accurate compared with Peng's simulation. Near the reattachment location ($x/H=30$), Peng's calculation has a better accuracy, and RNG model is the most accurate. The source of error in estimating turbulent kinetic energy is the high expansion ratio ($H/h=6$) as the source of adverse pressure gradient. It is still not clear how the adverse pressure gradient affects the accuracy of the solution. However, it is believed that the selection of the numerical scheme, grid structure and turbulence model contributes to the inaccuracy of the solution. Peng et al. (1997) reported a better estimation of turbulent kinetic energy with a lower expansion ratio ($H/h=1.2$).

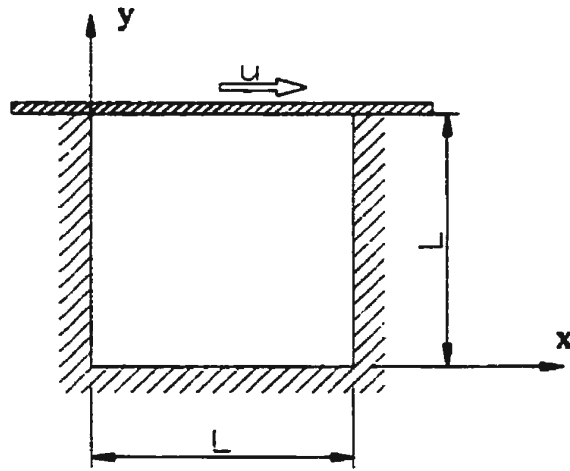


Figure 3.1: Flow domain in a square driven cavity.

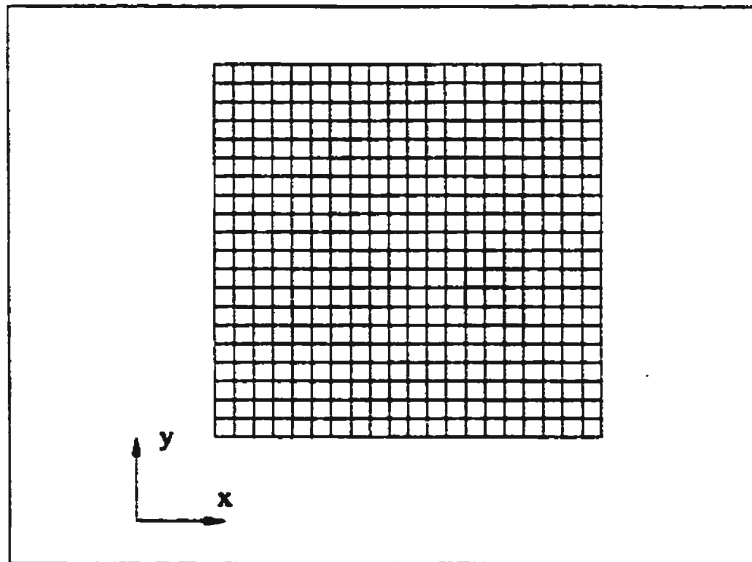
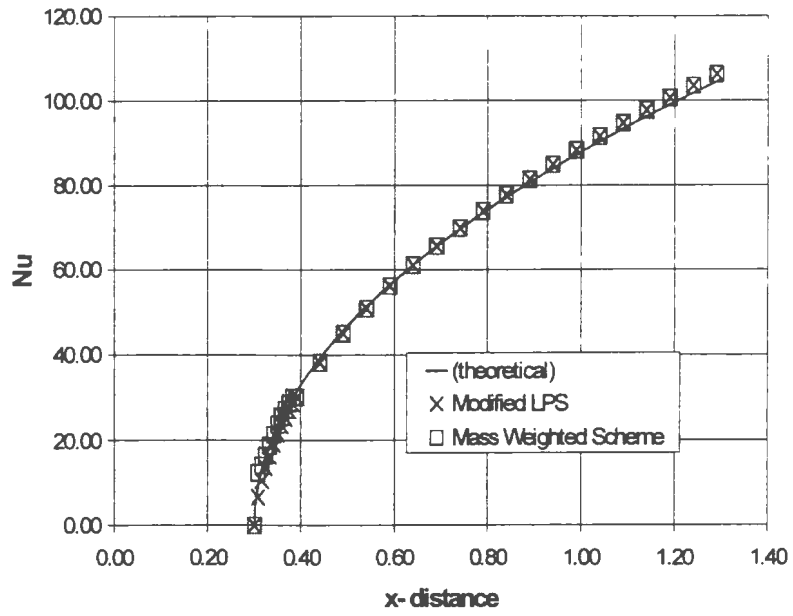
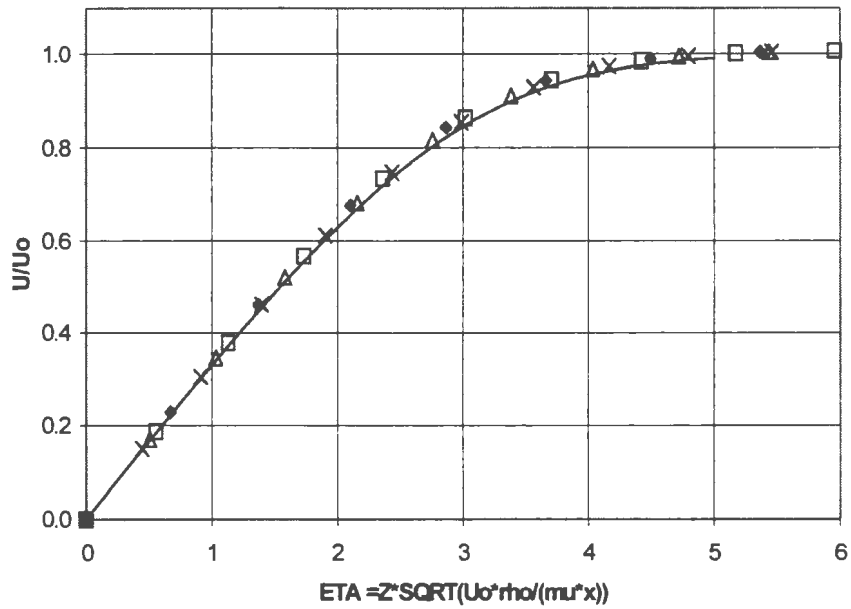


Figure 3.2: Grid structure for flow in square driven cavity.



(a)



(b)

Figure 3.3: U-velocity distribution along $x=0.5$ for different discretization schemes: a). Re=100 and b). Re=400.

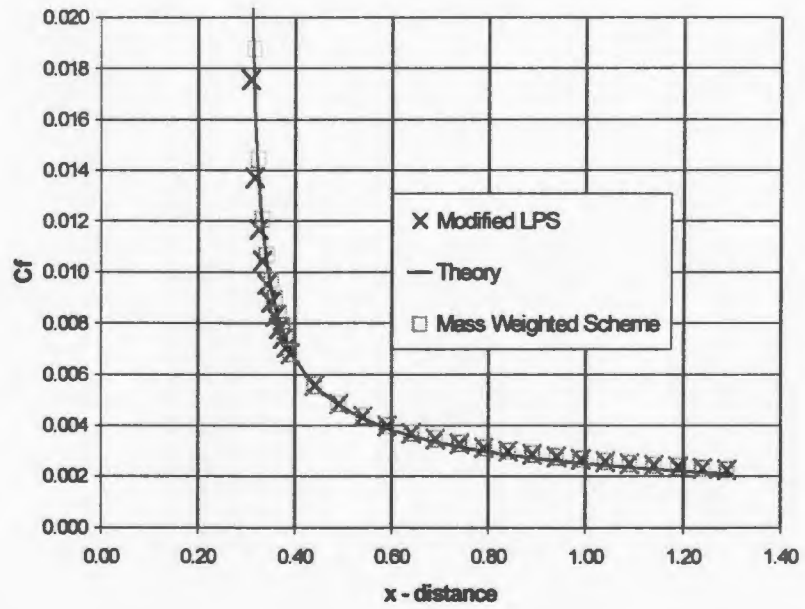


Figure 3.4: U-velocity distribution along $x=0.5$ for different discretization schemes at grid size $41 \times 41 \times 3$ and $Re=400$.

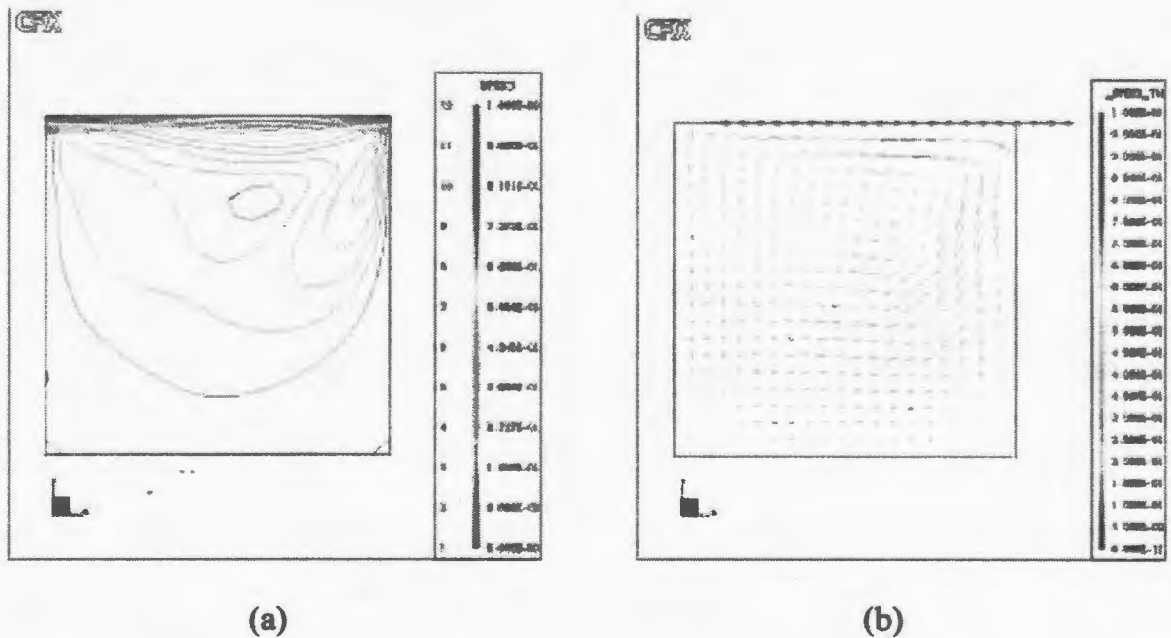


Figure 3.5: Velocity contour (a), and velocity vector (b) for $Re=100$.

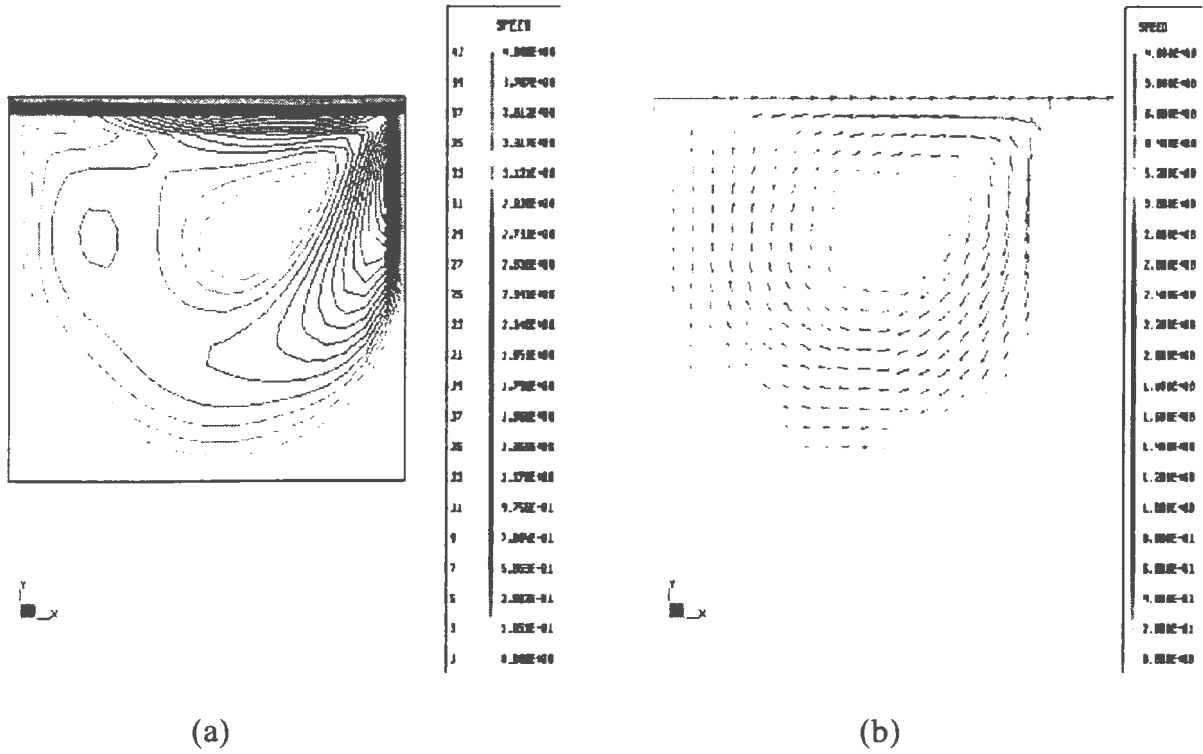


Figure 3.6: Velocity contour (a), and velocity vector (b) for $Re=400$.

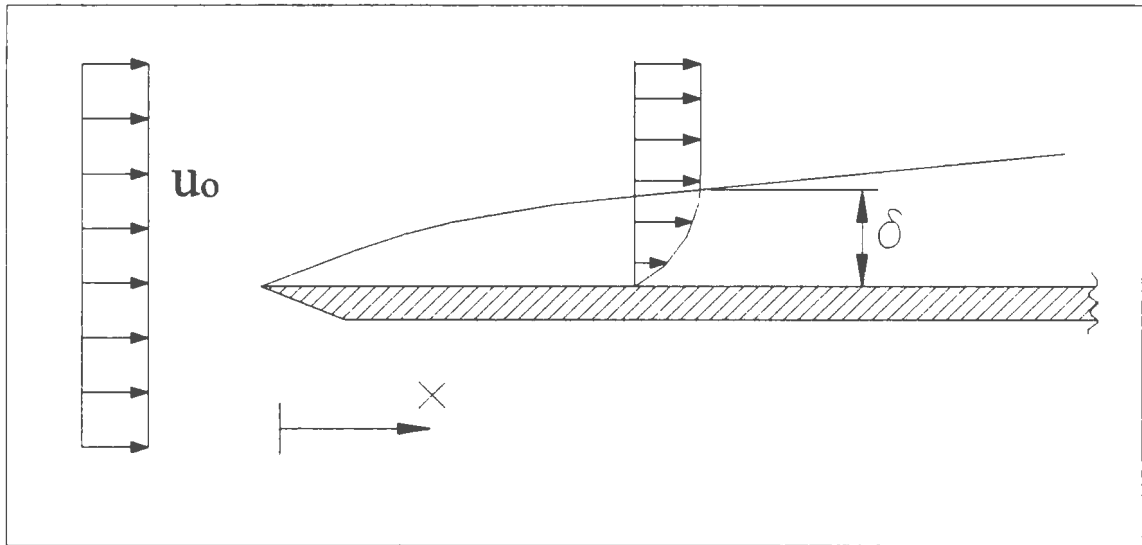


Figure 3.7: Schematic of boundary layer over a flat plate.

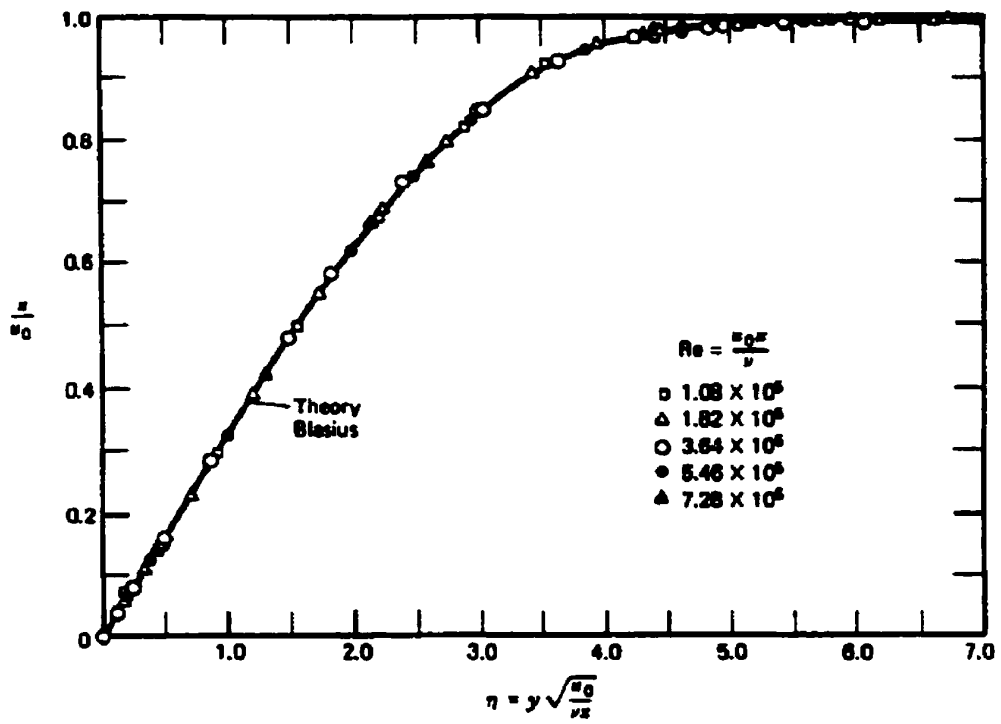


Figure 3.8: Blasius velocity profile for laminar boundary layer (reproduced from Panton, 1984).

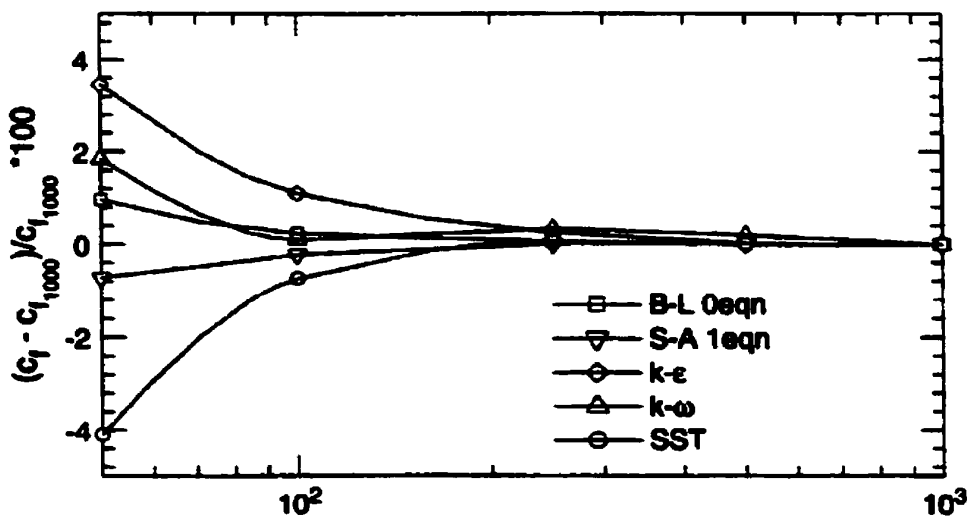


Figure 3.9: The sensitivity of skin friction calculation to the number of nodes within boundary layer for some turbulence models (rep. from Bardina et al. 1997).

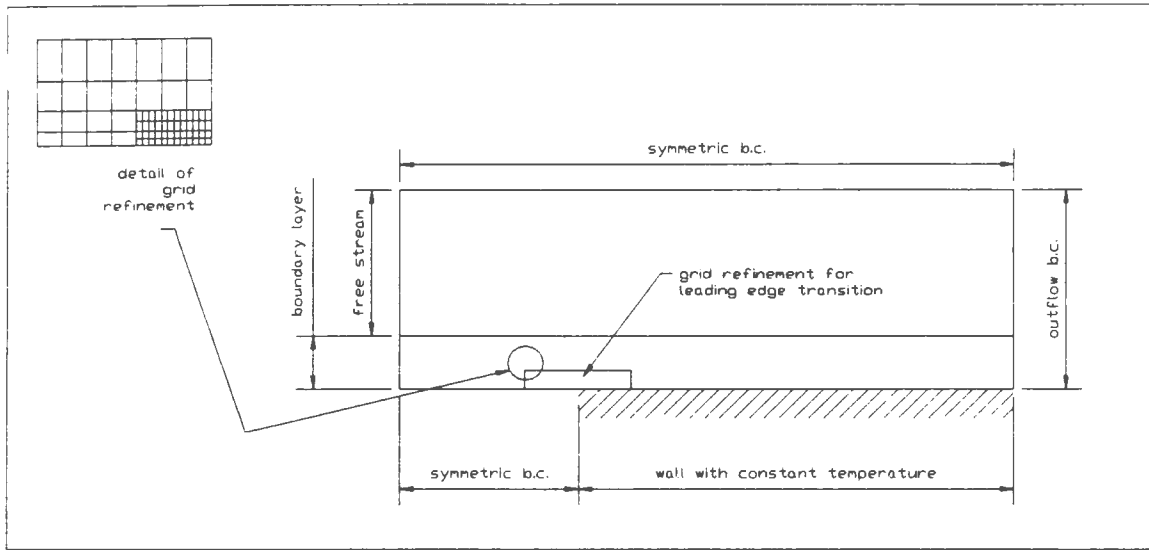


Figure 3.10: Layout for grid structure and boundary conditions for flow over a flat plate.

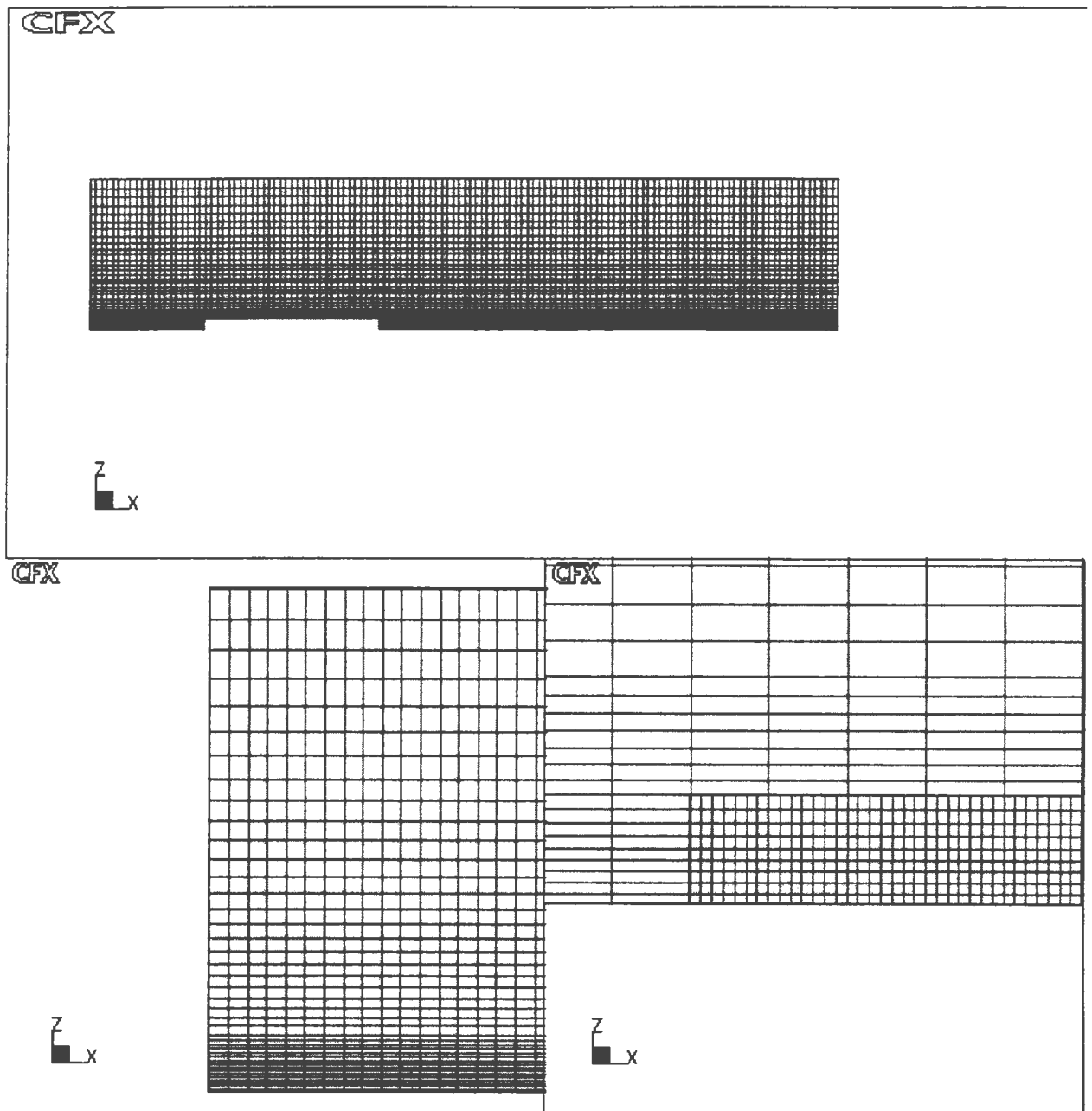
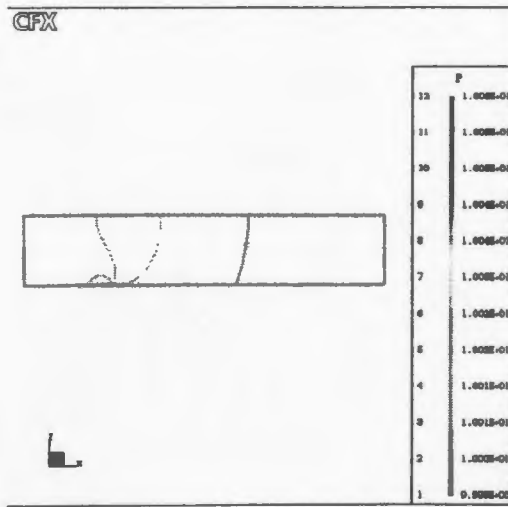
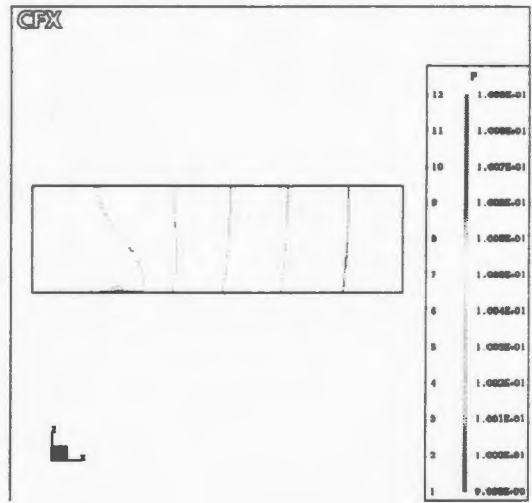


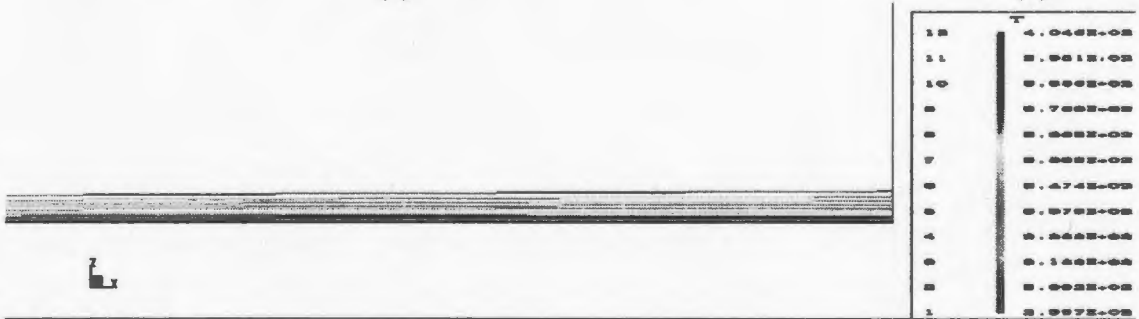
Figure 3.11: Grid structure for flow over a flat plate. Top: grid distribution, left bottom: grid distribution along vertical direction, right bottom: grid refinement around leading edge.



(a)



(b)

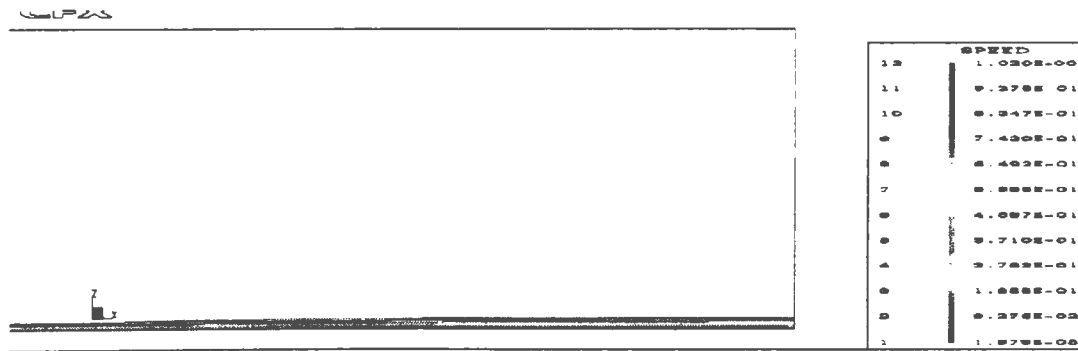


(c)



(d)

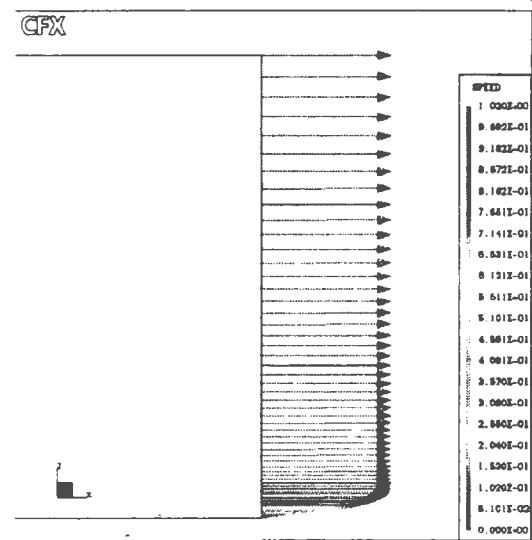
Figure 3.12: Pressure contours for (a) laminar flow, (b) turbulent flow; and temperature contour for (c) laminar and (d) turbulent flow.



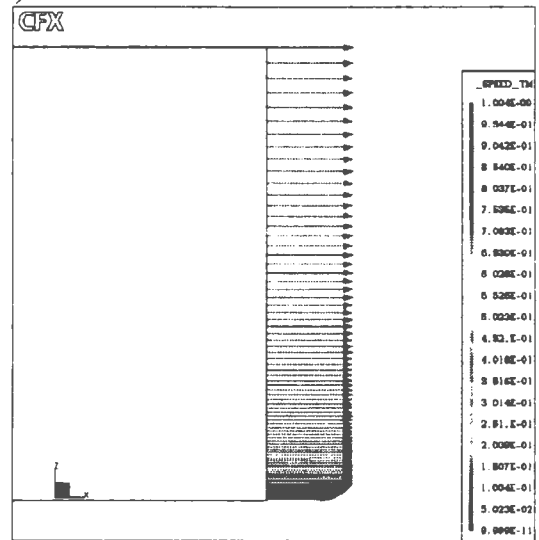
(a)



(b)



(c)



(d)

Figure 3.13: Velocity contours for (a) laminar, (b) turbulent flow; and velocity vector for (c) laminar and (d) turbulent flow.

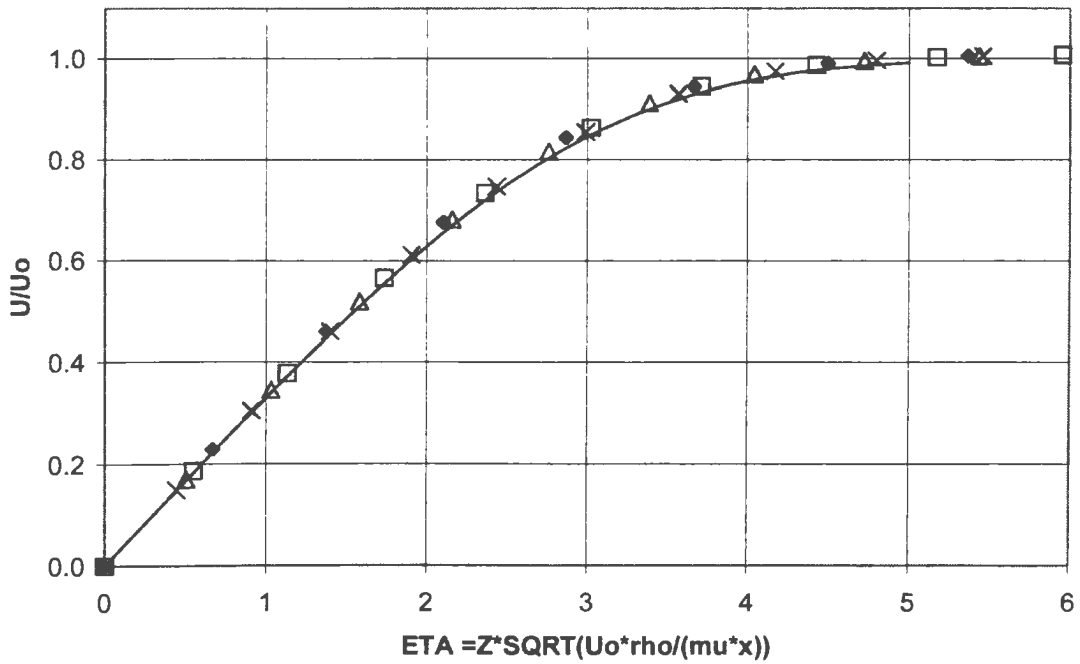


Figure 3.14: Velocity profile at several streamwise locations (laminar boundary layer). Symbols: —, Blasius; \blacklozenge , $x=0.51$ m; \square , $x=0.69$ m; \triangle , $x=0.81$ m; \times , $x=1$ m.

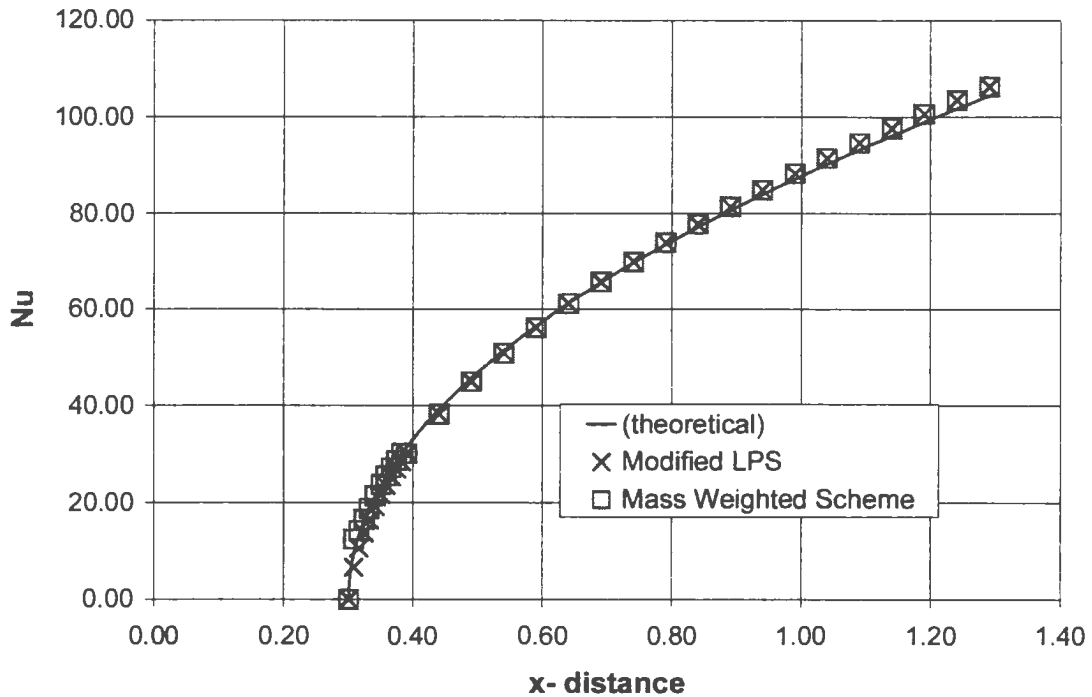


Figure 3.15: Distribution of Nusselt numbers (laminar boundary layer). Symbols: —, Theory; \times , MLPS; \square , MWS.

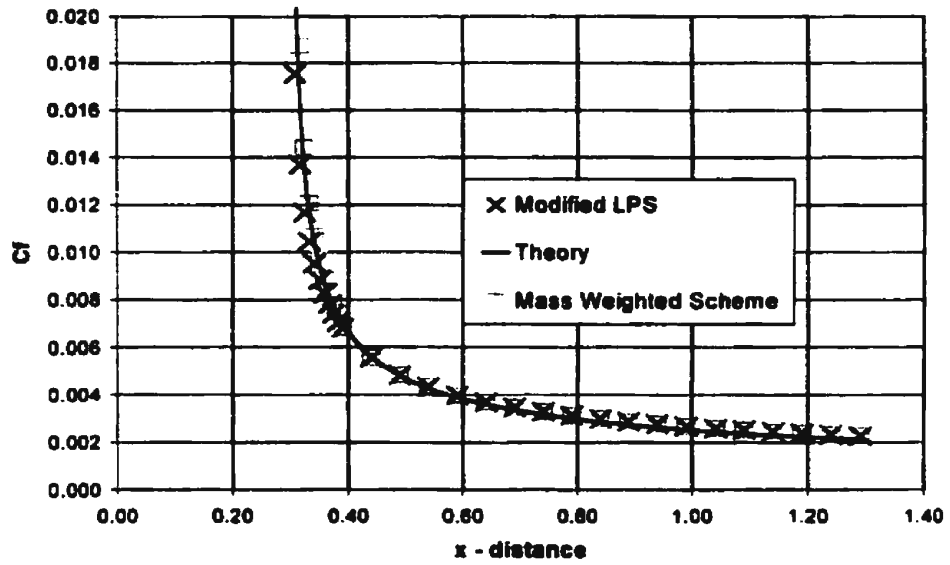


Figure 3.16: Distribution of skin Friction (laminar boundary layer). Symbols: —, Theory; x, MLPS; O, MWS.

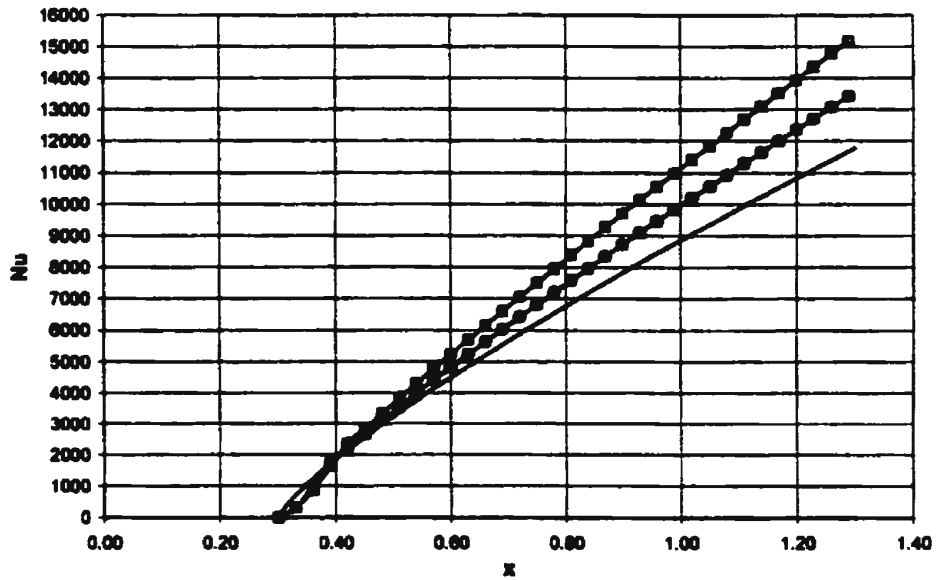


Figure 3.17: Nusselt number for coarse grid structure (turbulent boundary layer). Symbols: —, Theory; —x—, standard; —□—, Kato; —○—, RNG.

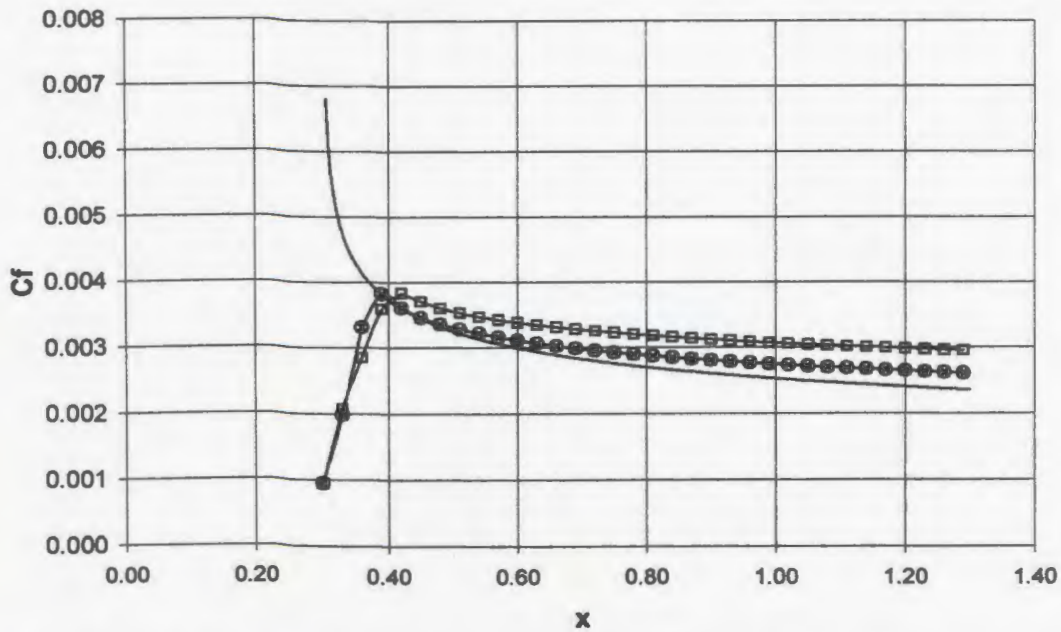


Figure 3.18: Skin friction for coarse grid structure (turbulent boundary layer).
 Symbols: —, Theory; —x—, standard; —□—, Kato; —○—, RNG.

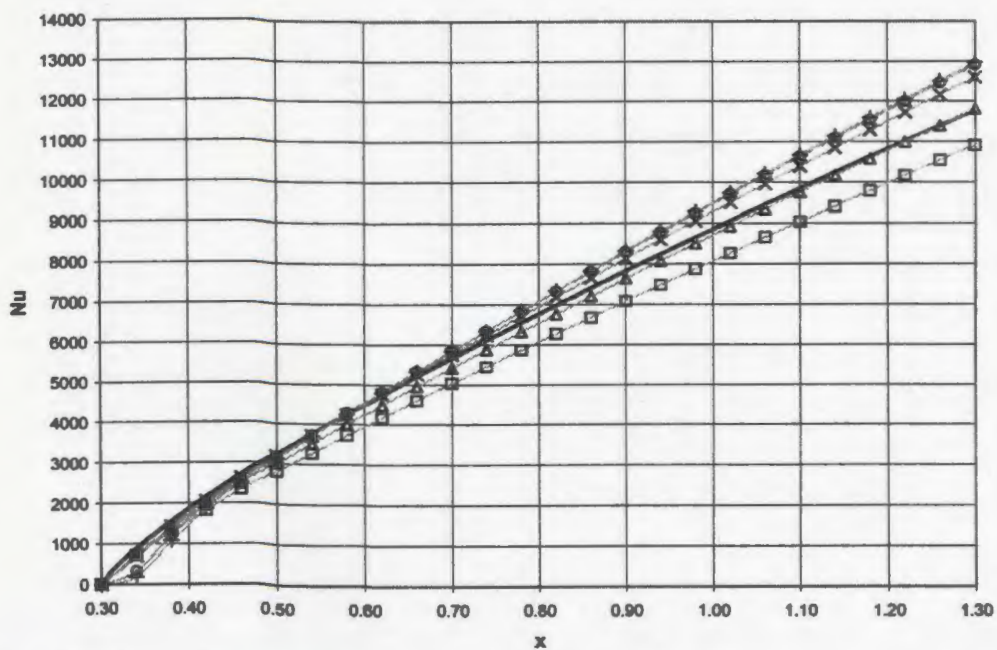


Figure 3.19: Nusselt number distribution using different distances to the first node.
 Symbols: —, Theory; □, $y=6.0 \times 10^{-5}$; Δ, $y=1.8 \times 10^{-4}$; x, $y=4.5 \times 10^{-5}$; ○, $y=6.6 \times 10^{-5}$; +, $y=8.8 \times 10^{-5}$.

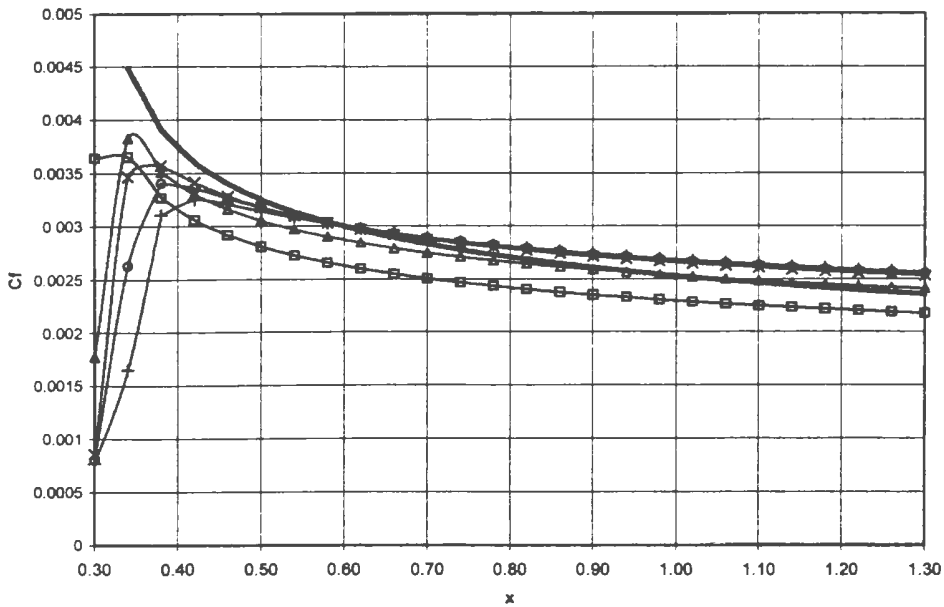


Figure 3.20: Skin friction distribution using different distances to the first node.
 Symbols: —, Theory; \square , $y=6.0 \times 10^{-5}$; Δ , $y=1.8 \times 10^{-4}$; \times , $y=4.5 \times 10^{-5}$; \circ , $y=6.6 \times 10^{-5}$; $+$, $y=8.8 \times 10^{-5}$.

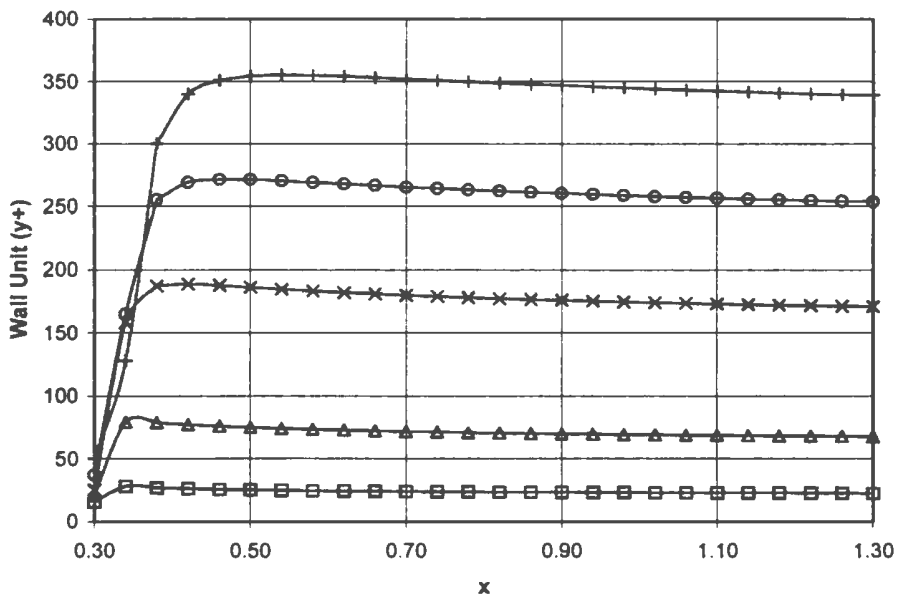


Figure 3.21: Distribution of wall unit value for different distance to the first node.
 Symbols: —, Theory; \square , $y=6.0 \times 10^{-5}$; Δ , $y=1.8 \times 10^{-4}$; \times , $y=4.5 \times 10^{-5}$; \circ , $y=6.6 \times 10^{-5}$; $+$, $y=8.8 \times 10^{-5}$.

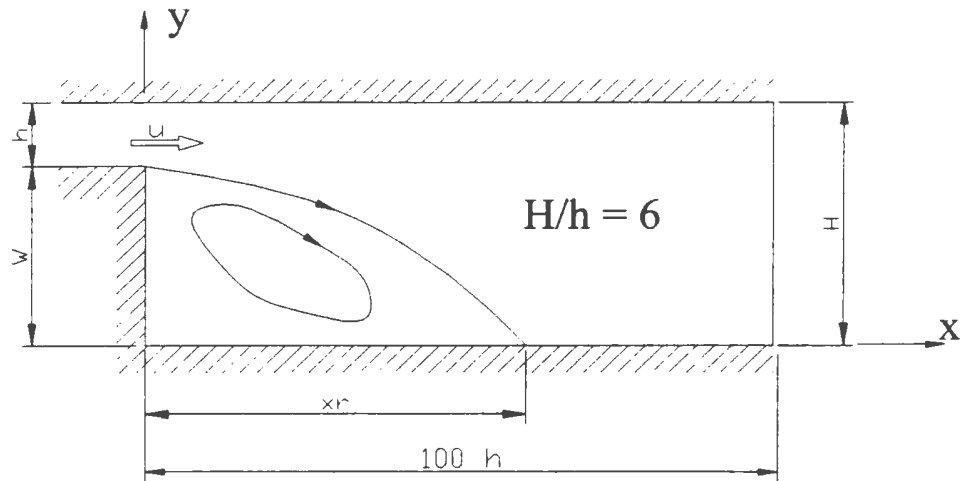


Figure 3.22: Flow domain for backward facing step.

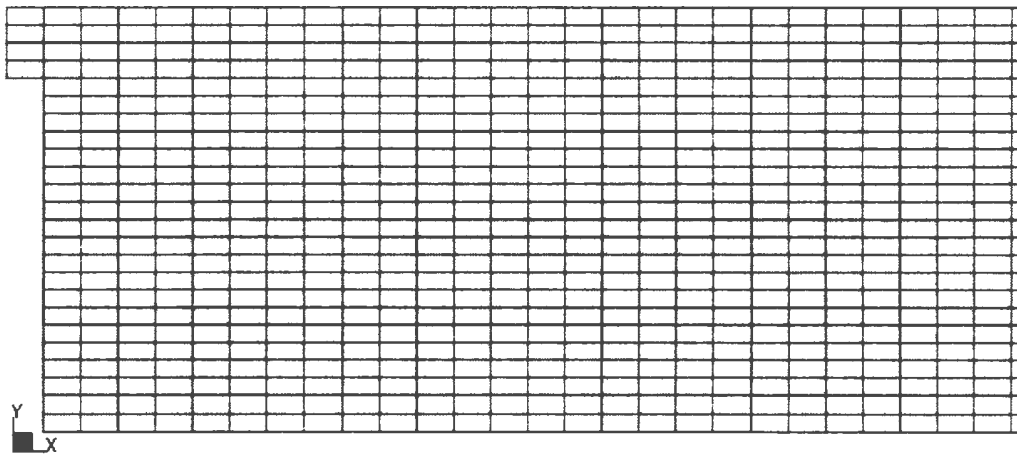


Figure 3.23: Grid structure for backward facing step.

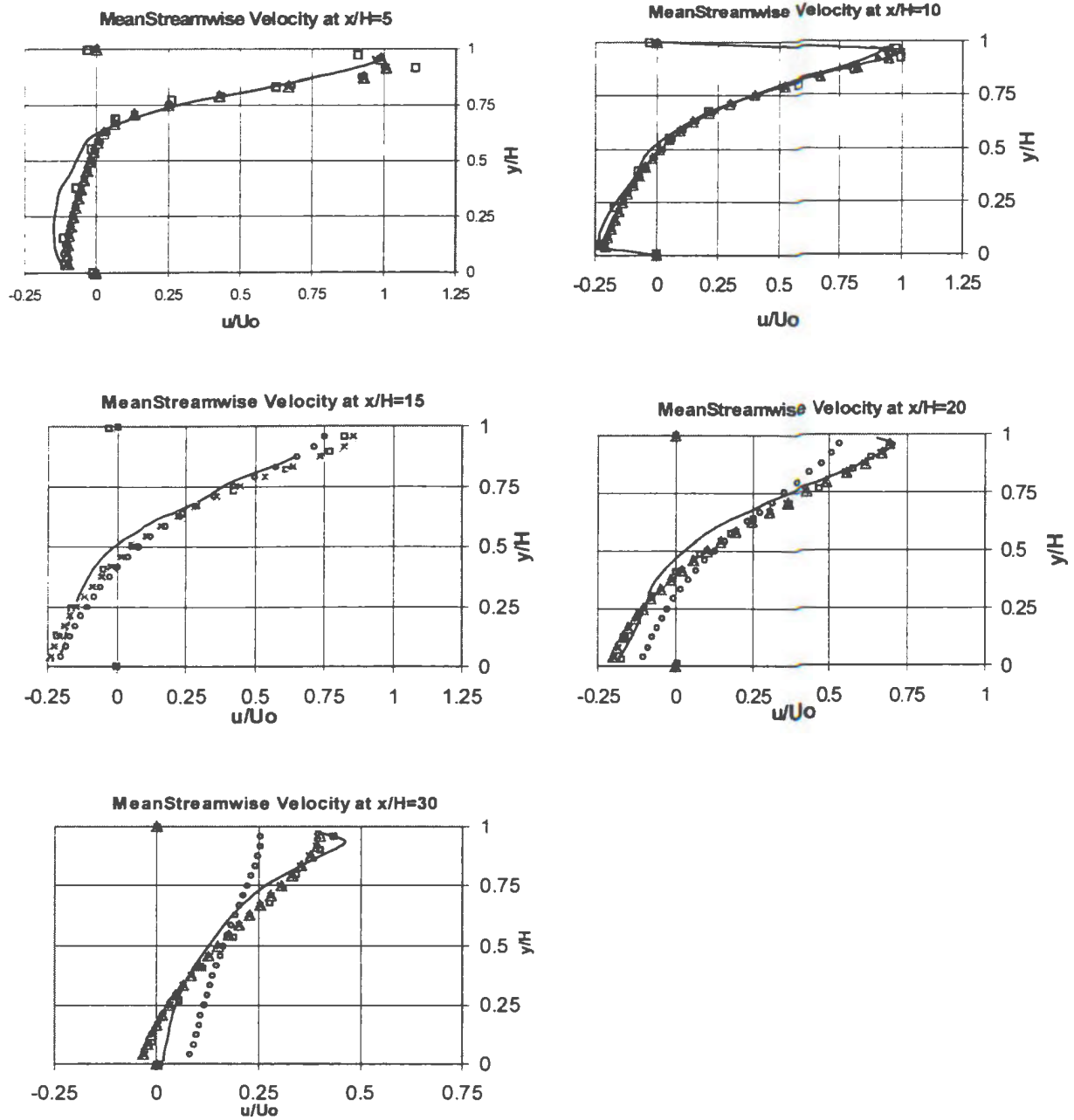


Figure 3.24: Mean streamwise velocity profile at several streamwise locations in the recirculation region. Symbols: —, Restivo (1979); □, Peng et al. (1997); Δ, standard; x, Kato; O, RNG.

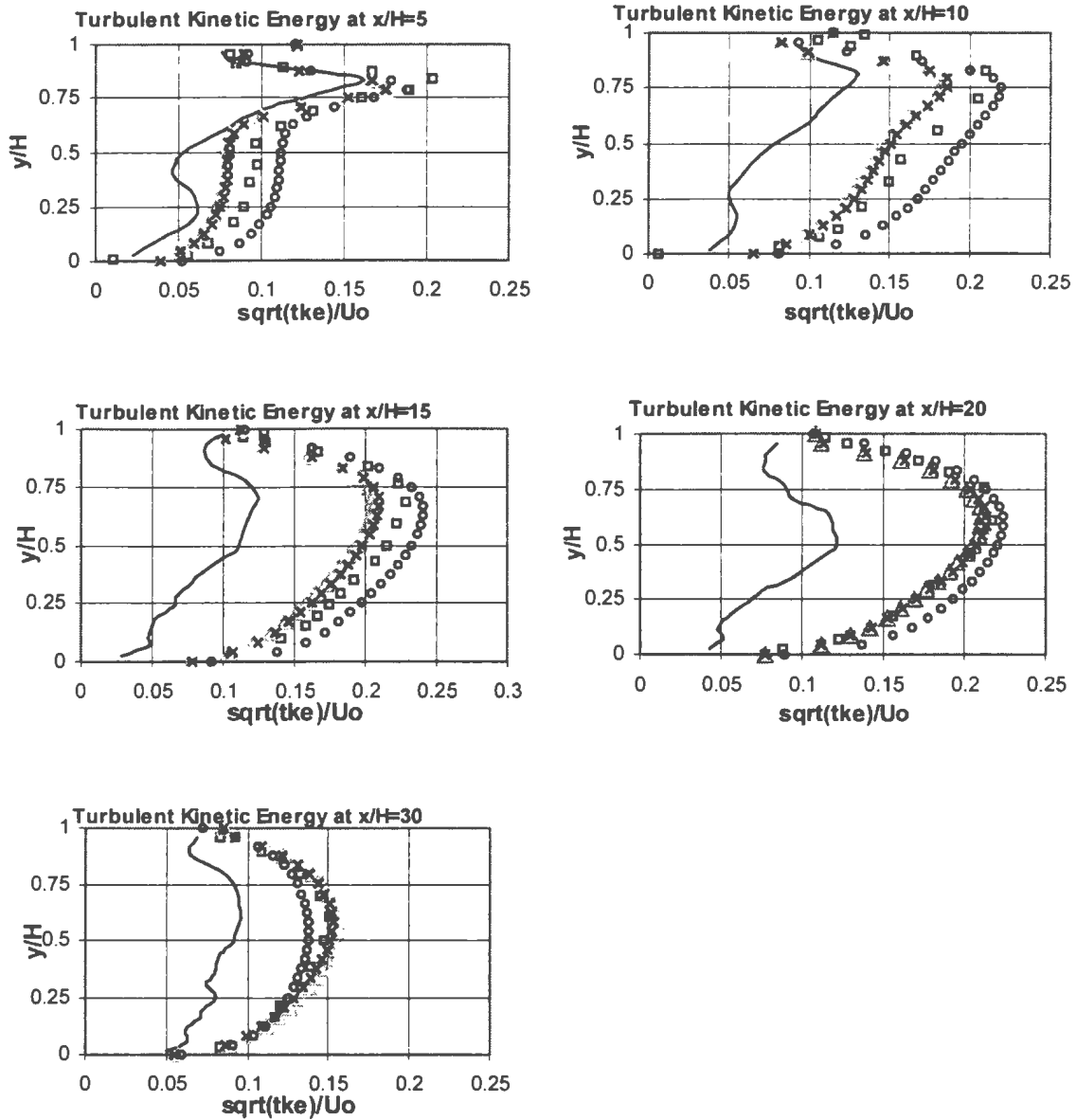


Figure 3.25: Turbulent kinetic energy profile at several streamwise locations in the recirculation region. Symbols: —, Restivo (1979); \square , Peng et al. (1997); Δ , standard; \times , Kato; \circ , RNG.

4. Stagnation Region Heat Transfer

This chapter consists of the stagnation region heat transfer simulations for laminar and turbulent freestreams. Simulations with a laminar freestream were performed to evaluate the influence of grid structure, discretization scheme and Reynolds number in the stagnation region heat transfer calculations. The best options using the laminar simulations are then implemented in the turbulent freestream simulations by using different Reynolds numbers, turbulent intensities and integral length scales.

4.1. Laminar freestream

Heat transfer rate in the stagnation region is usually expressed in terms of Frossling number, defined as local Nusselt number divided by square root of the Reynolds number ($Fr \equiv Nu / \sqrt{Re_D}$). For a laminar freestream, Frossling (1940) developed a semi-theoretical solution for the stagnation region heat transfer as a function of distance along the surface. For a cylindrical leading edge, the Frossling solution is given as (Frossling, 1940):

$$Fr\left(\frac{s}{D}\right) = 0.9411 - 0.1999\left(\frac{s}{D}\right)^2 + 0.076\left(\frac{s}{D}\right)^4 \quad (4.1)$$

Equation 4.1 is valid from the stagnation point up to the location where flow separation occurs.

Separation of the flow occurs in the presence of a favourable pressure gradient, when fluid experiences acceleration along a curved path. Since separation changes the flow direction away from the wall, the convection heat transfer decreases beyond the separation point. On the contrary, reattachment increases the heat transfer sharply. The location of the separation point depends on Reynolds number, surface geometry and flow conditions. Figure 4.1 shows that separation and reattachment flow change local heat transfer for a laminar boundary layer over a cylindrical leading edge. Separation occurs at the angular location $\theta \approx 90^\circ$ for $Re = 1.3 \times 10^4$. When the Reynolds number increases, the separation point moves forward to $\theta \approx 76^\circ$ at $Re = 10^5$. Further increase in Reynolds number causes the separation point to move backward. At Reynolds number of 1.25×10^5 separation occurs at $\theta \approx 81^\circ$ (Zdravkovich, 1997). The boundary layer becomes turbulent and the separation point moves backward to $\theta \approx 120^\circ$, when the Reynolds number increases to 3×10^5 . Figure 4.2 shows the approximate location of the separation point with Reynolds number.

Rigby and Van Fossen, (1992) simulated stagnation region heat transfer using the PARC3D code, a solver for three-dimensional Navier-Stokes equations, for a laminar freestream with Reynolds numbers ranging from 10^4 to 2×10^5 . The simulation results were in very good agreement with both experimental and analytical results, where the calculated stagnation point Frossling number ranges from 0.934 to 0.942. The Frossling number distribution obtained from their calculations is used to compare the present simulation.

4.1.1. Problem definition

Since there is flow symmetry, the domain for the simulation is half the actual flow domain. The grid structure is one half of the C-type grid. The boundary conditions are shown in Figure 4.3. Uniform velocity is specified as the inlet boundary condition, while uniform static pressure at atmospheric condition is specified as the outlet boundary condition. Heat transfer with constant wall temperature is specified on the cylindrical leading edge and adiabatic on the straight wall. Grid refinement around the leading edge is intended to accommodate the changes in flow properties in the viscous sublayer region of the boundary layer. By using air at STP conditions, simulations were performed at a Reynolds number of 13,000. The results using four discretization schemes (Upwind, MWS, MWLS and LPS) are presented in this chapter.

A C-type grid structure is used for the simulations. The x-co-ordinate is measured along the surface of the wall, starting from the outlet boundary condition and ending at the stagnation point. Y-direction is perpendicular to the wall, starting from the freestream and ending at the wall. The z-direction is perpendicular to the plane (Figure 4.3). For the preliminary simulations, a grid structure with 90x40x3 nodes is used. A non-uniform grid distribution in the freestream and in the near wall region is used.

Simulations were performed with the first grid structure (Figure 4.4a) to select an appropriate discretization scheme. Then simulations were performed on the three types of grid structure shown in Figure 4.4, to determine the most appropriate grid structure. Each

grid structure has different characteristics that affect the accuracy of the heat transfer computations. The first grid structure has a rectangular shape in the freestream. Consequently, elements on the leading edge are non-orthogonal, especially at the location 45° from the stagnation point. The second grid provides orthogonality for all elements. The third is a modification of the second grid by shortening the straight wall region to reduce elemental aspect ratio and making the grid denser near the stagnation point. Orthogonal elements and proper elemental aspect ratio eliminate the effect of false diffusion, and estimates separation more accurately. Since the flow is critical to the presence of false diffusion and separation, different grid structures are required to obtain accurate simulations. Control parameters for the laminar freestream simulations are shown in Table 4.1.

Table 4.1: Control parameters for laminar freestream simulations

Parameter name	value
Number of time iterations	900
Sutherland law	Yes
Residual error target	1.0e-6
Multigrid	Yes

4.1.2. Flow simulation

Frossling number is calculated as:

$$Fr(\theta) = \frac{Nu_D(\theta)}{\sqrt{Re}} \quad (4.2)$$

The Nusseit number for constant wall temperature is calculated as:

$$Nu_D(\theta) = \frac{h(\theta)D}{k} = \frac{q''}{(T_w - T_\infty)} \frac{D}{k} \quad (4.3)$$

Wall (T_w) and freestream (T_∞) temperatures are obtained from the boundary conditions, and thermal conductivity (k) is calculated from the Sutherland law (CFX-TASCflow, 1999c):

$$k(T) = \frac{0.0025 T^{1.5}}{(T + 194.4)} \quad (4.4)$$

By using the Sutherland law, the influence of temperature change on the thermal conductivity is incorporated in the simulations.

Figure 4.5 shows the performance of the discretization schemes using the first grid structure, shown in Figure 4.4a. The upwind scheme has the poorest performance among the different discretization schemes. Modified Linear Profile Scheme (MLPS) has a better performance in estimating Frossling number than the Upwind scheme. The best

performance is obtained using the Mass Weighted Scheme (MWS) and Linear Profile Scheme (LPS). The latter two schemes are able to better estimate Frossling number and also predict separation and reattachment, because both schemes have better performance in handling false diffusion. Compared to the results of Rigby and VanFossen, MWS and LPS results are higher by about 14%. The error is mainly caused by the use of a coarse grid for these simulations. Figure 4.7 shows the velocity contours for the four discretization schemes. Figure 4.7 b and d show a larger separation compared to Figure 4.7 a and c. The large separation causes MWS and LPS schemes to have smaller Frossling numbers compared to Upwind and MLPS schemes at the location $\theta \approx 80^\circ$. The difference in Frossling number distribution at locations around the stagnation point performed by Upwind and MLPS cannot be illustrated by the velocity contours, because the velocity magnitude at that location is very small. This is shown by the color of the velocity contour. The next simulations are performed by employing a local grid refinement near the wall for all grid structure. The LPS is chosen since it provides a better estimation of the Frossling number distribution.

Local refinement of the grid is performed by dividing the elements near the wall to obtain additional elements that are nine times smaller than the original. A large number of element divisions can create oscillation of the simulation results. To reduce the oscillation, the grid refinement is performed by using a cascaded grid refinement. For example, to obtain elements that are nine times smaller, the element is divided into 3x3x1

smaller elements. The next refinement divides the new element into 3x3x1 smaller elements (Figure 4.6).

Figure 4.8 shows the distribution of Frossling number in the stagnation region using the different grid structures. The heat transfer results using the first grid structure are higher than the Frossling solution for locations $\theta < 45^\circ$, and lower beyond this location. This is caused by non-orthogonality of the elements at that location. The first grid also overpredicts the separation point. Figure 4.9, 4.10 and 4.11 show velocity and pressure contours for the first, second and third grids, respectively. The recirculation at the straight wall indicates the presence of flow separation. The first grid overestimates heat transfer at location $\theta \approx 40^\circ$, and underestimates at $\theta \approx 70^\circ$ (Figure 4.8). The distortion is caused by elements at location $40^\circ < \theta < 70^\circ$ that are not orthogonal. Orthogonal elements are important to maintain the conservation of flow properties that enter and leave the element. The third grid gives a better prediction of heat transfer, but predicts separation larger compared to the second grid. This can be seen from the speed and pressure contours of the second and third grid (Figures 4.10 and 4.11). As a result, the third grid has a sharp decrease of Frossling number at the location between $\theta = 80^\circ$ to $\theta = 90^\circ$ (Figure 4.8). The results using the second grid structure (Figure 4.8) are closest to the calculations of Rigby and Van Fossen (1992). Similar with experiment at $Re=13000$ (Zdravkovich, 1997), the second grid also shows separation at $\theta=90^\circ$ (Figure 4.11).

The final simulations for laminar freestream were performed using the LPS discretization scheme and the second grid structure for Reynolds numbers of 6.5×10^3 , 1.3×10^4 , 1.3×10^5 and 6.5×10^5 . The simulation is intended to validate the capability of the CFD code in estimating Frossling solution under a laminar freestream. The simulation results for this case are shown in Figure 4.12. The Frossling number distribution at Reynolds number 6.5×10^3 , 1.3×10^4 and 1.3×10^5 are in close agreement with the calculations of Rigby and VanFossen up to the location of $\theta=70^\circ$. Frossling numbers at the stagnation point ($\theta=0^\circ$) are 0.95, 0.967 and 1.03, respectively. The smaller value of Frossling number beyond $\theta=70^\circ$ is caused by the uncertainty of the heat transfer at that location due to the presence of flow separation. Experimental and simulation results of VanFossen also differ from the laminar Frossling solution at the same location. At $Re = 1.3 \times 10^5$, the Frossling number decreases drastically at $\theta=80^\circ$ and increases sharply at $\theta=90^\circ$, since separation occurs at $\theta=80^\circ$, and reattachment occurs at $\theta=90^\circ$.

4.2. Turbulent freestream

For a turbulent freestream, heat transfer in the stagnation region depends on the interaction between the freestream and the boundary layer on the surface. The boundary layer consists of both laminar and turbulent regions. In flow over a cylinder, the laminar region can exist to a significant distance (Achenbach, 1975). For $Re=10^5$, the boundary layer is laminar in the region $0^\circ < \theta < 90^\circ$, while at $Re=4 \times 10^6$, the laminar region is $0^\circ < \theta < 40^\circ$. The increase of Reynolds number moves the location of transition upstream. Since the turbulent region produces higher heat transfer rate, the increase of Reynolds

number will increase the overall heat transfer. The interaction between the freestream and the boundary layer depends on Reynolds number and turbulence characteristics, especially the turbulence intensity and integral length scale.

The increase of Reynolds number under a constant turbulence intensity causes a smaller boundary layer thickness, which in turn increases the temperature gradient and heat transfer rate. The increase of Reynolds number also promotes earlier separation and reattachment flow. At $Tu=0.5\%$ and $Re=10^5$, the flow separates at $\theta=80^\circ$, and reattaches at $\theta=90^\circ$. When Reynolds number increases from 10^5 to 1.9×10^6 , the boundary layer transition moves upstream to $\theta \approx 70^\circ$ and causes a significant increase in overall heat transfer (Achenbach, 1975).

Turbulence intensity is defined as the ratio of the rms of the fluctuating velocity components to the mean streamwise velocity.

$$Tu = \frac{\left\{ \frac{1}{3} [u'^2 + v'^2 + w'^2] \right\}^{1/2}}{U} \quad (4.5)$$

For isotropic turbulence, equation (4.5) becomes:

$$Tu = \frac{u'}{U} \quad (4.6)$$

where u' is the RMS value of the fluctuating streamwise velocity component. Freestream turbulence intensity has a significant influence on stagnation region heat transfer. At $Re=2.2 \times 10^5$, the stagnation Frossling number increases from 0.945 to 1.25 as the turbulence intensity increases from 0 to 0.8% (Kestin, 1966). Zang and Han (1994)

reported an increase of heat transfer on the gas turbine surface as high as 250% due to turbulence intensity increase from 0.7% to 17%.

Integral length scale describes the averaged eddy size associated with turbulence. The calculation of integral length scale is based on the correlation of the longitudinal fluctuating velocity components at two locations spaced apart in the streamwise direction. By integrating the correlation over a distance from 0 to ∞ , the integral length scale is obtained.

$$R(y) = \frac{\overline{u_1 \cdot u_2}}{\left[\overline{u_1^2} \right]^{1/2} \left[\overline{u_2^2} \right]^{1/2}} \quad (4.7)$$

$$\lambda = \int_0^{\infty} R(y) dy$$

where:

$\overline{u_1}, \overline{u_2}$ = time-averaged fluctuating velocity component at two locations

$R(y)$ = correlation coefficient

λ = integral length scale

Yardi and Sukhatme (1978) correlated stagnation region heat transfer with turbulence intensity and an integral length scale parameter, $(\lambda/D)\sqrt{Re_D}$. They determined an increase of integral length scale decreases heat transfer rate. They also reported that the optimum integral length scale is between 5 to 15 times the boundary layer thickness. Van Fossen et al. (1995) investigated stagnation region heat transfer by varying the ratio of integral length scale to leading-edge diameter from 0.05 to 0.3. The heat transfer

increases with decreasing length scale, but they were unable to determine an optimum integral length scale.

Several correlations have been developed for the heat transfer and freestream turbulence characteristics. Lowery and Vachon (1975) reported an increase in local heat transfer with an increase of turbulence intensity in the laminar boundary-layer region $0^\circ < \theta < 40^\circ$. By performing experiments at Reynolds number ranging from 1.09×10^5 to 3.02×10^5 and turbulence intensity $0.4\% < Tu < 14.2\%$, they proposed a correlation for Frossling number at the stagnation point as:

$$\frac{Nu}{\sqrt{Re_D}} = 1.01 + 2.624 \left[\frac{Tu \sqrt{Re_D}}{100} \right] - 3.07 \left[\frac{Tu \sqrt{Re_D}}{100} \right]^2 \quad (4.8)$$

Van Fossen et al. (1995) correlated heat transfer at the stagnation point with Reynolds number, turbulence intensity and integral length scale. They proposed the correlation:

$$Fr(0) = 0.008 \sqrt{Tu Re_D^{0.8} \left(\frac{\lambda}{D} \right)^{-0.574}} + 0.939 \quad (4.9)$$

where:

λ = integral length scale

D = leading edge diameter

Re_D = Reynolds number based on leading edge diameter

VanFossen et al. (1995) plotted their experimental data using equation (4.8) and found that their data were not correlated with parameter $Tu\sqrt{Re_D}$ (Figure 4. 14). By using equation (4.9) for plotting the experiment data of VanFossen et al and other authors (Yeh, 1993; Smith and Kuethe, 1966; Mehendale et al., 1991; and Lowery and Vachon, 1975), the correlation between heat transfer and turbulence parameters can be obtained with deviation of 4% and 10%, respectively (Figure 4. 15). Since equation (4.9) gives good agreement with many author's data, Frossling number distribution for a turbulent freestream can be estimated by using equation (4.9) and normalising Frossling number by:

$$Fr(s/R)_{turb} = \left(\frac{Fr(s/R)}{Fr(0)} \right)_{lam} Fr(0)_{turb} \quad (4. 10)$$

Unlike experiments that have provided a good estimation of stagnation region heat transfer, simulations for stagnation region heat transfer for a turbulent freestream can still be in error by a significant amount (Larsson, 1996; Larsson et al., 1995; and Rigby and VanFossen, 1992). The sources of error are mainly due to the turbulence model, the discretization scheme and grid construction. Rigby and Van Fossen (1991 and 1992) simulated freestream turbulence by varying inlet velocity and momentum by 0.4 to 2.6 percent to represent a turbulent freestream. Using the PARC3D code, they reported an increase in heat transfer by 25 percent. However, numerical results are significantly different with experiments, which showed an increase of heat transfer by 50 percent.

The simulation of stagnation region heat transfer on turbine blades using a two-equation turbulence model was performed by Larsson and Håll (1998). Larsson and Håll used both the low-Reynolds number k - ϵ models (Chien and Launder-Sharma) and k - ω models (Wilcox, standard and transition). To obtain accurate simulations, Larsson and Håll suggested the distance of the first node after the wall should be below 0.2 wall unit and used double precision (64 bit) for the calculations. A smooth grid distribution also reduces the oscillation in the heat transfer calculations. All models suffer inaccuracy in estimating heat transfer, especially in the suction side and stagnation region. The models cannot predict the laminar boundary layer region on the suction surface and overestimate turbulence kinetic energy in the stagnation region. The k - ω models give better estimation in the leading and trailing edge of the suction side, while the remaining region cannot be estimated accurately (Figures 4.16 and 4.17).

The simulations of Larsson et al. (1995) on turbine blade heat transfer that used algebraic and k - ϵ turbulence models showed errors as high as 33 percent in the vicinity of the leading edge. Large normal strain at the stagnation point causes excessive production of turbulence energy that is convected downstream and induces earlier transition of the boundary layer from laminar to turbulent in the leading edge region. Consequently, the entire boundary layer is influenced by the overestimation of heat transfer. Larsson et al. (1995) tried to eliminate the error by either turning off the production term in the turbulence energy equation or by replacing the strain rate tensor with the vorticity.

However, the modification can only reduce the error on the pressure side, and not in the stagnation region and suction side. It is believed that the Boussinesq assumption fails in flows with large normal strain such as at the stagnation point (Wilcox, 1992; Larsson et al. 1995; and Taulbee et al. 1989).

Durbin (1996) reported that excessive production of turbulent kinetic energy is caused by overestimation of the turbulent time scale ($T=k/\varepsilon$) in the k and ε equations. Durbin (1996) proposed a new definition of turbulent time scale as a function of normal mean strain rate in addition to k and ε . The modification estimates k 90% smaller than that without modification. However, the progress in estimating the heat transfer was not reported. Due to the time limitation and the accessibility of the source code, the modification as proposed by Durbin and Larsson et al. cannot be performed in the present simulations. The simulations are intended to evaluate the performance of k - ε turbulence models in estimating the stagnation region heat transfer by using appropriate discretization scheme, grid construction and turbulence model.

4.2.1. Problem definition

The simulations for a turbulent freestream are performed using the second grid structure of section 4.1, since this structure gives a better estimation for the laminar freestream case. The simulation uses similar control parameters as the laminar freestream case (Table 4.2).

Table 4.2: Control parameter for turbulent freestream simulations

Parameter name	Value
Discretization scheme	LPS
Number of time iteration	900
Sutherland law	True
Residual error target	1.0e-6
Treatment for flow near wall region	Two-layer turbulence model
Multigrid	True

The two-layer turbulence model is selected because the flow near the curved wall is not in an equilibrium condition between turbulence production and turbulence dissipation. In the equilibrium condition, turbulence produced by shear strain at the wall will be dissipated as it diffuses into the freestream. Consequently, the turbulent kinetic energy contour has the highest value at the wall. In the stagnation region, the highest value of turbulent kinetic energy is not at the wall, but several nodes away from the wall (Figure 4.18). It can be concluded that the flow is not in equilibrium condition, where turbulence production is higher than turbulence dissipation.

The preliminary simulations for a turbulent freestream compare the performance of different turbulence models (Standard, Kato and RNG). Frossling number distribution obtained from all turbulence models are compared with the correlation of Van Fossen et al. (1995) as shown in equation (4.7). The turbulence model that gives the best estimation

is selected for the simulations that are performed under different combination of Reynolds number, turbulence intensity (Tu), and integral length scale, as shown in Table 4.3.

Table 4.3: Reynolds number, turbulence intensity and integral length scale (λ/D) for simulations with freestream turbulence

Reynolds number (Re)	13,000	50,000	100,000
Turbulence intensity (Tu)	1%	3%	5%
Integral length scale(λ/D)	0.4282	0.5709	0.7136

4.2.2. Flow simulation

The preliminary simulations are performed at $Re=1 \times 10^5$, $Tu=0.75\%$ and integral length scale (λ/D) = 0.98, to evaluate the different turbulence models. For the standard model, governing equations of momentum (u , v and w), continuity, k , ϵ , and energy reach convergence at 114 time iterations, while Kato and RNG models reach convergence at iterations of 142 and 146, respectively. The numerical results obtained from the simulations are compared with the experimental correlation of Van Fossen et al. (1994) Figure 4.19 shows that Kato and RNG models give better estimation with errors five and six percent respectively compared to Standard model with error of nine percent. Simulations were performed to compare Kato and RNG models in estimating Frossling

number. At $Re=5 \times 10^4$, $Tu=5\%$ and $\lambda \cdot D=0.69$, the Kato model gives a better estimation compared with the RNG model with errors six and eight percent, respectively (Figure 4.20). The errors are caused by overestimation of turbulence kinetic energy distribution on the stagnation region where the RNG model has a larger turbulence kinetic energy distribution compared with the Kato's (Figure 4. 21).

The final simulations use Linear Profile Scheme (LPS) for the discretization schemes and Kato turbulence model. Because the grid structure is highly nonuniform, where the size of the element near the wall is much smaller than in the freestream, the selection of time step is important to maintain convergence stability. The time step was specified small enough to obtain sufficient residence time defined by:

$$T = \frac{L}{V}$$

where:

L = characteristic length of flow domain

V = freestream velocity

The characteristic length depends on the length of the flow domain and the size of the smallest element. Since the final simulations were performed on the same grid structure, the residence time would only depend on the freestream velocity. The simulations under different Reynolds numbers have different time steps that were specified by trial and error. The optimum time step would give a stable convergence and require smaller number of time iterations to the reach convergence criteria. The number of time iterations

varies from 117 to 800 and depends on Re , Tu and λ . There is no correlation between the variation of the number of time iteration with the variation of Re , Tu and λ .

Figures 4.23, 4.24 and 4.25 show the Frossling number distribution for constant Reynolds numbers of 10^5 , 5×10^4 and 1.3×10^4 , respectively. The simulation results deviate from the empirical solution by as much as 10% for the Frossling number with changes of Tu . The simulations also do not show a maximum Frossling number at the stagnation point due to the presence of large normal strain rates at that point (Wilcox, 1992; Larsson et al. 1995; and Taulbee et al. 1989). Since two-equation turbulence models calculate eddy viscosity according to the Boussinesq assumption, which correlates the eddy viscosity with shear strain rate, the increase of heat transfer caused by normal strain rates cannot be captured. The detailed discussion on the estimation of stagnation Frossling number is presented later.

The final simulations consist of three cases where each case is performed to evaluate the effect of different combinations of Tu and λ/D in estimating stagnation region heat transfer. The simulations at constant $Re=10^5$ and different Tu (1%, 3% and 5%) and λ/D (0.4282, 0.5709 and 0.7136) are shown in Figure 4.26. The largest deviation for stagnation point Frossling number is for the simulations at $Tu=1\%$, and is 7% larger than VanFossen's estimation. The smallest error is found for the simulations at $Tu=3\%$ with a 0.72 percent error. The Frossling number distribution beyond $\theta=50^\circ$ is

much larger than the experimental value, since the simulations do not contain any flow separation. Velocity contours for the first simulations (Figure 4. 22 a) do not show any flow separation.

The results of the simulations at constant $Re = 5 \times 10^4$ and the same combinations of Tu and λ/D , are shown in Figure 4.24. The simulations at $Tu=1\%$ have the largest error of 10%, while the smallest error, 0.71%, occurs at $Tu=5\%$. Similar to the first case, the second case also has a Frossling number higher than the experiment at locations beyond $\theta=55^\circ$. The tendency of overestimating turbulence kinetic energy causes the computations to be less sensitive to the change of Tu and λ/D compared to the experimental results. It is difficult to explain the insensitivity, but the simulation results from all cases show the same tendency.

Figure 4.25 shows the result of the simulations at constant $Re=1.3 \times 10^4$. The simulation has the largest error in stagnation point Frossling number (4.4%) at $Tu=5\%$, and the smallest error (1 percent) at $Tu=1\%$. Unlike the previous cases, the third case has a sharp decrease of Frossling number distribution beyond $\theta=60^\circ$. This is likely caused by the presence of flow separation at that location. The small separation can be identified by the velocity contour located at $\theta=90^\circ$ (Figure 4. 22 b).

To evaluate the performance of the simulations, the stagnation point Frossling numbers are plotted against the correlation parameter $Tu Re_D^{0.8} (\lambda D)^{-0.574}$ as proposed by VanFossen et al. (1995). Figure 4.26 shows that the calculated stagnation point Frossling numbers lie 10 percent above and 5 percent below the empirical correlation. Stagnation Frossling numbers at $Re=10^5$ and 1.3×10^4 are not distributed along the curve of equation 4.6, but its averaged value agrees with the correlation. Overestimation of k near the wall, as described by Durbin (1996), has reduced the accuracy of estimating heat transfer. The estimations of stagnation Frossling numbers and the errors compared to equation 4.6 are shown in Table 4.4. Although there is a significant error ranging from 0.22 to 10.11 % in the heat transfer estimation, the simulations show an increase in stagnation Frossling number with an increase of Reynolds number and turbulence intensity. However, a decrease of integral length scale does not always increase stagnation point Frossling number. It is also shown that the increase of integral length scale under constant Tu is not followed by a decrease of stagnation Frossling number.

Table 4.4: Stagnation Frossling numbers

	Re = 100,000			Re = 50,000			Re = 13,000		
	δ/D	Fr(0)	% error	δ/D	Fr(0)	% error	δ/D	Fr(0)	% error
Tu = 1%	0.428	1.091	7.62	0.428	1.0889	7.15	0.428	0.996	1.25
	0.571	1.089	8.45	0.571	1.089	7.80	0.571	0.996	1.62
	0.714	1.099	9.34	0.714	1.0895	8.32	0.714	0.996	1.89
Tu = 3%	0.428	1.102	0.63	0.087	1.0923	1.72	0.087	0.996	-2.21
	0.571	1.112	2.31	0.116	1.0929	2.79	0.116	0.996	-1.57
	0.714	1.112	3.25	0.145	1.0887	3.13	0.145	0.996	-1.18
Tu = 5%	0.428	1.114	-3.19	0.087	1.1041	-0.78	0.087	0.999	-4.03
	0.571	1.114	-1.65	0.116	1.1086	0.86	0.116	0.998	-3.34
	0.714	1.116	-0.39	0.145	1.1086	1.77	0.145	1	-2.65

It can be concluded that the simulations are less sensitive to the change of Tu and are insensitive to the change of integral length scale. The inaccuracy of simulations may be caused by the inadequate distance of the first node near the wall, the single precision of variable storage and the pitfall of $k-\epsilon$ turbulence model in simulating flow over a curved body. The following sections discuss the sources of inaccuracy.

The implementation of a two-layer turbulence model requires that the distance of the first node after the wall should be in the viscous sublayer (≈ 2 wall units). Due to the limitation of computer memory and maintaining element aspect ratio, the first node was located at a distance of 13 wall units. This condition causes inaccuracies in the solution using two-layer turbulence models. Increasing computer memory can increase the number of elements near the wall and reduce the distance from the wall to the first node into 2 wall units without changing element aspect ratio. This condition will assure a

consistent application of two-layer turbulence models and increase the accuracy of the simulation.

The inability of the CFD-code to provide double precision calculation also causes inaccuracy of the iteration process. By storing variables in single precision, large truncation errors may occur during the iteration process.

As mentioned earlier, the pitfall of the k - ϵ turbulence model is caused by the failure of the Boussinesq assumption in flows over a curved body. A more accurate simulation can be performed by modifying the Reynolds-stress tensor (Taulbee et al. 1989; Wilcox, 1993), modifying the time scale for k and ϵ equations (Durbin, 1996), and using Second-Order Closure Models rather than k - ϵ turbulence models (Wilcox, 1993). The Reynolds-stress tensor can be expressed in terms of normal strain rate and vorticity tensor, in addition to shear strain tensor. By including normal strain rate and vorticity tensor, any sudden change of strain rate will not reduce the accuracy. Modifying the time scale is intended to decrease k into more realistic conditions. Since k relates to the governing equation of energy, the modification should increase the accuracy of the heat transfer calculations. Among the mentioned modifications, the use of Second-Order Closure models is the best choice, since the model introduces an additional governing equation for the Reynolds-stress tensor. The new governing equation will calculate the time scale properly and take account of sudden changes in the strain rate. Since the CFD-code does not provide Second-Order Closure models, the simulation under this model

cannot be performed. The modification as proposed by Durbin (1996) requires the access to the software source code. Due to the time limitation, this improvement was also not performed.

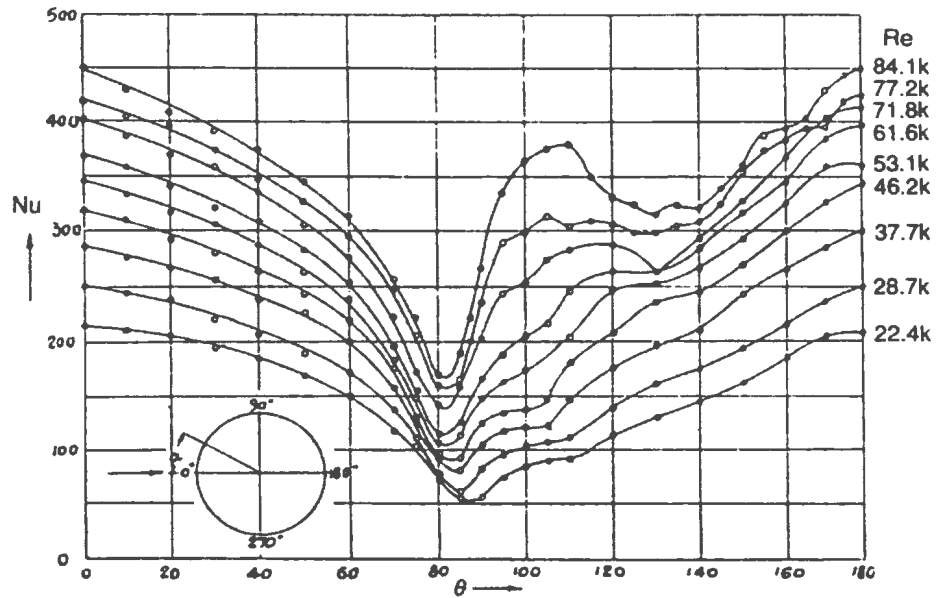


Figure 4.1: The influence of separation and reattachment flow on the local heat transfer rate (reproduced from Zdravkovich, 1997).

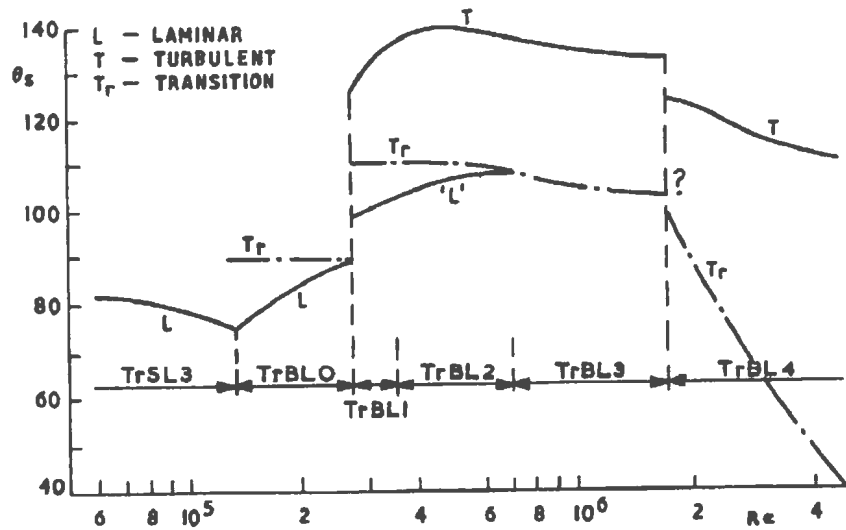


Figure 4.2: The location of separation point for flow over cylinder (rep. from Zdravkovich, 1997).

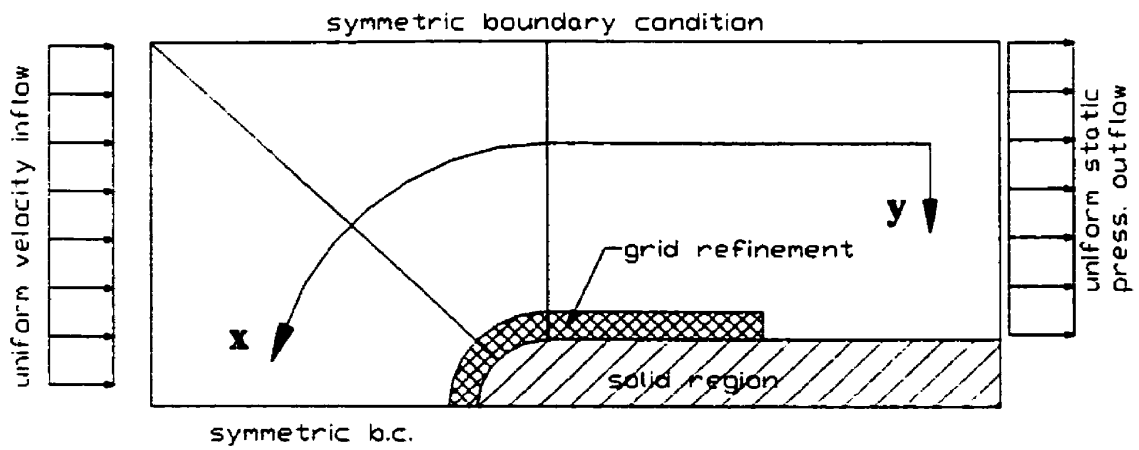
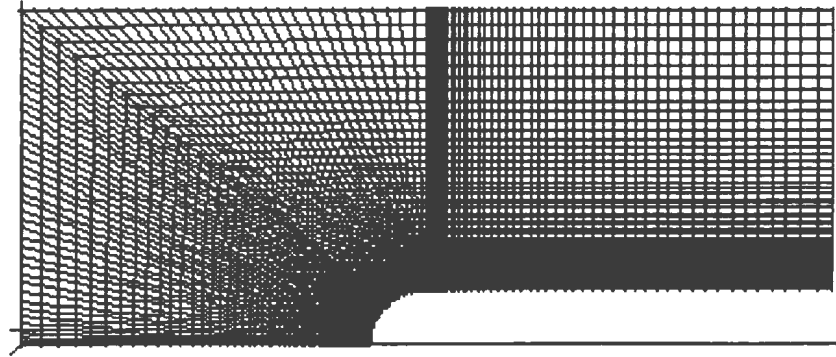
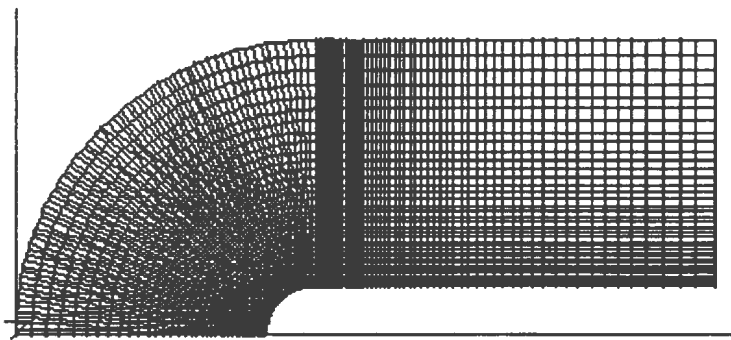


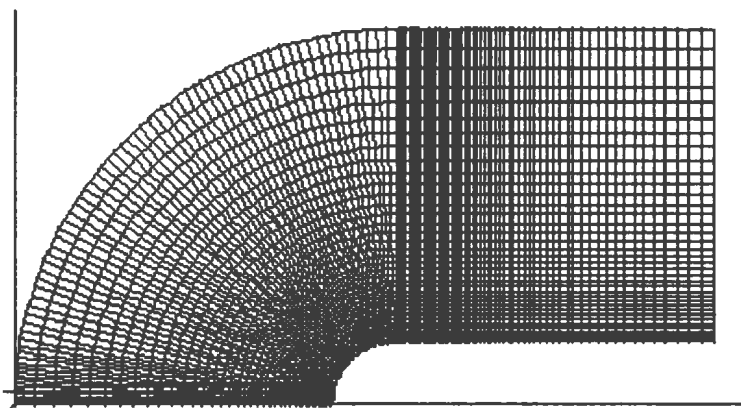
Figure 4.3: Boundary conditions for flow over the stagnation region.



(a)



(b)



(c)

Figure 4.4: Grid structures for laminar flow over the stagnation region.

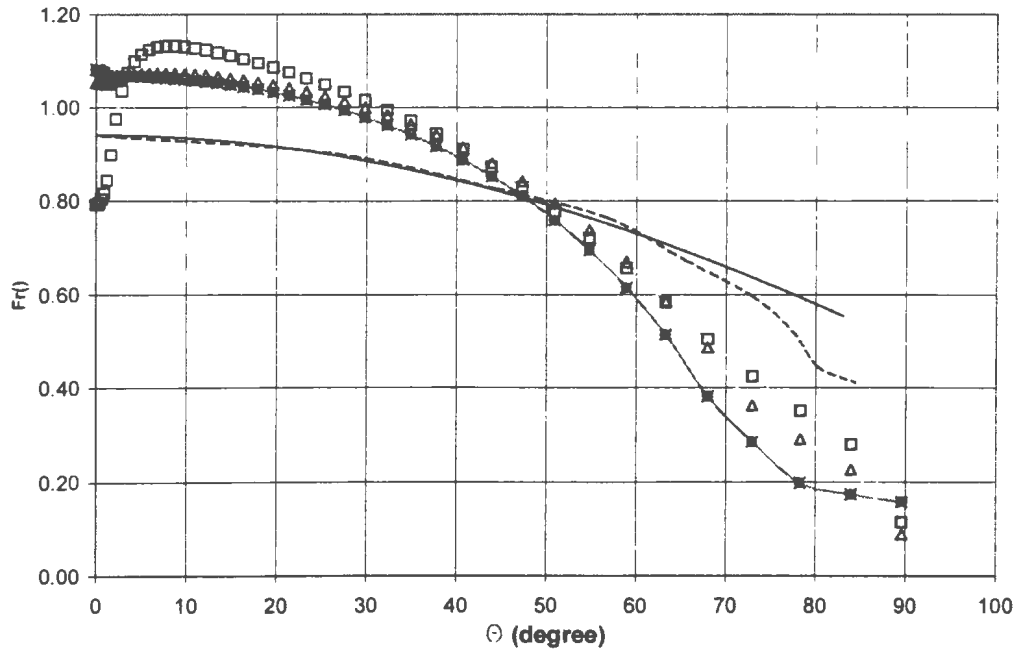


Figure 4.5: The performance of discretization scheme in estimating Frossling number using the first grid structure. Symbols: —□—, Upwind; —○—, MWS; —△—, MLPS; —x—, LPS; —, Frossling (1940); - - -, Rigby and Van Fossen (1992).

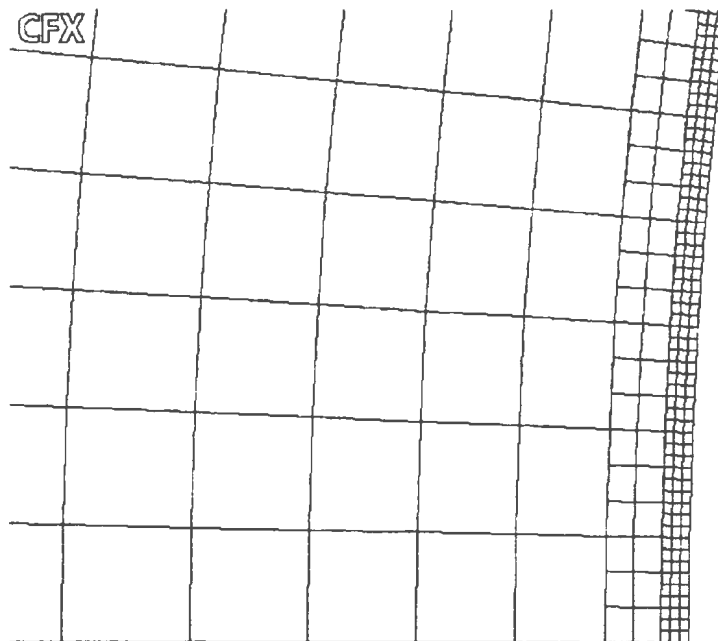


Figure 4.6: Local grid refinement near the wall on the stagnation point.

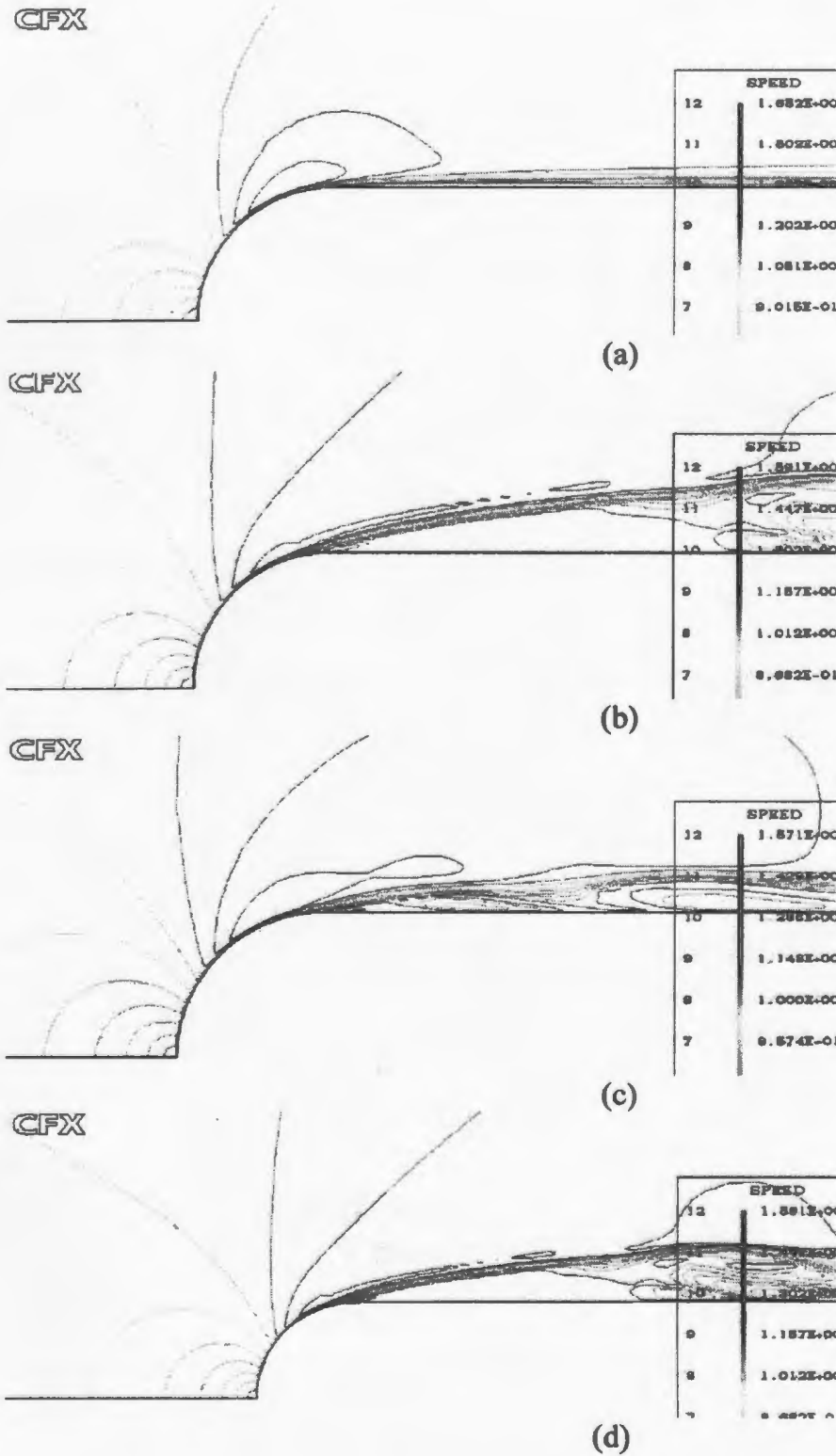


Figure 4.7 Velocity contours for different discretization schemes (a) Upwind, (b) MWS, (c) MLPS and (d) LPS.

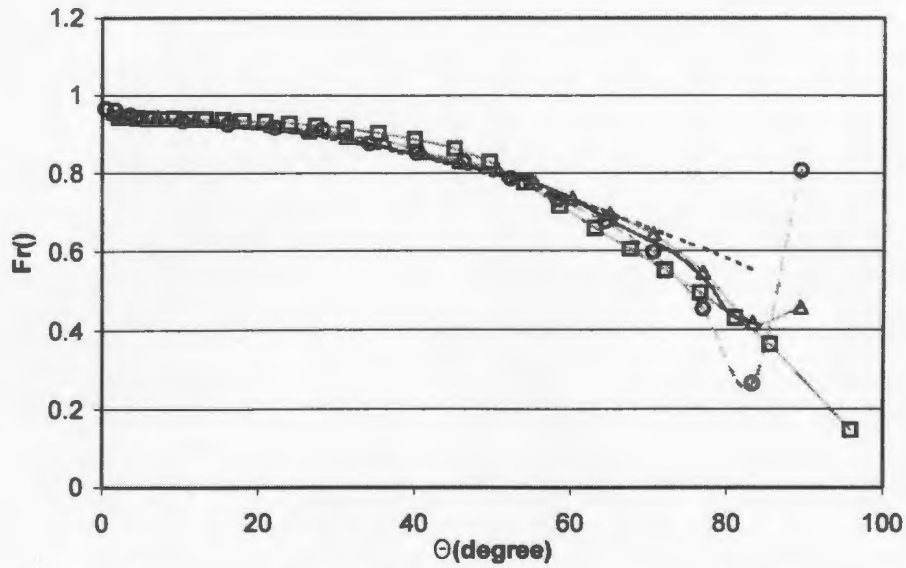


Figure 4.8: Estimation of Frossling number using different grid structure. Symbols: \square , first grid; \triangle , second grid; \circ , third grid; —, Rigby and VanFossen (1992); - - - -, Frossling (1940).

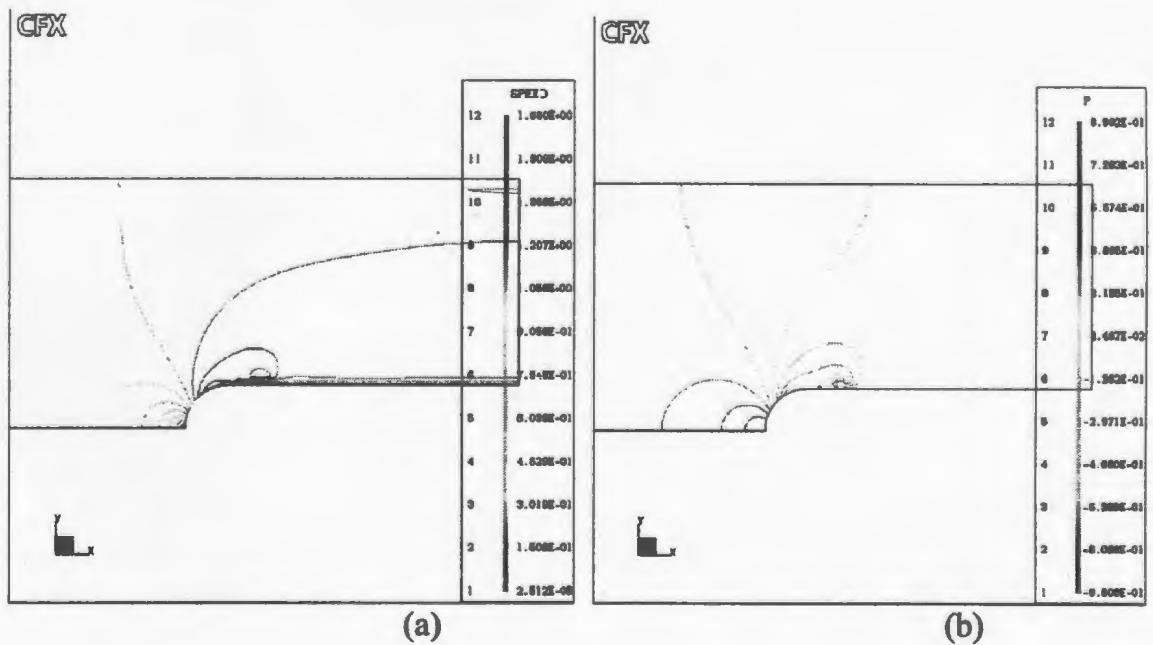


Figure 4.9: (a) Speed contour and (b) pressure contour for the first grid.

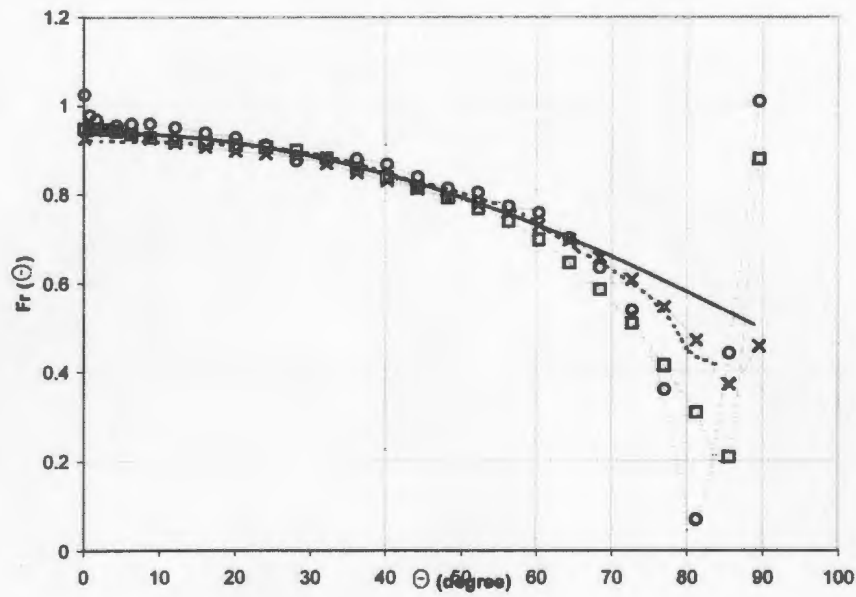


Figure 4.12: Frossling number distribution at different Reynolds numbers.
 Symbols: \square , $Re=6.5 \times 10^3$; x , $Re=1.3 \times 10^4$; \circ , $Re=1.3 \times 10^5$; \cdots , Rigby and VanFossen (1992); — , Frossling (1940).

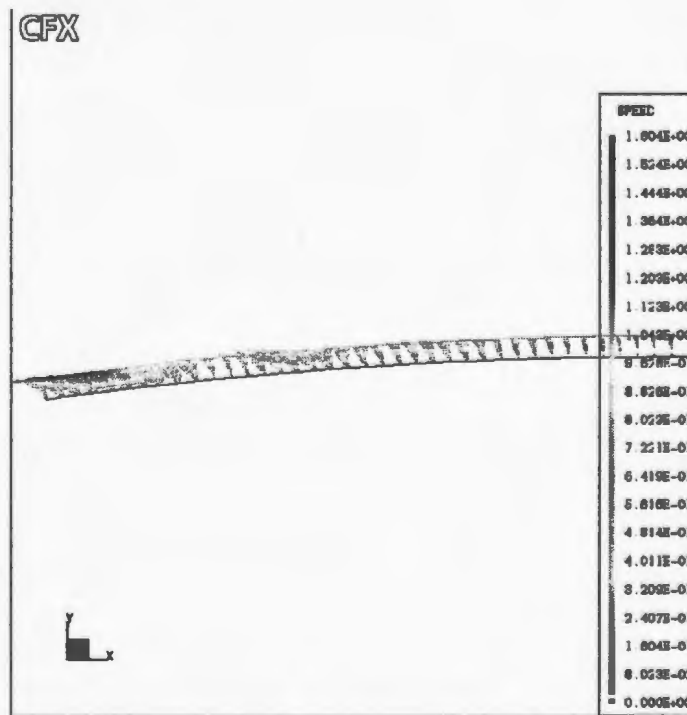


Figure 4.13 The small separation and reattachment at $Re=1.3 \times 10^5$ located in $80^\circ < \theta < 90^\circ$.

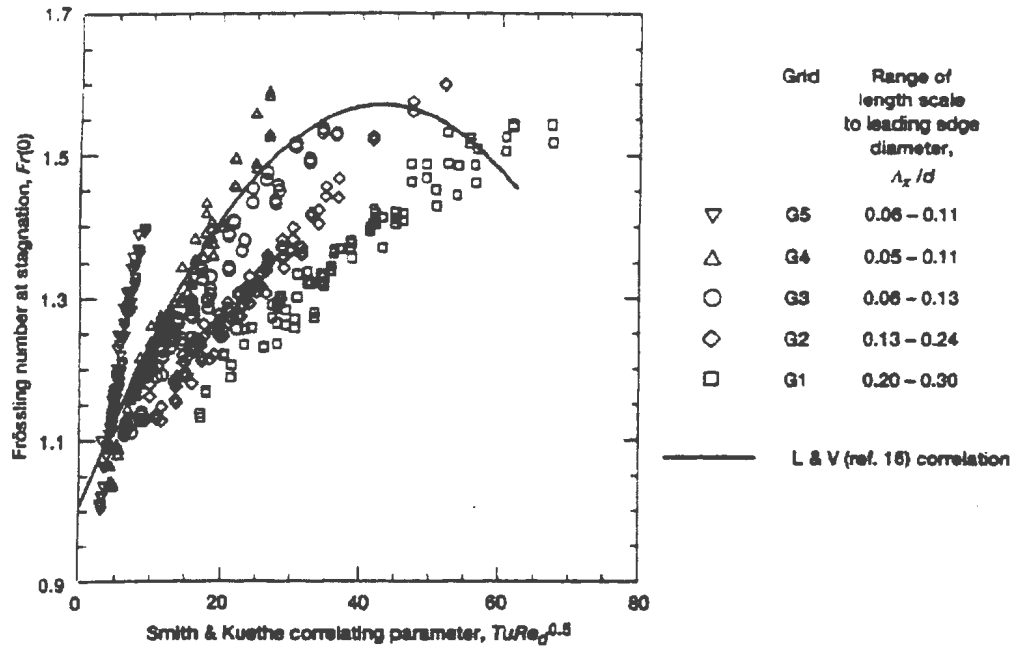


Figure 4. 14 Correlation of stagnation region heat transfer with turbulence freestream proposed by Lowery and Vachon (1997).

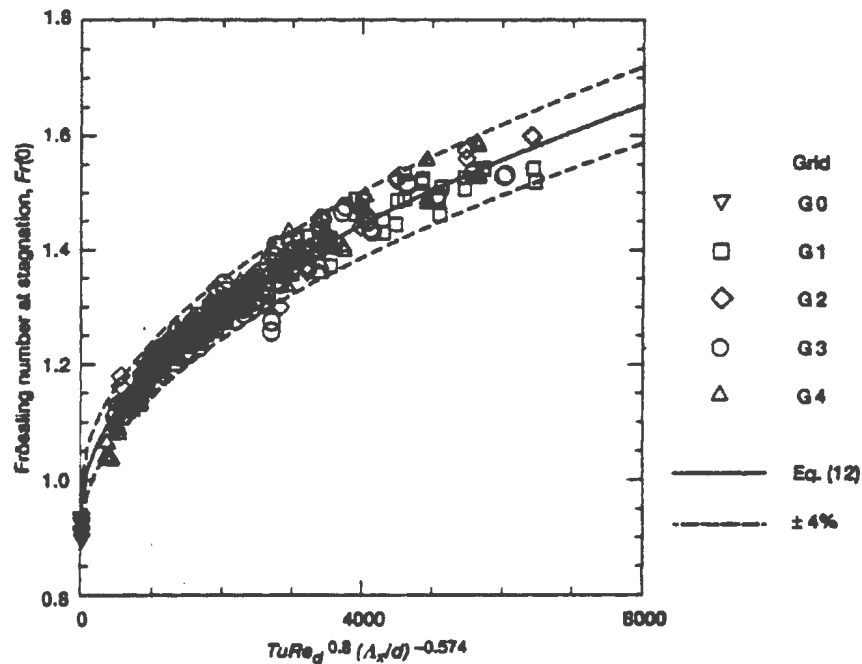


Figure 4. 15 Correlation of stagnation region heat transfer with turbulence freestream proposed by Van Fossen et al. (1995).

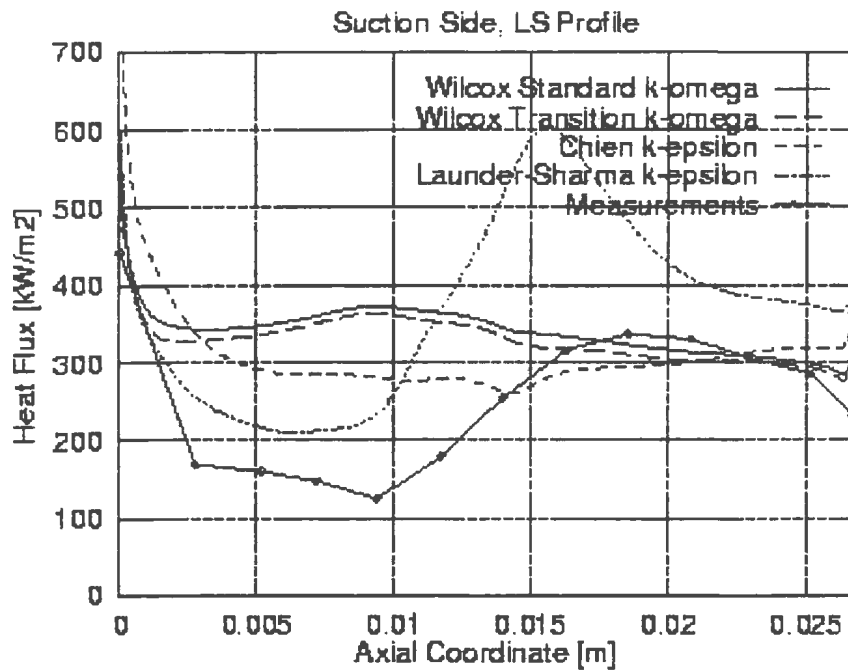


Figure 4.16: The estimation of heat transfer on the suction side of a turbine blade surface (Reproduced from Larsson and Håll, 1998).

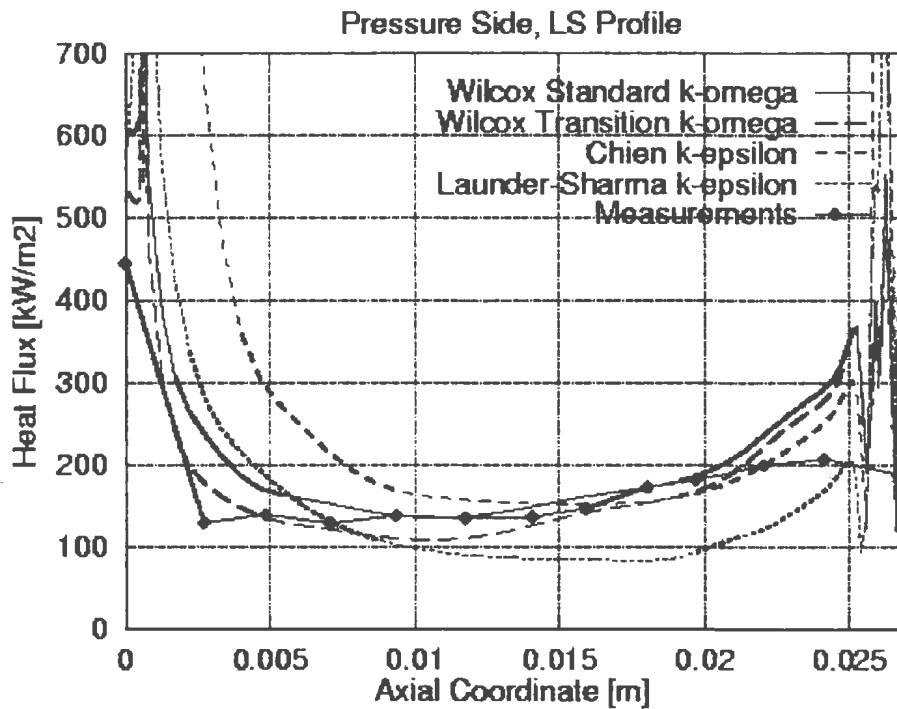


Figure 4.17: The estimation of heat transfer on the pressure side of a turbine blade surface (Reproduced from Larsson and Håll, 1998).

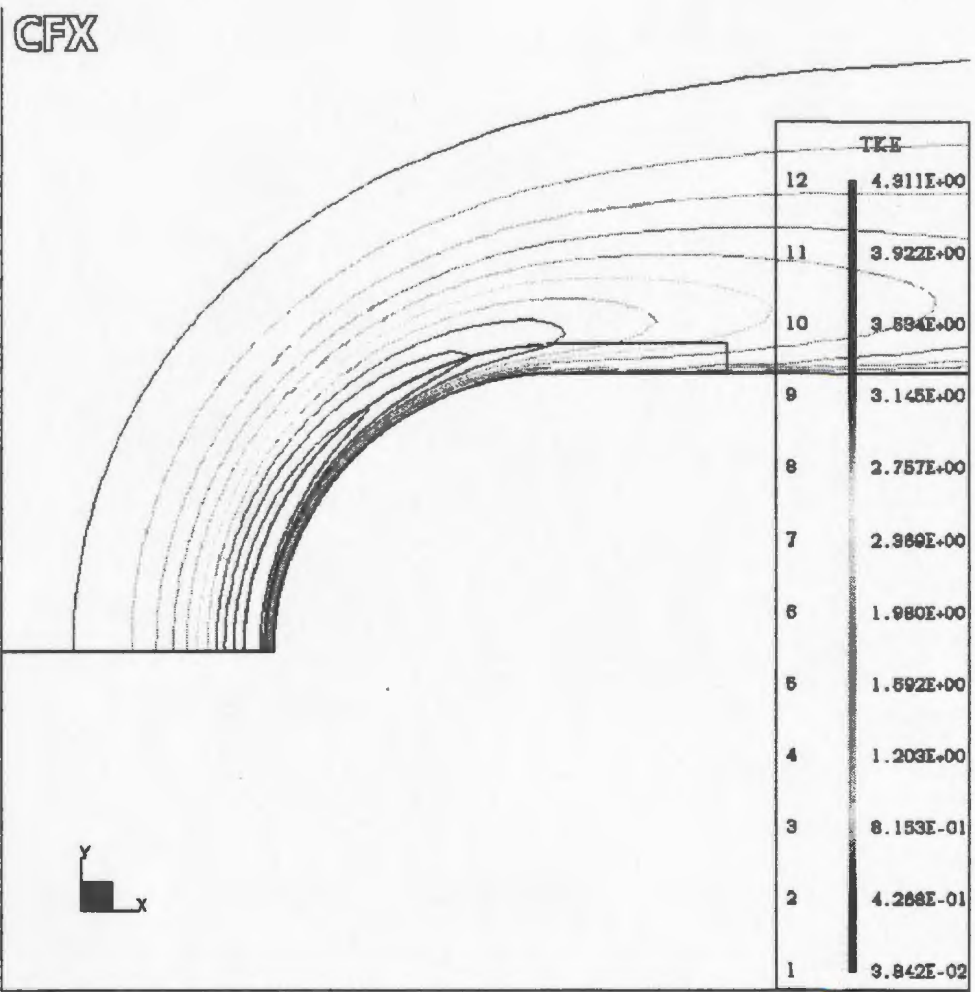


Figure 4.18: Turbulent kinetic energy distribution around the stagnation region.

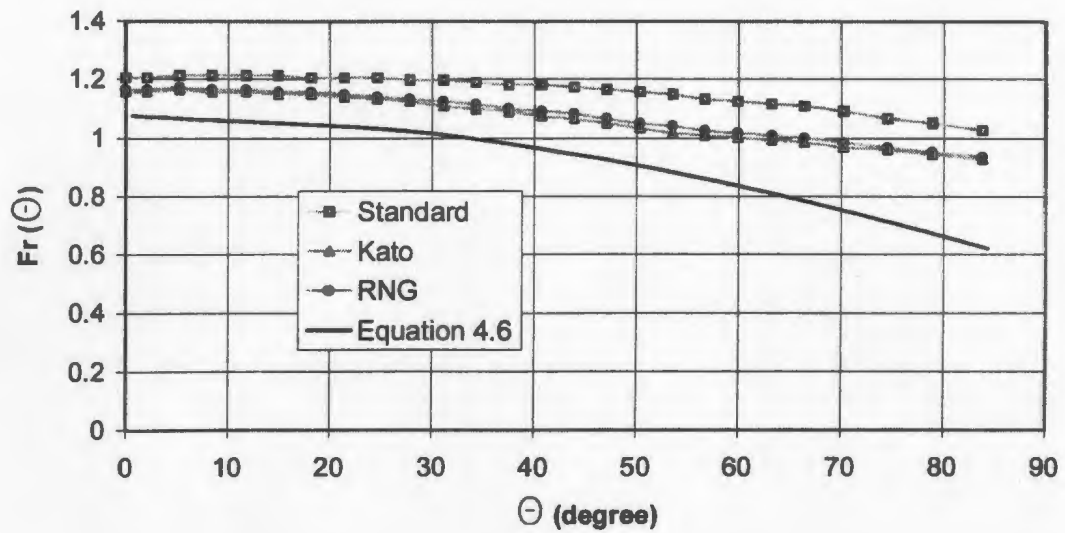


Figure 4.19: Distribution of Frossling numbers for different turbulence models at $Re=1 \times 10^5$, $Tu=0.75\%$ and $\lambda/D=0.98$. Symbols: \square , Standard; \triangle , Kato; \circ , RNG; —, Equation 4.6.

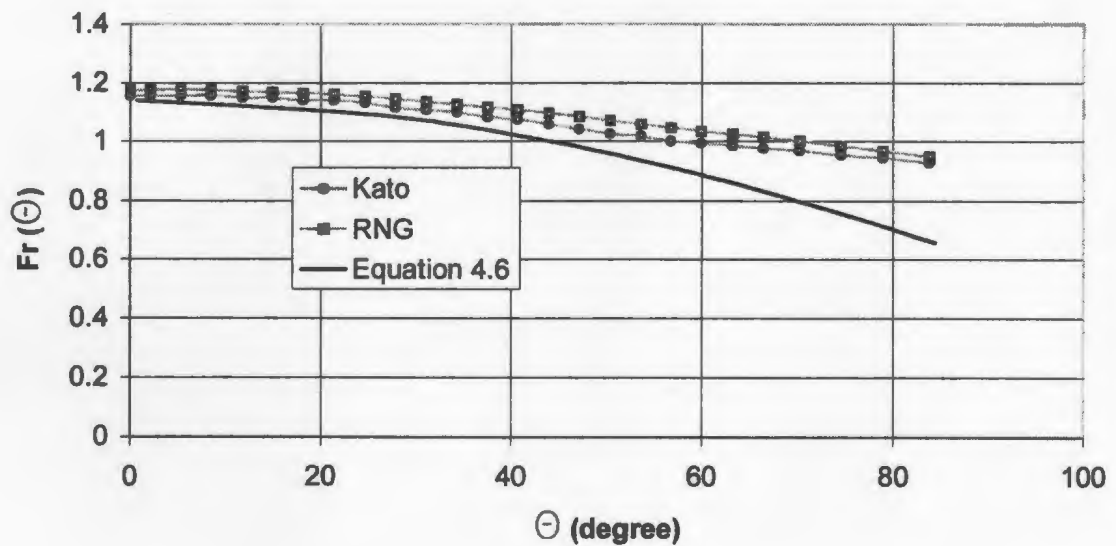
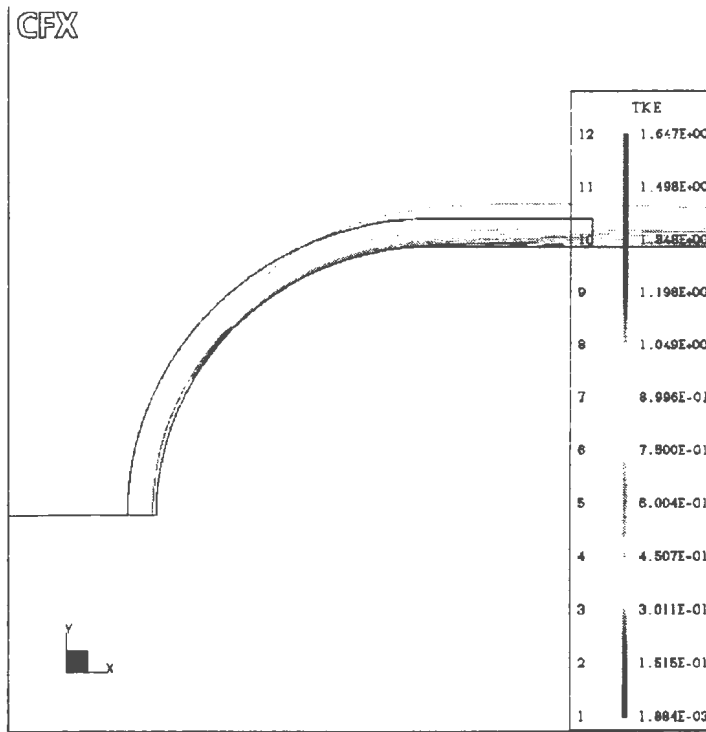
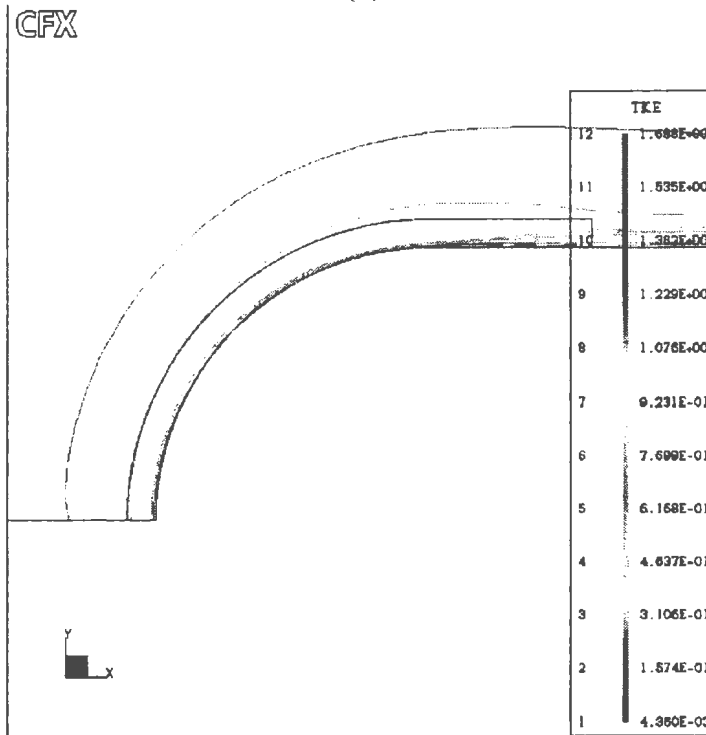


Figure 4.20: Distribution of Frossling numbers for Kato and RNG turbulence models at $Re=5 \times 10^4$, $Tu=5\%$ and $\lambda/D=0.69$. Symbols: \circ , Kato; \square , RNG; —, Equation 4.6.

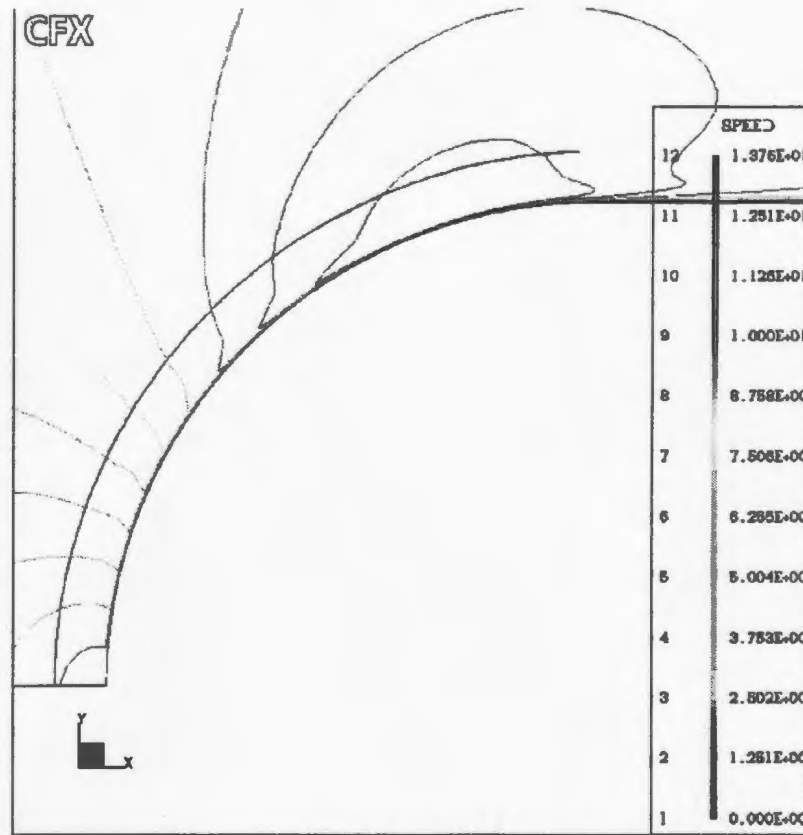


(a)

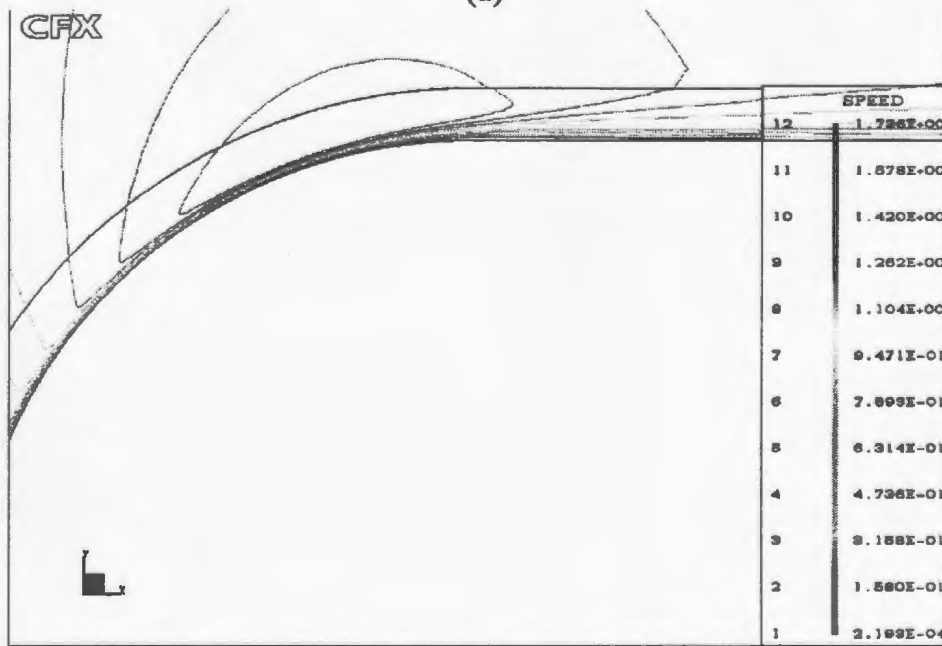


(b)

Figure 4. 21 Turbulence kinetic energy contour at $Re=5 \times 10^4$, $Tu=5\%$ and $\lambda/D=0.69$ (a) Kato, (b) RNG



(a)



(b)

Figure 4. 22 Velocity contours at the final simulation. (a) $Re=10^5$, (b) $Re=1.3 \times 10^4$.

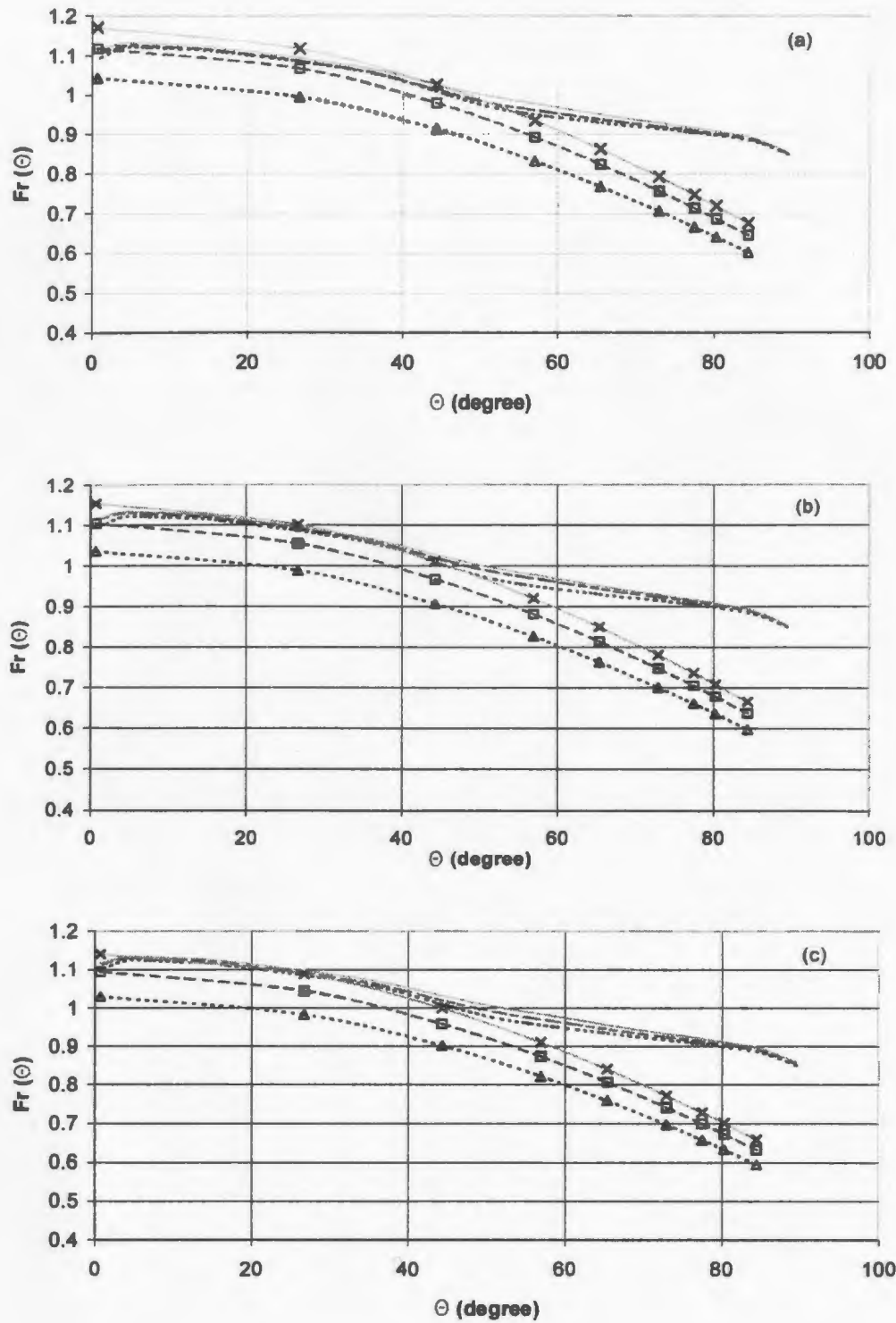


Figure 4.23: Distribution of Frossling numbers for Kato turbulence models at $Re=1. \times 10^5$: (a) $\lambda=0.4282$, (b) $\lambda/D=0.5709$ and (c) $\lambda/D=0.7136$. Symbols: - - - -, $Tu=1\%$; - - - -, $Tu=3\%$; —, $Tu=5\%$; - - Δ - -, $Tu=1\%$ (Eq. 4.6); - - \square - -, $Tu=3\%$ (Eq. 4.6); — \times —, $Tu=5\%$ (Eq. 4.6).

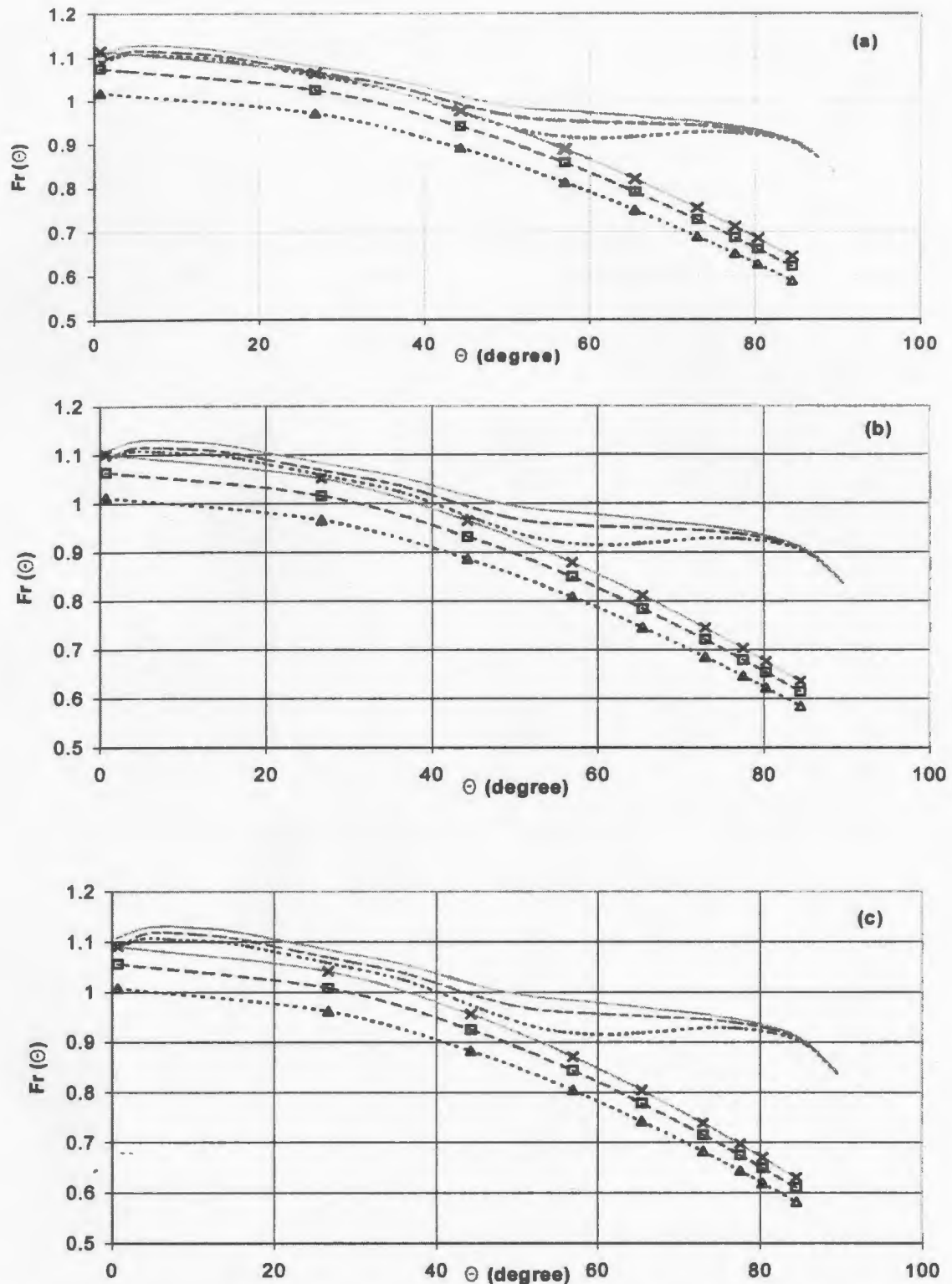


Figure 4.24: Distribution of Frossling numbers for Kato turbulence models at $Re=5.10^4$: (a) $\lambda=0.4282$, (b) $\lambda/D=0.5709$ and (c) $\lambda/D=0.7136$. Symbols: - - - -, $Tu=1\%$; - - - - -, $Tu=3\%$; —, $Tu=5\%$; - - Δ - -, $Tu=1\%$ (Eq. 4.6); - - \square - -, $Tu=3\%$ (Eq. 4.6); — \times —, $Tu=5\%$ (Eq. 4.6).

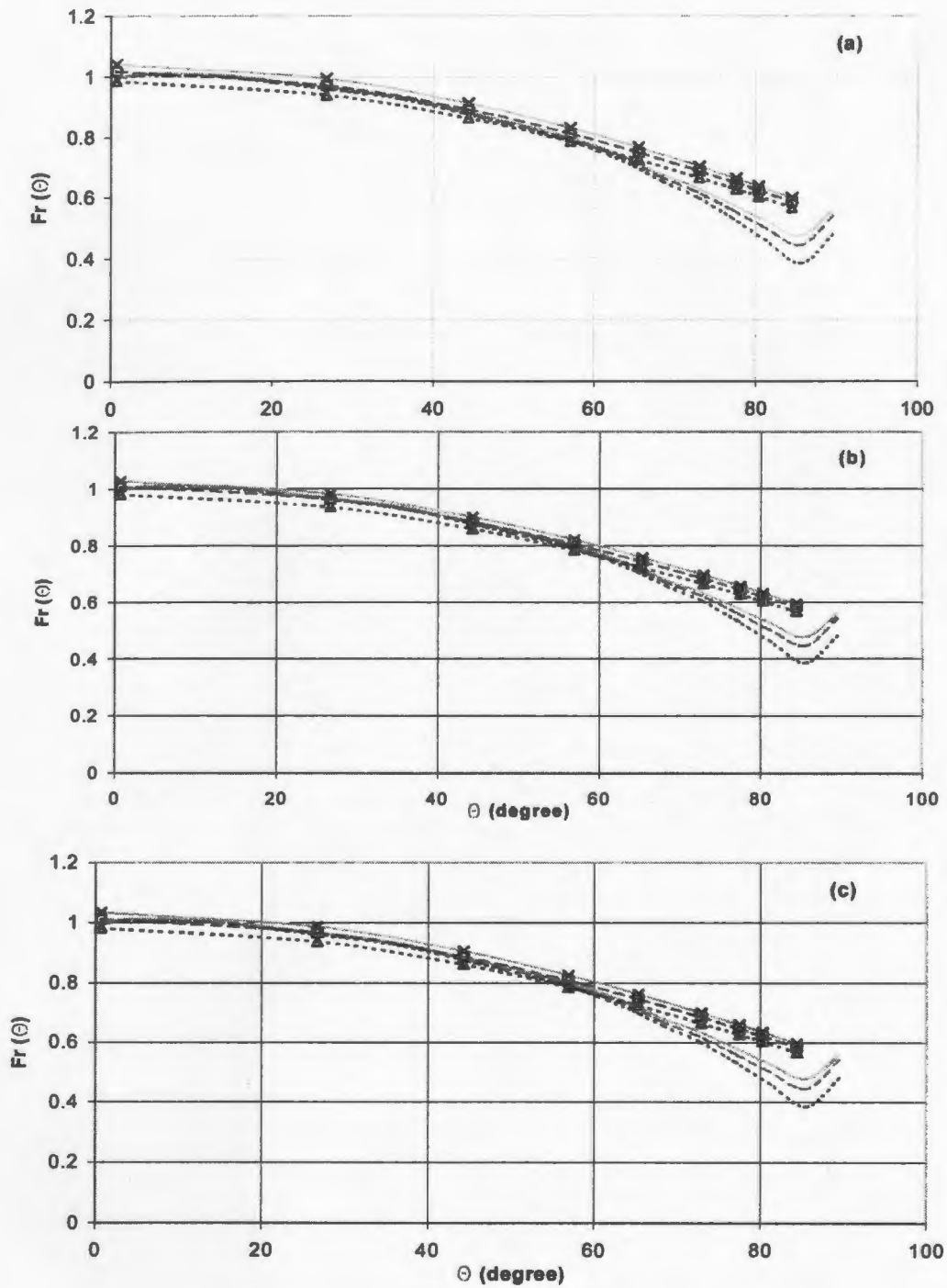


Figure 4.25: Distribution of Frossling numbers for Kato turbulence models at $Re=1.3 \times 10^4$: (a) $\lambda/D=0.4282$, (b) $\lambda/D=0.5709$ and (c) $\lambda/D=0.7136$. Symbols: - - - -, $Tu=1\%$; - - - -, $Tu=3\%$; —, $Tu=5\%$; - - Δ - -, $Tu=1\%$ (Eq. 4.6); - - \square - -, $Tu=3\%$ (Eq. 4.6); — \times —, $Tu=5\%$ (Eq. 4.6).

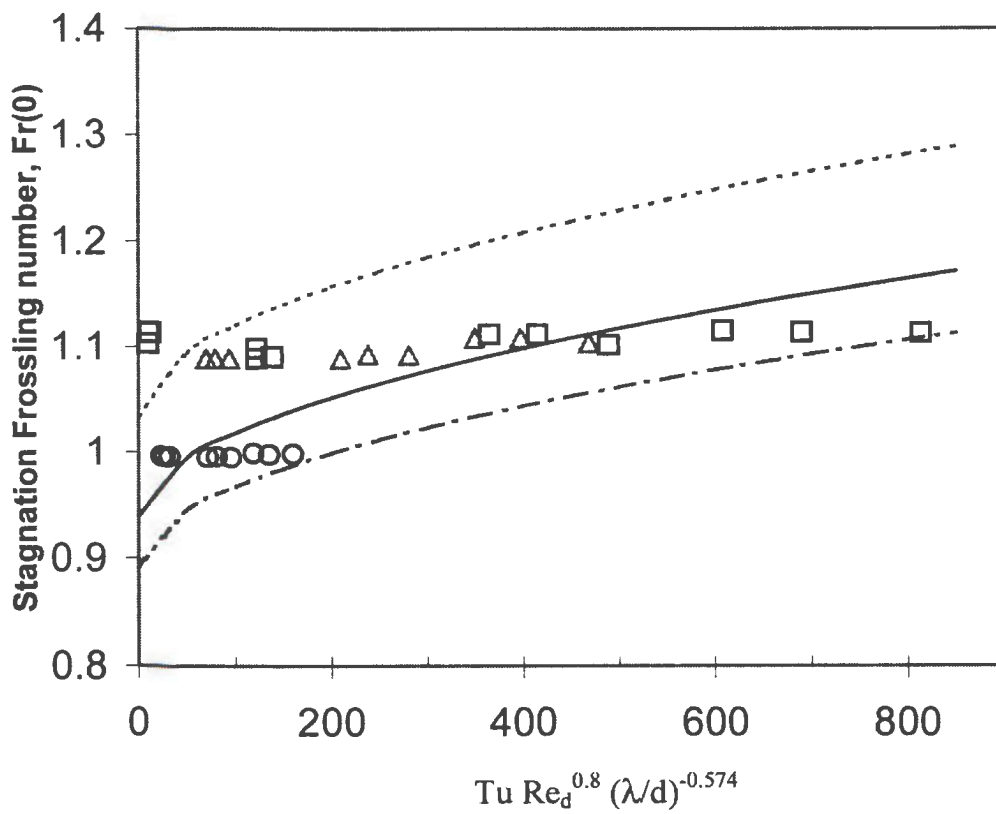


Figure 4.26: Stagnation Frossling number vs. $Tu Re_d^{0.8} (\lambda/D)^{-0.574}$. Symbols: \square , $Re=10^5$; Δ , $Re=5 \times 10^4$; \circ , $Re=1.3 \times 10^4$; —, equation 4.6; - - -, +10%; - · - · -, -5%.

5. Concluding Remarks and Recommendations

5.1 Concluding Remarks

Stagnation region heat transfer is important in many critical applications. Studies in gas turbine blade heat transfer show that the highest heat transfer occurs in the stagnation region. Several experiments and simulations have been performed to understand the physical mechanism of heat transfer augmentation in that region. Experiments have been performed and empirical correlations developed for stagnation region heat transfer with Reynolds number and the turbulence characteristics. Simulations have been performed to estimate the actual heat transfer for practical purposes.

The simulations for this thesis were performed using the CFD code, CFX-TASCflow. The code was validated using a number of standard problems. These consist of flow in a square driven cavity, flow over a flat plate with laminar and turbulent boundary layers, and flow over a backward facing step. Simulations for stagnation region heat transfer consist of laminar freestream with Reynolds numbers ranging from 6.5×10^3 to 6.5×10^5 , and turbulent freestream with the combinations of Reynolds number (1.3×10^4 , 5×10^4 and 10^5), turbulence intensity (1%, 3% and 5%), and the ratio of integral length scales to leading edge diameter (λ/D) of 0.4282, 0.5709 and 0.7136.

The simulation of flow in the square driven cavity was intended to evaluate the performance of the discretization scheme in handling recirculating flows. This is done by comparing the velocity profile at the vertical centreline with Baliga 's (1983) solution. The simulations give good agreement with errors less than six percent. Among the different discretization schemes, Linear Profile Scheme gives the best performance in handling this problem.

The simulations of laminar and turbulent boundary layers over a flat plate were performed to evaluate the performance of turbulence models and the software to resolve the near wall region. The simulations give very good estimation of Nusselt number and skin friction with the errors less than two and seven percent, respectively. In the turbulent boundary layer case, the application of a wall function for flow near the wall region reduces the computational efforts by reducing the number of nodes in the boundary layer. By implementing the standard turbulence model, the best estimation of Nusselt number and skin friction are obtained by locating the first node after the wall between 50 to 150 wall units.

In flow over a backward facing step, three turbulence models, standard, Kato-Launder and RNG are compared in estimating the reattachment length. RNG model underestimates the reattachment length by 18 percent, while the standard and Kato-Launder model overestimate by 2 and 7 percent, respectively. However, the estimations

of turbulent kinetic energy are still in significant error due to the disadvantage of the two-equation turbulence models in simulating a flow with adverse pressure gradients.

The laminar simulations of stagnation region heat transfer give very good agreement with experiment and semi-theoretical solution of the Frossling number distribution. The errors in estimating stagnation Frossling number are as high as 6 percent ($Re=1.3 \times 10^5$). At $Re=1.3 \times 10^5$, Frossling number distribution decreases at $\theta=80^\circ$ and increase sharply at $\theta=90^\circ$, due to the presence of flow separation. The use of LPS as a discretization scheme and grid structure with unity element aspect ratio near the wall are the important considerations in performing an accurate simulation.

By using the same discretization scheme and grid structure of the laminar simulation, the simulations for a turbulent freestream are performed on three cases. Each case has constant Re and different combinations of Tu and λ/D . The simulation results of turbulent freestream are less accurate compared to the laminar simulation with the errors as high as 8 percent. The Frossling number distribution increases with the increase of Re and Tu , and a decrease of λ . At $Re=10^5$, heat transfer simulations have errors ranging from 0.72 % to 7%. Frossling number distribution beyond $\theta=50^\circ$ are higher than the experimental value due to the absence of separation. The second case has similar results with the first case, where Frossling number distribution beyond $\theta=50^\circ$ is higher than the experimental value. The simulations of the second case have errors ranging from

0.71% to 8%. Unlike the first and second cases, the third case simulations contain a small separation at $\theta=90^\circ$ causing a lower Frossling number distribution.

The increase of Frossling number distribution is less sensitive compared to the experiment, especially with the increase of Tu and the decrease of λ . The sources of inaccuracy can be attributed to the inadequate distance of the first node after the wall, the use of single precision storage and the disadvantage of $k-\epsilon$ turbulence models in simulating flow over a curved body.

5.2. Recommendations

Some recommendations are proposed to increase the accuracy of simulation for stagnation region heat transfer under a turbulent freestream.

1). Increase computer memory (RAM)

By increasing computer memory, additional grids can be located near the wall, so that the first grid is located in the viscous sublayer. This condition will maintain the consistency of the two-layer turbulence model implementation and in turn, increase the accuracy of the simulation.

2). Using double precision storage system

By storing variables of simulation in double precision, the truncation error during iteration can be reduced, and the solution will be more accurate. Double precision system

also maintains the accuracy of the calculation with two-layer turbulence models that require the first grid after the wall to be located in the viscous sublayer.

3). Using Second-Order Closure models

Second-Order Closure models have additional governing equations for the Reynolds-stress tensor that accommodate sudden changes in strain rate and establish suitable time scales for the k and ε equations. This ability will reduce errors that arise during simulation of flow over a curved body, such as flow in the stagnation region using k - ε turbulence models as performed in this thesis.

References

1. Abbott, I. H., and Doenhoff, A. E., 1959, *Theory of Wing Sections, Including a Summary of Airfoil Data*,
2. Abdol-Hamid, K.S., Lakshmanan, B., and Carlson, J.R., 1995, Application of Navier-Stokes Code PAB3D with k - ϵ Turbulence Model to Attached and Separated Flow, NASA Technical Paper 3480.
3. Achenbach, E., 1975, Total and Local Heat Transfer From a Smooth Circular Cylinder in Cross-Flow at High Reynolds Number, *International Journal of Heat and Mass Transfer*, Vol. 18, pp. 1387-1396.
4. Amano, R.S., 1984, Development of a Turbulence Near-Wall Model and its Application to Separated and Reattached Flows, *Numerical Heat Transfer*, Vol 7, pp. 59-75.
5. Ameri, A., Sockol, P. M., and Gorla, R. S. R., 1992. Navier-Stokes Analysis of Turbomachinery Blade External Heat Transfer, *Journal of Propulsion and Power* Vol. 8, No. 2, pp. 374-381.
6. Anderson, D. A., Tannehill, J. C., and Pletcher, R. H., 1984, *Computational Fluid Mechanics and Heat Transfer*, McGraw-Hill, New York.
7. Anderson, J.D., Anderson, Jr., and David, J., 1995. *Computational Fluid Dynamics : the Basics with Applications*, McGraw-Hill, New York.
8. Arima, T., Sonoda, T., Shirotori, M., Tamura, A., and Kikuchi, K., 1999, A Numerical Investigation of Transonic Axial Compressor Rotor Flow Using a Low-Reynolds-Number k - ϵ Turbulence Model, *Journal of Turbomachinery* Vol. 121 pp. 44-58.

9. Asvapoositkul, W., and Zangeneh, M., A Time-Marching Method for the Calculation of Nonsimilar 3D Boundary Layers on Turbomachinery Blades, *Journal of Fluid Engineering*, Vol. 120, pp. 799-807.
10. Azouz, Idir, and Shirazi, Siamack A., 1997, Numerical Simulation of Drag Reducing Turbulent Flow in Annular Conduits, *Journal of Fluid Engineering*, Vol. 119, pp. 838-846.
11. Badran, O.O., Bruun, H.H., 1999, Comparison of Flying-Hot-Wire and Stationary-Hot-Wire Measurement of Flow Over a Backward-Facing Step, *Journal of Fluid Engineering*, Vol. 121, pp. 441-445.
12. Baliga , B.R., and Patankar, S.V., 1983, A Control Volume Finite-Element Method for Two-Dimensional Fluid Flow and Heat Transfer, *Numerical Heat Transfer*, Vol 6, pp. 245-261.
13. Baliga , B.R., and Pham, T.T., 1983, Solution of Some Two-Dimensional Incompressible Fluid Flow and Heat Transfer Problems, Using a Control Volume Finite-Element Methods, *Numerical Heat Transfer*, Vol 6, pp. 263-282.
14. Ballio, F., Bettoni, C., Franzetti, S., 1998, A Survey of Time-Averaged Characteristics of Laminar and Turbulent Horseshoe Vortices, *Journal of Fluid Engineering*, Vol. 120, pp. 233-242.
15. Bardina, J.E., Huang, P.G., and Coakley, T.J., 1997, Turbulence Modelling Validation, Testing, and Development, NASA Technical Memorandum 110446.
16. Bathie, W. W., 1996, Fundamentals of Gas Turbines, 2nd Ed., John Willey & Sons, Inc., USA.
17. Blottner, F.G., 1978, Numerical Solution of Diffusion-Convection Equations, *Computers and Fluids*, Vol 6, pp. 15-24.

18. Bogaerts, S., Degrez, G., Razafindrakoto, E., 1978, Upwind Residual Distribution Schemes for Incompressible Flows, Technical Memoranda 30-1998, von Karman Institute for Fluid Dynamics, Belgium.
19. Bottin, B., Carbanaro, M., and Schroder, W., 199, Calibration and Application of a Flexible Wall Adaptation Technique on a NACA0012 Airfoil, Technical Notes 41 von Karman Institute for Fluid Dynamics, Belgium.
20. Boussinesq, J., 1877, Essai sur la théorie des eaux courantes, *Mem. Pres. Acad. Sci.* XXIII, 46, Paris.
21. Bradshaw, Peter, 1994, Turbulence: the Chief Outstanding Difficulty of Our Subject, *Experiments in Fluids*, Vol. 16, pp. 203-216.
22. Cai, R., 1998, Some Explicit Analytical Solutions of Unsteady Compressible Flow, *Journal of Fluid Engineering*, Vol. 120, pp. 760-764.
23. Caughey, D.A., 1988, Diagonal Implicit Multigrid Algorithm for the Euler Equation, *AIAA Journal*, Vol. 26, No. 7, pp. 1841-851.
24. CFX-TASCflow, 1999a, *Theory Documentation*, AEA Technology Engineering Software, Ltd., Waterloo, Ontario.
25. CFX-TASCflow, 1999b, *Tutorial Documentation*, AEA Technology Engineering Software, Ltd., Waterloo, Ontario.
26. CFX-TASCflow, 1999c, *User Documentation*, AEA Technology Engineering Software, Ltd., Waterloo, Ontario.
27. Chen, H.C. and Patel, V.C., 1988, Near-Wall Turbulence Models for Complex Flows Including Separation, *AIAA Journal*, Volume 26, Number 6, pp. 641-648.
28. Chernobrovkin, A., and Lakshminarayana, B., 1998, Turbulence Modeling and Computation of Viscous Transitional Flows for Low Pressure Turbines, *Journal of Fluid Engineering*, Vol. 121, pp. 824-833.

29. Chung, T.J., 1978, *Finite Element Analysis in Fluid Dynamics*, 1st Ed., McGraw-Hill, New York.
30. Coleman, H. W., and Stern, F., 1997, Uncertainties and CFD Code Validation, *Journal of Fluid Engineering*, Vol. 119, pp. 795-803.
31. Comini, G., and Giudice, S.D., 1985, A (k- ϵ) Model of Turbulence, *Numerical Heat Transfer*, Vol 8, pp. 133-147.
32. Day, C.R.B., Oldfield, M.L.G., and Lock, G.D., 1999, The influence of Film Cooling on the Efficiency of an Annular Nozzle Guide Vane Cascade, *Journal of Turbomachinery ASME*, Vol. 121, pp. 145-151.
33. Degrez, G., Deconinck, H., 1999, Multidimensional Upwind Residual Distribution Schemes and Applications. Technical Notes 41 von Karman Institute for Fluid Dynamics, Belgium.
34. Du, H., Han, J. C., and Ekkad, S. V., 1998, Effect of Unsteady Wake on Detailed Heat Transfer Coefficient and Film Effectiveness Distributions for Gas Turbine Blade, *Journal of Fluid Engineering*, Vol. 120, pp. 808-817.
35. Dullenkopf, K. and Mayle, R. E., 1995, An Account of Free-Stream-Turbulence Length Scale on Laminar Heat Transfer, *Journal of Turbomachinery*, Vol. 117, pp. 401-406.
36. Eckert, E.R.G., and Drake Jr., Robert M., 1987 *Analysis of Heat and Mass Transfer*, McGraw-Hill Book Co., 2nd ed., New York.
37. Eckert, E.R.G., and Drake, R.M., *Heat and Mass Transfer*, McGraw-Hill Book Co., 2nd ed. 1959, New York.
38. Ekkad, S. V., Han, J. C., and Du, H., 1998, Detailed Film Cooling Measurements on a Cylindrical Leading Edge Model: Effect of Free-Stream Turbulence and Coolant Density, *Journal of Turbomachinery*, Vol. 120, pp. 799-807.

39. Fletcher, C.A.J., 1991. *Computational Techniques for Fluid Dynamics Vol.1*, Springer-Verlag Berlin.
40. Fletcher, C.A.J., 1991, *Computational Techniques for Fluid Dynamics Vol. 2*, Springer-Verlag Berlin.
41. Van Fossen, G. J., Simoneau, Robert J., Ching, Can Y., 1994. Influence of Turbulence Parameters, Reynolds Number, and Body Shape on Stagnation-Region Heat Transfer, NASA Technical Paper 3487.
42. Frossling, N., 1940, Evaporation Heat Transfer and Velocity around Two Dimensional and Rotational Symmetrical Boundary Layer Flow (in German), Lunds Universitat, Arkive Physik Part 2, 36, No.4.
43. Frossling, N., 1940, Evaporation, Heat Transfer, and Velocity Distribution in Two-dimensional and Rotationally Symmetrical Laminar Boundary Flow, Technical Report TM-1432, NACA.
44. Gerolymos, G.A., 1988, Numerical Integration of the Blade-to-Blade Surface Euler Equations in Vibrating Cascades, *AIAA Journal*, Vol. 26, No. 11, pp. 1483-1492.
45. Ghosal, Sandip, 1999, Mathematical and Physical Constraints on Large Eddy Simulation of Turbulence, *AIAA Journal*, Vol. 37, No. 4, pp. 425-433.
46. Goldberg, U., Perroomian, O., and Chakravarthy, S., 1998, A Wall-Distance-Free $k-\epsilon$ Model With Enhanced Near-Wall Treatment, *Journal of Fluid Engineering*, Vol. 120, pp. 457-462.
47. Greiner, M., Chen, R. -F., Wirtz, R.A., 1995, Augmentated Heat Transfer in a Recovery Passage Downstream From a Grooved Section: An Example of Uncoupled Heat/Momentum Transport, *Journal of Heat Transfer*, Vol 117, May 1995, pp. 303-309.

48. Guo, S. M., Jones, T. V., Lock, G. D., and Dancer, S. N., 1998, Computational Prediction of Heat Transfer to Gas Turbine Nozzle Guide Vanes With Roughened Surface, *Journal of Turbomachinery*, Vol. 120, pp. 343-350.
49. Hanjalic, K., Hadzic, I., and Jakirlic, S., 1999, Modeling Turbulent Wall Flows Subjected to Strong Pressure Variations, *Journal of Fluid Engineering*, Vol. 121, pp. 57-64
50. Hartwich, P.M., Hsu, C.H., 1988, Resolution Upwind Schemes for Three-Dimensional Incompressible Navier-Stokes Equation, *AIAA Journal*, Vol. 26, No. 11, pp. 1321-1328.
51. Hattori, H., 1999, Two Layer Turbulence Model For Heat Transfer in Wall Turbulent Shear Flows, Proceeding of the 5th ASME/JSME Joint Thermal Engineering Conference San Diego, California, pp. 1-8.
52. Hayase, T., 1999, Monotonic Convergence Property of Turbulent Flow Solution With Central Difference and QUICK Schemes, *Journal of Fluid Engineering*, Vol. 121, pp. 351-358.
53. Hookey, Neil A., *Evaluation and Enhancements of Control-Volume Finite-Element Methods for Two-Dimensional Fluid Flow and Heat Transfer*, M. Eng. Thesis, McGill University, Montreal, 1986.
54. Hutchinson, B.R., and Raithby, G.D., 1986, A Multigrid Methods Based on the Additive Correction Strategy, *Numerical Heat Transfer*, Vol 9, pp. 511-537.
55. Incropera, Frank P., and Dewitt, D. P., *Fundamentals of Heat and Mass Transfer*, John Willey&Sons, 1990, New York.
56. Jou, W.H., 1983, Finite Volume Calculation of Three-Dimensional Potential Flow Around a Propeller, *AIAA Journal*, Vol. 21, No. 10, pp. 1360-1364.

57. Kader, B.A., 1981, Temperature and Concentration Profiles in Fully Turbulent Boundary Layers, *International Journal of Heat and Mass Transfer*, Vol. 24, Number 9, pp. 1541-1544.
58. Kasagi, Nobuhide, and Iida, Oaki , 1999. Progress in Direct Numerical Simulation of Turbulent Heat Transfer, Proceeding of the 5th ASME/JSME Joint Thermal Engineering Conference San Diego, California, pp. 1-17.
59. Kestin, J., 1966, The Effect of Freestream Turbulence on Heat Transfer Rates. *Advanced in Heat Transfer*, Vol.3, pp. 1-32.
60. Klewicki, J.C., and Hill, R.B., 1998. Spatial Structure of Negative $\partial u/\partial y$ in a Low Re Turbulent Boundary Layer, *Journal of Fluid Engineering*, Vol. 120, pp. 772-777.
61. Knight, D.D. and Degrez, G., 1997, Shock Wave Boundary Layer Interactions in High Mach Number Flow. A Critical Survey of Current CFD prediction Capability, Technical Memoranda VKI RP 1997-15, von Karman Institute for Fluid Dynamics, Belgium.
62. Kohli, A., and Bogard, D. G., 1998, Numerical Simulation of a Turbulent Flow in a Channel with Surface Mounted Cubes, *Journal of Turbomachinery*, Vol. 120, pp. 785-790.
63. Larson, J., 1997, Turbine Blade Heat Transfer Calculations using Two-equation Turbulence Models, *ImechE*, Vol. 211 Part A, pp. 253-262.
64. Larsson, J., and Håll, U., 1998, Simulations and Measurements on Impulse Blades for Heat Transfer Prediction in Supersonic Turbine Applications, Proc. of the ASME Turbo Expo, Stockholm.
65. Larsson, J., Eriksson, Lars-Erik, and Håll, Ulf, 1995, External Heat Transfer Predictions in Supersonic Turbines Using The Reynolds Averaged Navier-Stokes Equations, Proc. 12th ISABE Conference, Melbourne, Vol. 2, pp. 11-2-1112.

66. Latimer, B.R., and Pollard, A., 1985, Comparison of Pressure-Velocity Coupling Solution Algorithms, *Numerical Heat Transfer*, Vol 8, pp. 635-652.
67. Lavante, E.V., and Thompkins Jr., W.T., 1983, An Implicit, Bidiagonal Numerical Method for Solving the Navier-Stokes Equations,' *AIAA Journal*, Vol. 21, No. 11, pp. 828-833.
68. Lambert de Rouvriot, M., Art, T., 1997, Numerical Aero-Thermal Prediction of Laminar/Turbulent Flows in a Two-Dimensional High Pressure Turbine Linear Cascade, Second European Conference on Turbomachinery-Fluid Dynamics and Thermodynamics, Antwerp, Belgium, March 5-7, 1997, pp 401-409
69. Lowery, G.W., and Vachon, R.I., 1975, The Effect of Turbulence on Heat Transfer from Heated Cylinder, *International Journal of Heat and Mass Transfer*. Vol. 18, pp. 1229-1242.
70. Mansour, N. N., Kim., J. and Moin, P., 1988, Reynolds-stress and Dissipation Rate Budgets in Turbulent Channel Flow, *Journal of Fluid Mechanics*, Vol 194, pp. 15-44.
71. Marvin, J.G., 1983, Turbulence Modelling for Computational Aerodynamics, *AIAA Journal*, Vol. 21, No. 7, pp. 941-955.
72. Mayle, R. E., Dullenkopf, K., and Schulz, A., 1998, The Turbulence That Matters, *Journal of Fluid Engineering*, Vol. 120, pp. 402-409.
73. Mehendale, A.B., Han, J.C., and Ou, S., 1991, Influence of High Mainstream Turbulence on Leading Edge Heat Transfer, *Journal of Heat Transfer*, Vol 113, November 1991, pp. 843-849.
74. Menter, F. R., 1997, Eddy Viscosity Transport Equations and Their Relation to the $k-\epsilon$ Model, *Journal of Fluid Engineering*, Vol. 119, pp. 876-884.
75. Murthy, S.N.B., 1977, *Turbulence in Internal Flow*, Hemisphere Publishing Corp., Washington.

76. Paciorri, R., Dieudonné, W., Degrez, G., Charbonnier, J.M., and Deconinck, H., 1997, Validation of the Spalart-Allmaras Turbulence Model for Application in Hypersonic Flows, AIAA Paper 97-2023.
77. Panis, Jean-François, and Pérault, Michel, 1997, Numerical Study of the Effective Viscosity and Pressure in Perturbed Turbulent Flows, *Physics of Fluids*, Vol. 10, No. 12, pp. 3111-3125.
78. Panton, Ronald L., 1984, *Incompressible Flow*, John Wiley&Sons, New York.
79. Papanicolaou, E.L., and Rodi, W., 1999, Computation of Separated-Flow Transition Using a Two-Layer Model of Turbulence, *Journal of Turbomachinery*, Vol. 121, pp. 78-87.
80. Patankar, Suhas V., 1980, *Numerical Heat Transfer and Fluid Flow*, McGraw-Hill, New York.
81. Patel, M.K., Markatos, N.C., Cross, M., 1985, A Critical Evaluation of Seven Discretization Schemes for Convection-Diffusion Equations, *International Journal for Numerical Methods in Fluids*, Vol. 5, pp. 225-244.
82. Peng, Shia-Hui, Davidson, Lars, and Holmberg, Sture, 1997, A Modified Low-Reynolds-Number $k-\epsilon$ Model for Recirculating Flow, *Journal of Fluid Engineering*, Vol. 119, pp. 867-875.
83. Phillips, R.E., and Schmidt, F.W, 1984, Multigrid Techniques for the Solution of the Numerical Solution of the Diffusion Equation, *Numerical Heat Transfer*, Vol 7, pp. 251-268.
84. Phillips, R.E., and Schmidt, F.W, 1985a, A Multilevel-Multigrid Technique For Recirculating Flows, *Numerical Heat Transfer*, Vol 8, pp. 573-594.
85. Phillips, R.E., and Schmidt, F.W., 1985b, Multigrid Techniques for the Solution of the Passive Scalar Advection-Diffusion Equation, *Numerical Heat Transfer*, Vol 8, pp. 25-43.

86. Prakash, C. and Patankar, S.V., 1985, A Control Volume-Based Finite Element Method For Solving The Navier-Stokes Equation Using Equal-Order Velocity-Pressure Interpolation. *Numerical Heat Transfer*, Vol 8, pp. 259-280.
87. Prakash, C., 1986, An Improved Control Volume Finite-Element Method for Heat and Mass Transfer, and for Fluid Flow Using Equal-Order Velocity-Pressure Interpolation, *Numerical Heat Transfer*. Vol 9, pp. 253-276.
88. Raithby, G.D., Galpin P.F., and VanDoormaal, J.P., 1986, Prediction of Heat and Fluid Flow in Complex Geometries Using General Orthogonal Coordinates, *Numerical Heat Transfer*, Vol 9, pp. 125-142.
89. Ramadhyani, S., and Patankar, S.V., 1985, Solution of the Convection-Diffusion Equation by a Finite-Element Method Using Quadrilateral Elements, *Numerical Heat Transfer*, Vol 8, pp. 595-612.
90. Reynolds, A. J., 1974, *Turbulent Flows in Engineering*, John Wiley, New York.
91. Rhie, C.M., and Chow, W.L., 1983, Numerical Study of the Turbulent Flow Past an Airfoil with Trailing Edge Separation, *AIAA Journal*, Vol. 21, No. 11, pp. 1525-1532.
92. Rigby, D.L., and Van Fossen G.J., 1991, Increased Heat Transfer to a Cylindrical Leading Edges Due to Spanwise Velocity Variations in the Freestream, AIAA Paper 91-1739, AIAA 29th Aerospace Sciences Meeting, Reno, Nevada, U.S.A.
93. Rigby, D.L., and Van Fossen G.J., 1992, Increased Heat Transfer to Elliptical Leading Edges Due to Spanwise Variations in the Freestream Momentum: Numerical and Experimental Results, AIAA Paper 92-3070, AIAA 29th Aerospace Sciences Meeting, Reno, Nevada, U.S.A.
94. Rodi, W., 1980, *Turbulence Models and Their Application in Hydraulics- A State of The Art Review*, International Association for Hydraulic Research, Rotterdam.

95. Rodi, W., 1991, Experience with Two-Layer Models Combining the k- ϵ Model with a One-Equation Model Near The Wall', AIAA Paper 91-0216, AIAA 29th Aerospace Sciences Meeting, Reno, Nevada, U.S.A.
96. Schlichting, H., 1979, *Boundary Layer Theory*, McGraw- Hill Book Co., 7th ed.1959, NewYork.
97. Schneider, G.E., and Raw, M.J., 1986, A Skewed, Positive Influence Coefficient Upwinding Procedure for Control-Volume-Based Finite-Element Convection-Diffusion Computation, *Numerical Heat Transfer*, Vol 9, pp. 1-26.
98. Schneider, G.E., and Raw, M.J., 1987a, Control Volume Finite-Element Method for Heat Transfer and Fluid Flow Using Colocated Variables-I. Computational Procedure, *Numerical Heat Transfer*, Vol 11, pp. 363-390.
99. Schneider, G.E., and Raw, M.J., 1987b, Control Volume Finite-Element Method for Heat Transfer and Fluid Flow Using Colocated Variables-I. Application and Validation, *Numerical Heat Transfer*, Vol 11, pp. 390-399.
100. Sengupta, S., 1988, Numerical Grid Generation in Computational Fluid Mechanics '88, International Conference on Numerical Grid Generation in Computational Fluid Dynamics and Related Fields, Swansea, Wales, UK.
101. Simoneau, Robert J. and Simon, Frederick F., 1993, Progress Toward Understanding and Predicting Heat Transfer in the Turbine Gas Path, *Int. J. Heat and Fluid Flow*, Vol.14, No. 2, pp. 106-118.
102. Smith, Leslie M., and Woodruff, Stephen L., 1998, Renormalization-Group Analysis of Turbulence, *Annu. Rev. Fluid Mech.*, Vol 30, pp. 275-310.
103. Sohankar, Ahmad, and Norberg, C., Davidson, L., 1999, Simulation of Three-Dimensional Flow Around a Square Cylinder at Moderate Reynold numbers, *Physics of Fluids*, Vol.11, No. 2, pp. 288-306.

104. Straatman, G. A., 1999, A Modified Model for Diffusion in Second-Moment Turbulence Closures, *Journal of Fluid Engineering*, Vol. 121, pp. 747-756.
105. Streeter, Victor L., Wylie, E.B, 1971, *Fluid Mechanics*, McGraw-Hill, New York.
106. Sutera, S., Kestin J., and Maeder, P., 1963, On the Sensitivity of Heat Transfer in the Stagnation Point Boundary Layer to Free-stream Vorticity, *J. Fluid Mech.* 16, pp. 497-520.
107. Tan, B. T., Thompson, M. C., and Hourigan, K., 1998, Simulated Flow around Long Rectangular Plates under Cross Flow Perturbations, *International Journal of Fluid Dynamics*, Vol. 2, Art. 1
108. Taulbee, D. B., Tran, L., and Dunn, M. G., 1989, Stagnation Point and Surface Heat Transfer for a Turbine Stage: Prediction and Comparison With Data, *Transactions of ASME*, Vol. 111, pp.28-35.
109. Van Doormaal, J.P., and Raithby, G.D., 1984, Enhancements of The Simple Methods For Predicting Incompressible Fluid Flows, *Numerical Heat Transfer*, Vol 7, pp. 147-163.
110. VanDyke, Milton, 1982, *An Album of Fluid Motion*, THE PARABOLIC PRESS, Stanford, California.
111. Vasilliev, V. I., Volkov, D. V., Zaitsev, S. A., and Lyubimov, D. A., 1997, Numerical Simulation of Channel Flow by a One-Equation Turbulence Model, *Journal of Fluid Engineering*, Vol. 119, pp. 885-892.
112. Verstapen, R. W. C. P., and Veldman, A. E. P., 1998, Numerical Simulation of a Turbulent Flow in a Channel with Surface Mounted Cubes, *Applied Scientific Research*, Vol. 59, pp. 395-408.
113. Versteeg, H.K., and Malalasekera, W., 1995, *An Introduction to CFD: The Finite Volume Method*, Longman Scientific & Technical, New York.

114. Wendt, John F., **Computational Fluid Dynamics: An Introduction**, Springer-Verlag Berlin Heidelberg, 1996
115. Westin, K. J. A., and Henkes, R. A. W. M., 1997, **Application of Turbulence Models to Bypass Transition**, *Journal of Fluid Engineering*, Vol. 119, pp. 859-866.
116. White, F.M., 1991, *Viscous Fluid Flow*, 2nd ed., Mc-Graw Hill, New York.
117. Wilcox, D. C., 1993, **Reassessment of the Scale-Determining Equation for Advanced Turbulence Models**, *AIAA Journal*, Vol. 30, pp. 324-331.
118. Wilcox, D. C., 1993, *Turbulence Modeling in CFD*, DCW Industries, Inc., La Canada, California.
119. Wilson, D. E., and Hanford, A. J., 1998, **An Unsteady Velocity Formulation for the Edge of the Near-Wall Region**, *Journal of Turbomachinery* Vol. 120, pp. 351-361.
120. Wood, P.E., and Chen, C.P., 1986, **A Calculation Scheme for Computing Turbulent Shear Flows in the Developing Region Using Closure Models**, *Numerical Heat Transfer*, Vol 9, pp. 115-123.
121. Yap, C. R., 1987, **Turbulent Heat and Momentum Transfer in Recirculating and Impinging Flows**, Doctoral Thesis, University of Manchester, Manchester, England, U. K.
122. Yardi, N.R., and Sukathme, S.P., 1978, **Effect of Turbulence Intensity and Integral Length Scale of a Turbulent Freestream on Forced convection Heat Transfer from a Circular Cylinder in Crossflow**, *International Heat Transfer Conference, 6th, Proceedings General Papers, Nuclear Reactor Heat Transfer, Forced Convection, Paper FC(b)-29*, Hemisphere Publ., Washington, D.C., , Vol. 5, pp. 347-352.
123. Zang, L., and Han, J.C., 1995, **Combined Effect of Freestream Turbulence and Unsteady Wake on Heat Transfer Coefficients from a Gas Turbine Blade**, *ASME Journal of Heat Transfer*, Vol. 17, 296-302.

124. Zdravkovich, MM., 1997, *Flow around Circular Cylinders: a Comprehensive Guide Through Flow Phenomena, Experiments, Applications, Mathematical models, and Computer Simulations*, Oxford University Press, Toronto
125. Zheng, X., Liao, C., Liu, C., Sung, C. H., and Huang, T. T., 1997, Multigrid Computation of Incompressible Flows Using Two-Equation Turbulence Models: Part I – Applications, *Journal of Fluid Engineering*, Vol. 119, pp. 900-905.
126. Zheng, X., Liao, C., Liu, C., Sung, C. H., and Huang, T. T., 1997, Multigrid Computation of Incompressible Flows Using Two-Equation Turbulence Models: Part II – Numerical Methods, *Journal of Fluid Engineering*, Vol. 119, pp. 893-899.



